Global structure prediction of phase diagrams

Dissertation

zur Erlangung des Doktorgrades der Naturwissenschaften
(Dr. rer. nat.)

der

Naturwissenschaftlichen Fakultät II
Chemie, Physik und Mathematik

der Martin-Luther-Universität
Halle-Wittenberg

vorgelegt von

Herrn Steigemann, Conrad
geb. am 15.02.1986 in Schwedt / Oder

Betreuer: Prof. Dr. M. Marques

1. Gutachter: Prof. Dr. M. Marques
2. Gutachter: Prof. Dr. W. Hergert
3. Gutachter: Prof. Dr. X. Blase

Datum der Abgabe: 19.12.2019
Datum der öffentlichen Verteidigung: 01.07.2020
Vorsitzender der Promotionskommission: Prof. Dr. D. Reichert

For every moment of truth,
there is confusion in life.

Ronnie James Dio

Contents

List of abbreviations

BCE	before the Christian Era
CPU	central processing unit
DFT	density-functional theory
DFTB	density-functional tight-binding
GGA	generalized gradient approximation
GM	geometric mean
GPU	graphics processing unit
LDA	local density approximation
MD	molecular dynamics
MOSFET	metal-oxide-silicon field-effect transistors
MP	materials project
PES	potential energy surface
RMS	root mean square
SoC	system on a chip
VASP	vienna ab initio simulation package, program for DFT calculations

Chapter 1

Introduction

This dissertation discusses strategies to search efficiently for new materials, each with specific properties. Each search is motivated by a different background and requires an individual variation of the general prediction techniques introduced in section 2.5. Although at first the task to identify new materials and structures seems to be niche research and the simulations of this work are based on density-functional theory[1, 2], the roots of this task go much deeper than the 1960s.

The whole evolution of humankind ran parallel to the investigation and exploitation of new materials with their specific properties. Starting with the stone age $3.3 \cdot 10^6$ years ago, simple tools were created out of stone and wooden parts [3]. The invention of ovens and crafting tools to quarry ore enabled the extraction of metals from ore. First bronze, an alloy group of copper and e. g. tin became accessible ($T_{\mathrm{Cu}}^{\mathrm{melt}} = 1360$ K [4]). The so-called Bronze Age lasted in Europe from around 2300 BCE to 700 BCE [5, 6]. The techniques of smelting and manufacturing tools improved over time and iron became accessible. It has a higher melting temperature than copper ($T_{\mathrm{Fe}}^{\mathrm{melt}} = 1810$ K [4]) and labels the Iron Age. In Europe the Iron Age lasted from 700 BCE to 1 BCE [6].

Over these periods, as an example, knives and blades were first made of stone and advanced to copper- and iron-based ones. Nowadays, knives with blades of steel (an alloy of iron and carbon [7]), ceramics or even plastics are used depending on their specific purpose. Additionally, the handle and sleeve of a knife are usually dominated by another material to fit the usage and optimize characteristic properties. This example may seem historic and general, but there are further more recent examples. They demonstrate how the application of new materials can open up new possibilities even today and can lead further to a direct loop of improvement regarding tools, processing techniques and materials:

- Discussing new materials, a first thought is about the discovery and accessibility of radioactive elements. This history already lasts for more than 200 years and leads to topics still important today: The chemical element Uranium was discovered by Martin Heinrich Klaproth in 1789 [8, 9]. However, around 100 years passed until Marie Curie, Pierre Curie and Henri Becquerel discovered and characterized radioactive radiation for the first time while working on uranium ore. Additionally, they discovered further radioactive elements: Polonium and Radium [10]. This research can be seen as a starting point of further investigations leading the label 'atom' (greek *átomos*, undividable) to absurdity: The origin of the radiation, nuclear recoil, isomerism and fission were

discovered by Otto Fritsch, Otto Hahn, Lise Meitner and Fritz Straßmann in 1909, 1921 and 1938 [11–14].

In retrospective, these discoveries about the structure of atoms combined with the discovery of the neutron by James Chadwick in 1932 [15] and Einstein's famous equality of mass and energy from 1905 [16] drew a baseline regarding civil and military usage of nuclear power. Both are topics repeatedly dominating the news until today.

- A second example concerns carbon, an element of many faces and applications which is further dealt with in chapter 3. Graphite is used as the color of pencils, as electrode as well as it is an additive in lubricants [17]. Isolated layers of graphite (graphene) create a whole research field on its own [18, 19]. Another field are carbon nanotubes, whose structure is related to graphite as well [20]. In addition, carbon is the main component of coal and diamonds. The last are applicable in jewelry as well as in the tools segment to harden drills and cutting discs.

  Furthermore, threads of carbon can be woven into fabric, the basis of carbon-fiber composite materials. The manufacturing process allows almost arbitrary forms. Due to the good strength-to-weight ratio and insensitivity to corrosion, carbon-fiber composites are used in professional racing sports, aerospace industry and even the medical sector [21].

- The semiconductor industry offers a third example to highlight the cycle of developing a tool and to use it to improve its next generation. The processing power of one processor generation allows to simulate and develop the even more complex circuitry of an upcoming processor generation. The increased computation power of that upcoming generation can help again to develop an even more complex successor generation. As current processors contain up to tens of billions of transistors (NVIDIA Titan RTX GPU $18.6 \cdot 10^9$ transistors, AMD Ryzen 39xx CPU $9.89 \cdot 10^9$ transistors, Apple A13 SoC $8.5 \cdot 10^9$ transistors), increased computation power still makes a difference [22–25].

  Furthermore, the search and application of 'high-k' materials offers a fourth, recent example of the necessity to change the processed materials. In computers, the central components of processors are their metal-oxide-silicon field-effect transistors (MOS-FETs). For decades silicon oxide has been used to insulate gate electrodes (sketched in figure 1.1(a)). New process nodes were developed enabling to shrink transistors step-by-step. This also led to an increase in transistor density on the processor dye as well as the reduction of the switching time and the individual power consumption of a transistor. These developments are depicted in Moore's law [26–28]. However, the designs not only shrank the length of the channel but also used thinner and thinner oxide layers for insulation. Over many years its thickness scaled exponentially by a factor of $0.7 \approx \frac{1}{2}\sqrt{2}$ between process nodes. Unfortunately, oxides with a thickness of 2 nm and below started to exhibit increasing gate leakage due to electrons tunneling through the insulator between gate and channel (see figure 1.1(b)) [29–31]. The diagram not only shows that this issue was resolved by designing the 45 nm process node. It also reveals to which extend gate leakage has already limited the technical possibilities of several prior process nodes.

  To reduce the leakage by the tunnel effect, the general strategy was to increase the absolute thickness of the gate insulation. However, the electronic properties of the field-effect

(a) Sketch of the cross-section of a n-channel field-effect transistor with channel length L [35].

(b) Scaling of the effective oxide thickness and the gate leakage of several of Intel's process nodes. The data originates from [30, 36].
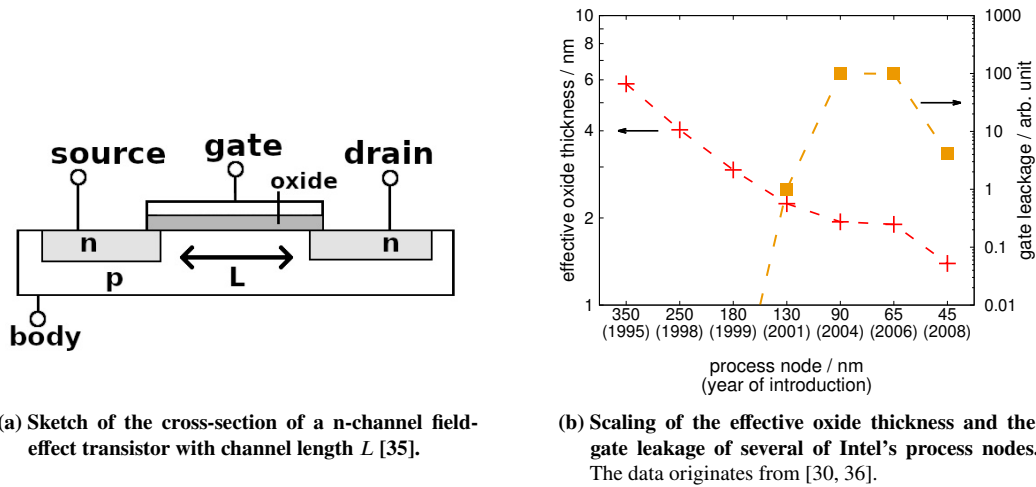
Figure 1.1: Benefits of Intel's high-k+metal gate transistor design. In panel (a), a planar metal-oxide-semiconductor field-effect transistor (MOSFET) is sketched. The three electrodes are labeled *source*, *gate* and *drain*. *Body* defines the reference potential of the silicon substrate. *n* and *p* mark its doped regions. The oxide insulates the gate electrode from the channel between source and drain. Shrinking the size of transistors up to the 130 nm process node, the thickness of the oxide is reduced exponentially (panel (b)). Due to increasing leakage only slightly thinner oxides could be used at the 90 nm and 65 nm process node. The high-k+metal gate transistor design of the 45 nm node enabled Intel to further reduce the effective oxide thickness, while as well reducing the gate leakage in comparison to the former 65 nm node. Initially, the name of the process nodes referred to the corresponding gate pitch. Due to marketing, the labeling has become more abstract to represent the evolution of processes. Furthermore, nodes of different companies are labeled the same although they provide different results [37, 38].

transistors should not be sacrificed. The source-drain current depends on the gate capacity C [31–33]. It depends on the gate area A and the insulator thickness d:

$$C = \varepsilon_0 \varepsilon_r \frac{A}{d} \tag{1.1}$$

As equation (1.1) contains the ratio ε_r/d, a large relative dielectric permittivity ε_r allows for larger thickness d while maintaining the same capacity C. To resolve the scaling problem, a search started looking for 'high-k' materials applicable in lithographic processes on silicon [30, 31, 33, 34]. In this context k stands for κ or ε_r and 'high-k' refers to larger values than silicon oxide ($\varepsilon_r(\text{Si, O}) = 3.9$ [31]). In 2007 Intel changed the design of its transistors from poly-silicon gates insulated by silicon oxide to metal gates insulated by hafnium oxide ($20 < \varepsilon_r(\text{Hf, O}) < 25$). The gate leakage could be reduced by a factor of 1000 (PMOS) or >25 (NMOS) compared to the former process generation [30–32]. High-k+metal-gate transistor designs have further been pursued at the follow-up 32 nm process node [34].

The examples above show that the search for new materials is still relevant today. However, the search strategy changed. Nowadays computational high-throughput studies are possible substituting initial trial and error searches via experiments. These theoretical studies allow for scanning a large variety of compositions to look for new structures with certain material

properties. The identification of reaction paths to enable synthesizing these structures in experiments is not part of these studies. However, the formation energy provides information to approximated how accessible predicted structures are [39].

In this dissertation global structure prediction calculations are performed and prediction techniques are discussed. Therefore, the basic terminology to describe these simulations is introduced in chapter 2.

In chapter 3 the stability of bulk carbon clathrates and therefore the possibility of carbon forming such structures is studied. A global structure prediction approach based on the minima hopping method is presented in section 3.1. Further attempts based on the geometrical comparison of isolated clathrate cages with the structure of diamond are discussed in section 3.2. This geometric approach is general and not limited to a certain group-IV element. The resulting stability ordering of structures is checked and confirmed by calculations based on density-functional theory (section 3.2.3). As clathrate structures are known for other group-IV elements besides carbon, in section 3.2.4 the geometric approach is reevaluated regarding the silicon and germanium analog of these carbon structures. An isolated cage shows a finite extent in any direction. Therefore, they can be seen as a quasi-zero-dimensional case. Linking favored cages periodically and expanding the results from isolated clusters to rods, planes and 3D crystals is discussed in section 3.3. A different perspective on the problem by slightly changing the formulation of the problem from pure-carbon clathrates to carbon-based clathrates is motivated by Tao Zeng *et al.* [40] and is discussed in section 3.4. The results of Zeng *et al.* are discussed and put into context with further investigations of the stability.

In chapter 4 basic investigations of the stability of some binary compounds are performed. They are investigated within the context of creating a training set to parameterize the pairwise interactions of the elements aluminum, lanthanum, strontium, titanium and oxygen to accelerate future global structure prediction calculations of these elements.

In chapter 5 approaches for constraining global structure prediction calculations are proposed. This is useful, e.g., to predict low-dimensional crystals or in general to predict crystal structures with certain geometric properties.

An outlook towards further investigations is presented in chapter 6.

Chapter 2

Theoretical background

The tradition of the search for new solid, crystalline materials has already been outlined by the introduction. This dissertation focuses on their theoretical prediction based on Density-functional theory calculations (DFT) and geometric comparisons of structures. Density-functional theory as well as the Born-Oppenheimer-approximation are introduced in section 2.1 and enable the calculation of the energy of configurations of electrons or rather of atoms. Density-functional tight-binding (DFTB) is an approximational approach to DFT and is outlined in section 2.2. The movements of atoms can be simulated by molecular-dynamics simulations, which are performed according to the forces acting on the nuclei (see section 2.3). The stability of structures is discussed in section 2.4: The combination of all possible positions of the present atoms and the shape of the unit-cell spans a potential energy surface.
The complete curvature of the potential energy surface describes all forces acting in all possible structures. Local minima are the desired spots on this abstract surface that need to be identified, as there the forces acting on all atoms are zero and locally the potential energy surface is only convex shaped. Furthermore, in section 2.4 it is also discussed which energies of a structure can be calculated, how they are connected and which energy needs to be investigated. Phase diagrams are introduced to compare the stability of structures with different composition of chemical elements.
Scanning a multi-dimensional area effectively for minima can be done with the minima hopping method. It is introduced and compared to further minimization algorithms in section 2.5.

2.1 Density-Functional Theory

In quantum mechanics, a system is described by its wave function $\Psi\big(\{\mathbf{R}_i\},\{\mathbf{r}_j\},t\big)$. $\{\mathbf{R}_i\}$ is the set of nuclear positions and $\{\mathbf{r}_j\}$ represents the set of positions of the electrons. The wave can be described as the superposition of individual modes Ψ_f, defined by the Schrödinger equation [41, 42]. When $\hat{H}$ shows no explicit time-dependence, the time-independent equation can be written as:

$$\hat{H}\left(\{\mathbf{R}_i\},\{\mathbf{r}_j\}\right)\,\Psi_f\big(\{\mathbf{R}_i\},\{\mathbf{r}_j\}\big) \;=\; E_f\,\Psi_f\big(\{\mathbf{R}_i\},\{\mathbf{r}_j\}\big) \tag{2.1}$$

Ψ_f and E_f are the wave function and the energy of eigenstate f. Looking closer at the Hamilton operator $\hat{H}$, it can be decomposed into kinetic energies $\hat{T}$ and the potential energies $\hat{V}$ of the interaction of electrons (el) and nuclei (nu):

$$\hat{H} = \underbrace{\hat{T}_{\text{nu}} + \hat{V}_{\text{nu,nu}}}_{\hat{H}_{\text{nu}}\left(\{\mathbf{R}_i\}\right)} + \underbrace{\hat{T}_{\text{el}} + \hat{V}_{\text{el,el}} + \hat{V}_{\text{ext}}}_{\hat{H}_{\text{el}}^{\{\mathbf{R}_i\}}\left(\{\mathbf{r}_j\}\right)} \tag{2.2}$$

As the inertial masses of electrons m_{el} and nuclei or protons m_{p} differ in orders of magnitude ($m_{\text{p}}/m_{\text{el}} \approx 1.8 \cdot 10^3$, [43]), within the **Born-Oppenheimer approximation** [44, 45] the electrons adjust instantaneously with respect to the position of the nuclei. The position of the atomic nuclei can be treated as static while the spatial distribution of the electron density adapts to the Coulomb potential of the nuclei, minimizing their energy. This context motivates to write the nuclei-electron interaction potential $\hat{V}_{\text{nu,el}}$ as a potential $\hat{V}_{\text{ext}}$ external to the electrons and to write Ψ_f furthermore as a product to separate its dependencies

$$\Psi_f\left(\{\mathbf{R}_i\}, \{\mathbf{r}_j\}\right) = \Xi\left(\{\mathbf{R}_i\}\right) \cdot \Psi_N^{\{\mathbf{R}_i\}}\left(\{\mathbf{r}_j\}\right) \tag{2.3}$$

with the nuclei wave function $\Xi\left(\{\mathbf{R}_i\}\right)$ and the N-electron wave function $\Psi_N^{\{\mathbf{R}_i\}}\left(\{\mathbf{r}_j\}\right)$. Often the nuclei are treated as classical particles and only the electron wave function needs to be obtained with respect to the position of the nuclei. However, one has to be aware that the electron density $n(\mathbf{r})$, but not the electron wave function, is an observable quantity. Both variables are linked according to:

$$n\left(\mathbf{r}_1\right) = N \int \mathrm{d}^3\mathbf{r}_2 \cdots \int \mathrm{d}^3\mathbf{r}_N \left|\Psi_N^{\{\mathbf{R}_i\}}\left(\{\mathbf{r}_j\}\right)\right|^2 \tag{2.4}$$

Density-functional theory allows to describe quantum mechanical calculations based on the electron density n and not based on the wave function Ψ_N like the Schrödinger equation. Reducing the number of degrees of freedom regarding electronic positions from $3N$ to 3 is the big advantage regarding the transition from the wave function to the particle density. Density-functional theory is based on the Hohenberg-Kohn-theorem which states that the ground-state electron density $n_{\text{GS}}(\mathbf{r})$ of a system is uniquely defined and a one-to-one relation exists between $n_{\text{GS}}(\mathbf{r})$ and the external potential v_{ext} [1].

Kohn and Sham proposed the calculation of an auxiliary system of non-interacting electrons yielding the same ground-state density as the interacting system [2, 46]. A self-consistent strategy to calculate the desired electron density $n(\mathbf{r})$ has been proposed by them, too [2, 47]. In Hartree atomic units ($\hbar = e^2 = m_{\text{e}} = 1$), the strategy is the following:

Initially the electron density is guessed and leads to the effective potential $v_{\text{eff}}[n](\mathbf{r})$ which can be written as a sum:

$$v_{\text{eff}}[n](\mathbf{r}) = v_{\text{ext}}(\mathbf{r}) + \underbrace{\int d^3\mathbf{r}' \, \frac{n(\mathbf{r}')}{|\mathbf{r} - \mathbf{r}'|}}_{\text{Hartree - term}} + \underbrace{\frac{\delta \, E_{\text{xc}}[n]}{\delta \, n}}_{v_{\text{xc}}[n](\mathbf{r})} \tag{2.5}$$

v_{ext} is the external potential, for example the Coulomb interaction of the electrons with present nuclei. The Hartree potential describes the interaction of the electrons. $v_{\text{xc}}[n]$ is the exchange-correlation potential and E_{xc} is the exchange-correlation energy. Now the Kohn-Sham equation is defined and needs to be solved for Kohn-Sham orbitals Φ_j and energies ε_j:

$$\varepsilon_j \, \Phi_j(\mathbf{r}) = \left(-\frac{1}{2}\nabla^2 + v_{\text{eff}}[n](\mathbf{r}) \right) \Phi_j(\mathbf{r})$$

$$n(\mathbf{r}) = \sum_j^{\text{occ}} \left| \Phi_j(\mathbf{r}) \right|^2 \tag{2.6}$$

Equation (2.6) approximates the kinetic energy as the kinetic energy of a non-interacting system of electrons and shifts the description of all interactions of electrons into the effective one-particle potential v_{eff}. After solving the current iteration of the Kohn-Sham orbitals and energies, the electron density $n(\mathbf{r})$ can be calculated by summing over the occupied orbitals.

The cycle of the equations of (2.6) needs to be calculated until the density $n(\mathbf{r})$ is converged. Now the total energy E_{tot} of the structure can be expressed as:

$$E_{\text{tot}} = E_{\text{nuc,nuc}} + \sum_j \varepsilon_j - \frac{1}{2} \iint d^3\mathbf{r} \, d^3\mathbf{r}' \, \frac{n(\mathbf{r}) \, n(\mathbf{r}')}{|\mathbf{r} - \mathbf{r}'|} + E_{\text{xc}}[n] - \int d^3\mathbf{r} \, n(\mathbf{r}) \, v_{\text{xc}}[n](\mathbf{r}) \tag{2.7}$$

The central place of approximations is the exchange-correlation functionals $E_{\text{xc}}[n]$ or $v_{\text{xc}}[n]$. Such functionals can be grouped into several classes. Two examples are the local density approximation (LDA) and the generalized gradient approximation (GGA). Within the first case, the energy density $\varepsilon_{\text{xc}}[n]$ depends locally on the density at positions $\mathbf{r}$, whereas in the second case the absolute value of the gradient $|\nabla n|$ is included as well, providing information on the change of n at positions $\mathbf{r}$.

$$E_{\text{xc}}^{\text{LDA}}[n] = \int d^3\mathbf{r} \, n(\mathbf{r}) \, \varepsilon_{\text{xc}}^{\text{LDA}}\left(n(\mathbf{r})\right) \tag{2.8}$$

$$E_{\text{xc}}^{\text{GGA}}[n] = \int d^3\mathbf{r} \, n(\mathbf{r}) \, \varepsilon_{\text{xc}}^{\text{GGA}}\left(n(\mathbf{r}), |\nabla n(\mathbf{r})|\right) \tag{2.9}$$

A first approximation regarding the energy density $\varepsilon_{xc}^{LDA}(n(\mathbf{r}))$ has already been proposed by Kohn and Sham using the energy density of a homogeneous electron gas [2, 46]. Libraries like LIBXC [47, 48] provide a large variety of approximations to the exchange-correlation functional and enable the user to easily apply a different functional. In solid-state physics, the PBE-functional developed by John Perdew, Kieron Burke and Matthias Ernzerhof [49, 50] has become the standard functional and is used in this dissertation if not stated differently. It is a GGA-type functional. The DFT code used in this thesis is VASP [51–54]. Alternative common simulation tools are for example ABINIT [55–57] and Quantum ESPRESSO [58, 59].

2.2 Density-Functional Tight-Binding

Density-functional tight-binding is an approximation to the Kohn-Sham DFT scheme and uses the linear combination of a minimal basis set of atomic-like orbitals η_μ to describe the Kohn-Sham orbitals Φ_j [60, 61]:

$$|\Phi_j\rangle = \sum_\mu c_\mu^j |\eta_\mu\rangle \tag{2.10}$$

For the ground-state electron density $n(\mathbf{r})$, the decomposition of equation (2.10) can be applied to the Kohn-Sham equation (2.6). Multiplying the expression further from the left side with $\langle\eta_\nu|$ leads to equation (2.11), defining the Kohn-Sham energies ε_j.

$$\sum_\mu c_\mu^j \underbrace{\langle\eta_\nu| \hat{H}[n] |\eta_\mu\rangle}_{H_{\nu,\mu}} = \varepsilon_j \sum_\mu c_\mu^j \underbrace{\langle\eta_\nu|\eta_\mu\rangle}_{S_{\nu,\mu}} \tag{2.11}$$

The Hamiltonian of the ground-state density $\hat{H}[n](\mathbf{r})$ can be described by the two-center approximation as the operator built from the superposition of the atomic-like densities of the atoms α and β. The orbital ν is centered on atom α and the orbital μ is centered on atom β. $\delta_{\mu,\nu}$ is the Kronecker symbol:

$$H_{\nu,\mu} = \begin{cases} \langle\eta_{\alpha,\nu}| \hat{T} + V[n_\alpha + n_\beta] |\eta_{\beta,\mu}\rangle & \text{if} \quad \alpha \neq \beta \\ \delta_{\mu,\nu} \cdot \varepsilon_\mu^{\text{neutral free atom}} & \text{if} \quad \alpha = \beta \end{cases} \tag{2.12}$$

The energy of a structure can be calculated using:

$$E^{\text{DFTB}} = \sum_j \varepsilon_j + \frac{1}{2}\sum_{\alpha,\beta} V_{\alpha,\beta}^{\text{rep}}\left(|\mathbf{r}_\alpha - \mathbf{r}_\beta|\right) \tag{2.13}$$

Before treating a specific problem of interest for a certain combination of chemical elements, the Hamilton matrix elements $H_{\nu,\mu}$ and the overlap matrix elements $S_{\nu,\mu}$ need to be calculated in advance to determine the Kohn-Sham energies ε_j via equation (2.11). The pairwise repulsive

potential between atomic cores $V_{\alpha,\beta}^{\text{rep}}$ needs to be parametrized in advance too. This can be achieved by fitting equation (2.13) to a set of structures already calculated by DFT [62, 63].

To sum up, atomic-like orbitals forming a minimal basis set were combined with a two-center approximation. It allows for the pre-calculation of all important integrals during the initial parametrization. The main computational effort is shifted away from the specific problem of one structure towards describing the pairwise interaction of chemical elements. These descriptions can be reutilized at investigating further configurations. Furthermore, there is no need to perform self-consistent Kohn-Sham cycles regarding a certain problem of interest. This strategy helps to save time after the initial parametrization to receive an approximate result. The speedup with respect to DFT is up to three orders of magnitude [64]. The approximation works well if the electron density $n(\mathbf{r})$ can be approximated well by the superposition of the atomic-like densities $\sum_\alpha n_\alpha(\mathbf{r})$. In cases with occurring charge transfer, an extension of basic DFTB, like self-consistent charge density-functional tight-binding (SCC-DFTB), needs to be used [65]. It includes further corrections depending on charge fluctuations and contains self-consistent charge calculations [60].

2.3 Molecular dynamics simulation

Using the methods above, the total / internal energy of a structure of interest can be calculated. Although they can also provide the forces acting on the atoms, an algorithm is still needed to solve the equation of motion. Several algorithms to solve the system of equations for any atom j of a given structure have been discussed by Michael P. Allen in [66]:

$$m \frac{d^2}{dt^2}\mathbf{r}_j(t) = \mathbf{F}_j(t) \tag{2.14}$$

One of the most important algorithms is the Verlet-algorithm, introduced by Loup Verlet in 1967 [67, 68]. It leads to a time-reversible and energy conserving solution of equation (2.14). The movement of the atoms is described without the need to calculate the velocity $v_j(t)$ of any atom saving computation time. To calculate the upcoming set of positions $\mathbf{r}_j(t+\delta t)$ only the current set of positions $\mathbf{r}_j(t)$ and the corresponding set of accelerations $\mathbf{a}_j(t)$ needs to be known:

$$\mathbf{r}_j(t+\delta t) = 2\,\mathbf{r}_j(t) - \mathbf{r}_j(t-\delta t) + (\delta t)^2\,\mathbf{a}_j(t) \tag{2.15}$$

During molecular dynamics simulations the atoms are moved in discrete, small time steps δt before the forces need to be recalculated due to the change of geometry. There are different possibilities like Lennard-Jones potentials, DFT or DFTB to calculate the energy E of the system. In conservative force fields, variations of the position $\mathbf{r}_j$ allow calculating the accelerations $\mathbf{a}_j(t)$:

$$\mathbf{a}_j(t) = \frac{d^2}{dt^2}\mathbf{r}_j(t) = -\frac{1}{m_j}\frac{\partial\,E(t)}{\partial\,\mathbf{r}_j} \tag{2.16}$$

orignal Verlet
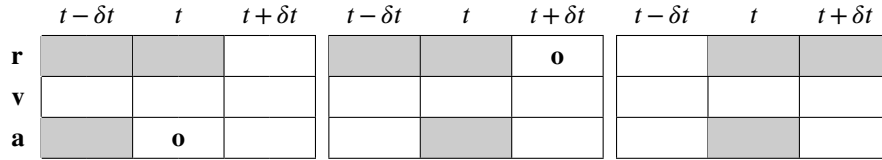
leap-frog
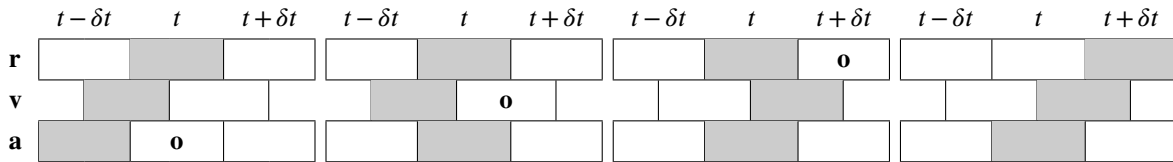
velocity form
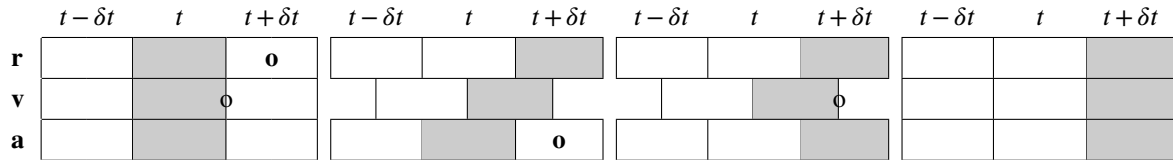
Figure 2.1: Variations of the Verlet algorithm. Each block represents the knowledge during a simulation step. It is horizontally divided into different time steps and each row represents positions **r**, velocities **v** or accelerations **a**. The *o* highlights variables which are calculated next with the help of the colored cells. Some algorithms use half-time steps or do not need to calculate any velocity [66, 69]. In comparison it is also visible, that one iterative step of the original Verlet algorithm is divided in three sub-steps, while leap-frog and the velocity form show four sub-steps for one iteration step. The sketches are reworked from [69].

In the original Verlet algorithm, the equations (2.15) and (2.16) create a cycle to stepwise calculate the positions and accelerations of the particles [66–68]. When needed, the velocities can be obtained separately to estimate the kinetic energy:

$$\mathbf{v}(t) = \frac{1}{2} \frac{\mathbf{r}(t+\delta t) - \mathbf{r}(t-\delta t)}{\delta t} \tag{2.17}$$

Besides these equations, the strategy of the Verlet-algorithm and of two of its variants to solve the equation of motion (2.14) are visualized in figure 2.1.

2.4 Stability

When investigating a system, the energy of a certain configuration can be calculated with methods like DFT or DFTB. To go further and be able to predict which of two configurations is more stable than the other, one needs to introduce phase diagrams.

2.4.1 Potential energy surface

The potential energy surface connects the potential energy of a configuration with its internal coordinates. In the simplest, non-trivial case only two atoms are present and the simulated cell is sufficiently large to neglect interactions of atoms with their duplicates from neighboring cells due to periodic boundary conditions. In contrast to the six coordinates needed to describe two positions in 3D space, there is only one internal coordinate - the distance between the two atoms. In 1927 Walter Heitler and Fritz London calculated the energy for a hydrogen molecule depending on the distance of its atoms [45, 70]. This potential energy surface of two hydrogen atoms is shown in figure 2.2(a). For large distances between the atoms, the energy converges to a constant value set to zero. At small distances, the atoms repel each other. This behavior is represented by an increase in energy for small distances. Between these two extreme cases, figure 2.2(a) shows a local minimum, representing the expected bond length and dissociation energy. As there are only two hydrogen atoms in this example, the potential energy surface spans only one dimension and contains only one minimum. A molecule of 2, 3, 4, 5, 6, ... atoms has 1, 3, 6, 9, 12, ... degrees of freedom. When bulk structures are investigated instead of isolated molecules, the positions of atoms are described by a unit cell and periodic boundary conditions. This way an infinitely large crystal with no surface can be simulated using only a finite number of atoms. To describe this periodicity in three-dimensional space, six further parameters are needed (three parameters for the lengths a, b, c of the unit vectors of the unit cell and three for the planar angles α, β, γ between them). Therefore, simulating structures of more atoms, the potential energy surface needs to be investigated in a higher dimensional space. This not only limits the possibilities of visualization, but with a growing number of atoms, the surface shows exponentially more local minima [71]. Both complicates the sampling of the potential energy surface and the identification of its global minimum configuration. From a brief view one might identify several separated funnels. At a closer look the surface reveals more of its details and the funnels not only contain one local minimum each. To transit from one local minimum to another, a certain activation energy is needed to overcome the barrier. The configurations of local minima are also called dynamically stable.

2.4.2 Bell-Evans-Polanyi principle

The Bell-Evans-Polanyi principle [72–74] connects the height of a potential barrier on the potential energy surface with the expected gain in energy when transitioning from one local minimum to a neighboring minimum. In figure 2.2(b) it is sketched, how low energy barriers
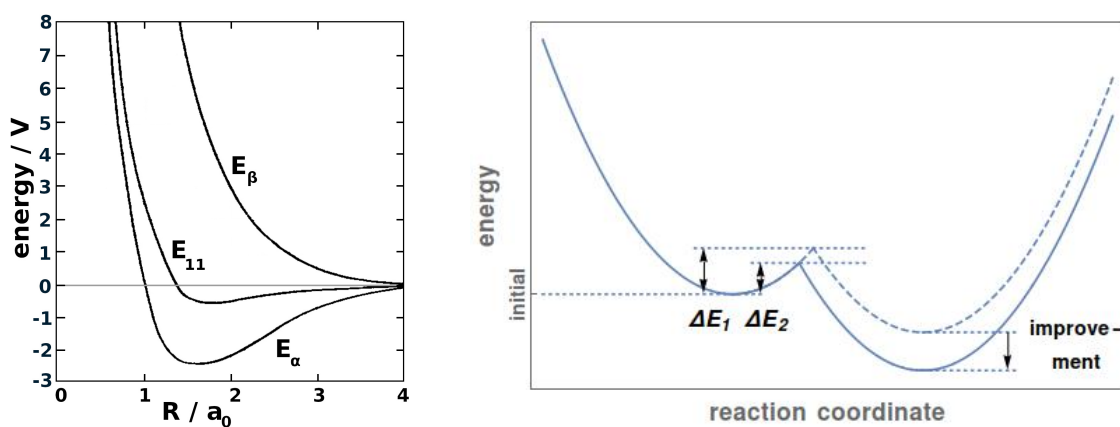
(a) Heitler-London's potential energy surface $E(R)$ represents a system of two hydrogen atoms of the distance R. E_α describes the covalent attraction and E_β the elastic reflection. At E_{11} only the Coulomb interaction is shown and the indistinguishability of the electrons is neglected. It reveals a less stable minimum than E_α. The graph has been reworked from [70].

(b) Sketch of the Bell-Evans-Polanyi principle. Parabolas are used to sketch the potential energy surface regarding two possible reactions. Each leads to a local minimum structure on the right. The energetic barriers preventing these reactions are ΔE_1 and ΔE_2. Regarding the comparison $\Delta E_1 > \Delta E_2$, the second reaction path (non-dashed) leads to an energetically lower minimum than the first, dashed path. The sketch is based on [72].

Figure 2.2: Local sketches of the potential energy surface.

are supposed to lead to lower energies. When looking for low-energy structures, high energy barriers should not be favored as they tend to lead to minima, which are not as low.

2.4.3 Enthalpy and phase diagrams

The Helmholtz free energy $F(N_{atoms}, T, V)$, or more specific total energy E^{tot}, of a structure can be calculated directly with methods like density-functional theory (section 2.1) or density-functional tight-binding (section 2.2). Here, N_{atoms} is the number of atoms in the unit cell, V its volume and T the temperature of the system. However, the obtained free energy F of different configurations cannot be compared directly, if they represent different pressures p. A change in pressure represents a different condition to minimize the energy of the structure by forming a certain geometry. Therefore, in most cases it makes no sense only to minimize F when looking for stable configurations. Furthermore, there is also no need to limit the volume V of the unit cell to a certain value. Therefore the free enthalpy, Gibbs energy G needs to be investigated, as it directly depends on the pressure p.

$$G(N_{atoms}, T, p) = F(N_{atoms}, T, V) + pV \tag{2.18}$$

A counterexample is the investigation of 2D-structures under strain. Here, the investigation of strain slightly shifts the context. For example Borlido *et al.* in fact conserves the volume V in constrained global structure prediction calculations [19].

Furthermore, it should be mentioned, according to the transformation of equation (2.19), the four thermodynamic potentials internal energy U, enthalpy H, free energy F and free enthalpy G of any system show identical values as long as temperatures of 0 K and pressures of 0 GPa are investigated. In this dissertation this condition is always met for the temperature. Sometimes a pressure is applied to the system. Correspondingly the enthalpies H and G are identical and the free energy F is equal to the internal energy U.

$$\begin{aligned}
U(N_{atoms}, S, V) & \\
H(N_{atoms}, S, p) &= U + pV \\
F(N_{atoms}, T, V) &= U - TS \\
G(N_{atoms}, T, p) &= U + pV - TS
\end{aligned} \tag{2.19}$$

S is the entropy of the structure. To be able to compare the stability of structures, it is necessary to normalize the extensive enthalpy G of the unit cell to the number of atoms in the unit cell N_{atoms} to receive the intensive enthalpy $g = G/N_{atoms}$. Furthermore, to tell which composition of two elements is more stable, it is necessary to compare structures of different compositions. Each composition is characterized by the number of N_i atoms of element El_i. These parameters allow to calculate the formation energy E_{form} (see equation (2.20)). There, $g_{min}(El_i, p)$ is the intensive enthalpy of the ground-state structure of each elementary substance at the currently investigated pressure p. It serves as a reference and can be calculated using the global structure
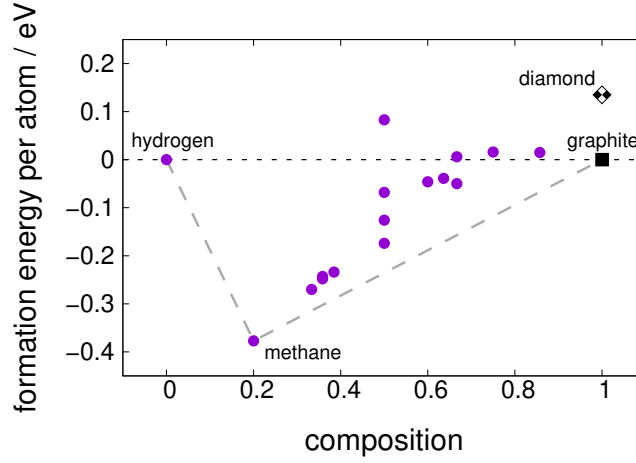
Figure 2.3: Phase diagram of carbon and hydrogen at zero pressure. The convex hull is highlighted by the gray dashed line connecting the data points of hydrogen, methane and graphite. The individual energies are taken from the Materials Project database [75].

prediction techniques described in section 2.5. As in most cases $g_{\text{min}}(El_i, p = 0)$ is needed, these values are also listed in databases like the materials project website [75].

$$E_{\text{form}}\left(\text{structure}, p\right) = g\left(\text{structure}, p\right) - \sum_i \frac{N_i}{N_{\text{atoms}}} \, g_{\text{min}}\left(El_i, p\right) \qquad (2.20)$$

The formation energy E_{form} describes the amount of net energy needed to form a certain geometry from the ground-state structures of its constituent elements. Accordingly, the most stable structural phase of each element has a formation energy of precisely zero. Plotting the formation energy with respect to the composition of the unit cell creates a phase diagram. Figure 2.3 shows the diagram of hydrogen-carbon compositions. The abscissa measures the number of carbon atoms per total number of atoms in the unit cell. It does not tell how many atoms are inside the cell, but the diagram allows to compare structures of different cell size. The figure mentions five structures with a positive formation energy. They are thermodynamic unstable and can decompose into structures of the individual elements or other mixed structures with a lower formation energy. Hydrogen and graphite are the reference structures with zero formation energy and most other data points mark a negative formation energy. However, a negative formation energy solely expresses that the structure is not going to decompose into individual structures of all constituent elements. It does not imply thermodynamic stability. Only the structures positioned on the convex hull sketched by the gray dashed line in figure 2.3 are thermodynamically stable. The hull is spanned between the most stable structures of the pure elements and their mixtures. As the name suggests, its curvature is strictly convex and by definition the energetic distance E_{hull} of a structure to the convex hull cannot be negative. If a new structure is identified and seems to lie below the hull, the hull needs to be readjusted to include the new structure setting E_{hull} here back to zero. Nevertheless, depending on the

investigated elements, not always does a stable mixture exist (see chapter 4). In those cases the convex hull is a straight horizontal line (binary phase diagram), a plane (ternary phase diagram) or in general a hyper-plane connecting the phases of the constituent pure elements in a multi-dimensional phase diagram.

According to equation (2.18), the enthalpy G depends on F and the product pV. It hints, the ordering of structures by enthalpy can change under pressure. If the volume of the unit cell is small, the term $+pV$ in equation (2.18) adds a smaller contribution than in cases of larger cells when the pressure is increased. One example is the phase transition of carbon between graphite and diamond. Diamond has a smaller unit cell than graphite and is stabilized under pressure as it has a smaller contribution pV compared to structures with a larger unit cell ($V_{\mathrm{graphite}}(p=0) = 10.1$ $\mathring{\mathrm{A}}^3/\mathrm{atom}$, $V_{\mathrm{diamond}}(p=0) = 5.71$ $\mathring{\mathrm{A}}^3/\mathrm{atom}$) [75]). At temperatures of 0 K, carbon has a structural phase transition from graphite to diamond at a pressure of 6 GPa. There, the two phases have a similar formation energy (see figure 3.22 on page 52). At higher temperatures, higher pressures are needed so graphite and diamond can coexist [76, 77].

2.5 Global structural prediction

Optimizing the crystal structure of a bulk material is not trivial. As already pointed out in section 2.4.1 the potential energy surface has an extremely complicated shape. Besides its many-dimensionality, the pressure p and the number of atoms N_{atoms} inside of the unit cell are two additional parameters which need to be taken into account. The goal is not solely to identify one or some local minima of the enthalpy. The one crystal structure needs to be found, which represents the lowest enthalpy of all corresponding possibilities.

Although permutations of the parameters of the unit cell, the indistinguishability of atoms of the same element and structural symmetries symmetrizes the potential energy surface, this does not considerably simplify the problem. Directly keeping track of such symmetries makes handling the problem even more complicated.

The Bell-Evans-Polanyi-principle (see section 2.4.2) hints at another detail the search algorithm needs to pay attention to. On one side, passing low energy barriers needs to be preferred when leaving one local minimum on the potential energy surface, as they promise to lead to an energetically lower minimum. On the other side, large energy barriers need to be overcome to be able to investigate different areas, funnels of the potential energy surface.

Furthermore, investigating the same region again and again renders the algorithm inefficient, so an algorithm should keep track of which structures have already been investigated. These are all criteria an appropriate search algorithm needs to fulfill to perform global structure prediction calculations.

In the following subsections, several optimization techniques are discussed. They are sectioned in local and global algorithms. Within the boundaries of an applied DFT-functional or DFTB-parametrization, the result of each algorithm can always be treated as an upper limit for the minimum enthalpy.

2.5.1 Local optimization algorithms

When optimizing a structure locally, one initial configuration always leads to solely one minimum on the potential energy surface. A lower boundary on the formation energy exists, as structures cannot become arbitrarily stable. Local search algorithms cannot escape a basin and stop when they identified one. That is why these methods alone are hardly applicable for global optimizations.

Method of steepest descent

The method of steepest descent can be used to optimize a structure locally with respect to the potential energy surface. In general the method minimizes a function f (here the enthalpy H) by shifting the argument $\mathbf{x}_k$ iteratively against the direction of the gradient $\nabla f(\mathbf{x}_k)$ [78]:

$$\mathbf{x}_{k+1} = \mathbf{x}_k - \varepsilon \nabla f(\mathbf{x}_k) \tag{2.21}$$

In general, the method can be roughly described as going down a slope to find the lowest point of the valley. The parameter $\varepsilon > 0$ allows an adjustment of the step size. If the potential can be locally approximated by a parabola, it is also possible to use individual step sizes ε_k to reach the local minimum in each direction within one step. As the method relies on the gradient, it leads the set of optimization parameters $\mathbf{x}_k$ down the slope of the potential energy surface to a configuration close to the initial parameter set $\mathbf{x}_0$ with vanishing forces $\mathbf{0} = \nabla f(\mathbf{x})|_{\mathbf{x}=\mathbf{x}_k}$. This criterion characterizes a local minimum as well as a saddle point of f. Both cases can be distinguished by the Hessian matrix $\nabla(\nabla f(\mathbf{x}_k))$. A saddle point is marked by an indefinite Hessian at $\mathbf{x}_k$ and a local minimum is indicated by a positive definite Hessian at position $\mathbf{x}_k$ [79].
Besides its simplicity, the algorithm contains an obvious inefficiency: The steps are not chosen necessarily in directions linearly independent of each other. Therefore each optimization step can partially 'deoptimizes' previously optimized coordinates leading to a zig zag movement on the potential energy surface (see red path in figure 2.4).

Conjugate gradient method

The conjugated gradient method improves upon the method of steepest descent. Again, the method is based on the gradient of the function $f(\mathbf{x})$ to iteratively minimize the value $f(\mathbf{x}_i)$. However, a second number series $\mathbf{h}_i$ needs to be introduced [80, 81]:

$$\begin{aligned} \mathbf{x}_{i+1} &= \mathbf{x}_i + \lambda_i \mathbf{h}_i \\ \mathbf{h}_{i+1} &= \frac{\left(\nabla f(\mathbf{x}_{i+1})\right)^2}{\left(\nabla f(\mathbf{x}_i)\right)^2} \mathbf{h}_i - \nabla f(\mathbf{x}_{i+1}) \end{aligned} \tag{2.22}$$
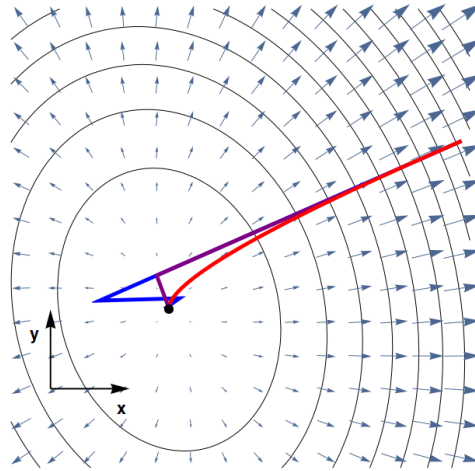
Figure 2.4: Comparison of the local optimization steps minimizing a quadratic function $f(\mathbf{x})$. Each black ellipse represents a region of constant values $f(\mathbf{x})$ and the blue arrows visualize the vector field $\nabla f(\mathbf{x})$. The minimization algorithms are the method of steepest descent with a large step size (blue), the method of steepest descent with a small step size (red) and the conjugated gradient method (purple). All algorithms start from the same position on the right and identify the one local minimum, which is highlighted black.

The starting positions are $\mathbf{x}_0$ and the initial correction $\mathbf{h}_0 = -\nabla f(\mathbf{x}_0)$. In the parameter space $\mathbf{x}_{i+1}$ is shifted linearly away from $\mathbf{x}_i$ by the step size of λ_i, calculated separately to minimize f along this line. Each correction $\mathbf{h}_i$ also takes previous corrections in account. The steps of the conjugate gradient method and the method of steepest descent are compared in figure 2.4.
As the algorithm minimizes the gradient, it can lead to saddle points like the method of steepest decent. Historically the algorithm was proposed by Magnus R. Hestenes and Eduard Stiefel in 1952 [80] to solve linear systems of equations.

2.5.2 Global optimization algorithms

Investigating the potential energy surface on a global scale can also be done by a variety of strategies. Each offers a different level of complexity and issues. However, all reasonable methods need to combine the global search with the local optimization of test positions to ensure their result represents a local minimum of the potential energy surface. So the previously introduced local strategies are still needed and do not solely serve as an entry point to optimization methods.

Random search

The method of random search is perhaps the simplest global minimization algorithm. First the positions of the atoms are taken randomly as well as the parameters of the unit cell of the crystal. This step is coupled with a local optimization strategy. Afterwards, a new configuration can be

created completely randomly or evolving from the previous configuration on a random path on the potential energy surface (random line search) [82, 83]. Only the pressure and configuration of atoms stays constant within a run.

Due to the independence of the positions, the algorithm is easy to parallelize on computers. However, as each position is only optimized within its basin and the surrounding basins are only investigated by chance, it is unpredictable how long the search is going to last and how close the current lowest value is to the true global minimum. Even if the global minimum has been identified in finite time, due to this lack of context of the test positions it can be hard to identify this configuration as the true global minimum.

Particle swarm optimization

Within this global optimization method, the enthalpy is calculated in parallel for a set of test configurations, the so-called swarm. Initially the positions of the test configurations (particles) and their momenta are chosen randomly on the potential energy surface [63, 84]. Iteratively the momentum of each test-particle are redefined with respect to:

- Its current momentum.

- The distance to its current personal best position (lowest enthalpy).

- The distance from the current best position found by all particles.

The momentum is used to describe the movement of each particle through search space. The particles fly above the potential energy surface, probing it while being prevented from being stuck in local minima . This movement is combined with local optimization steps. They reduce numerical noise on the individual test configurations and consequently enhance comparability between structures. Furthermore, the result is assured to represent a local minimum configuration on the investigated potential energy surface [85]. As all particles converge to the currently known global minimum configuration, its environment on the potential energy surface is investigated as well. Nevertheless, if the swarm heads for the 'wrong' funnel and the true global minimum is too far away, it is not going to be found.

Minima hopping method

The minima hopping method uses a single walker per run to sample the potential energy surface. It consists of two parts [72]: The inner part uses a series of molecular dynamic steps to move the test position from one basin to another one in the vicinity. The local relaxation of the geometry identifies the minimum of the supposed new basin. However, a 'new' minimum is not always accepted and can be rejected in the outer part. To favor search paths leading to low-energetic structures, the configuration is only accepted if the energy difference to the former minimum is below a certain threshold value δE (see figure 2.5).
Besides the mentioned threshold, escaping a local minimum provides another parameter: The
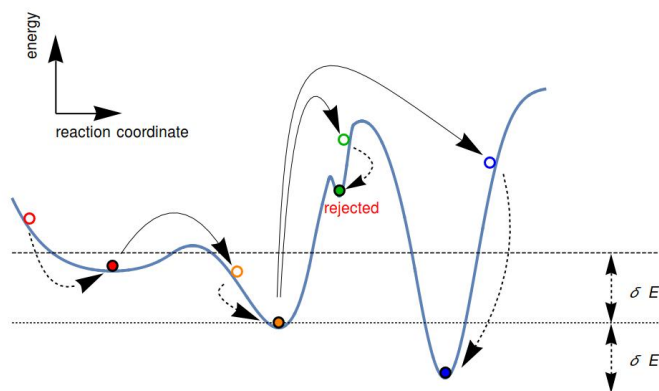
Figure 2.5: Sketch of the minima hopping algorithm. The blue curve represents a potential energy surface, solid arrows highlight MD steps to escape a local minimum and dashed arrows highlight relaxation processes. Configurations are highlighted by circles (○ - unrelaxed, ● - relaxed).
Starting at the left, hollow red configuration, the structure is relaxed and a local minimum is identified. Escaping this potential basin leads to the energetically even lower orange structure. The algorithm tries to escape this minimum again. Low kinetic energy does not enable the walker to leave this basin (not sketched). Higher kinetic energies lead the walker to the green configurations. However, the green local minimum structure is rejected as the difference in energy to the orange configuration exceeds δE. A further attempt to escape the minimum moves the walker toward the blue structures within δE. Local relaxation steps lead to a structure with an enthalpy lower than the current best. The configuration is accepted, as the energy difference between the consecutive minima is smaller than δE. The sketch is inspired by [72, 86].

kinetic energy provided to the walker to overcome the potential barrier. Following the Bell-Evans-Polanyi-principle, this parameter is decreased when new (formerly not visited) minima are found. To overcome energetic barriers and visit further regions of search space, the kinetic energy is increased when already visited structures are revisited. Therefore the enthalpy of all visited structures is saved to re-identify them.

These two parameters δE and the kinetic energy are both readjusted by the program at runtime, steering the algorithm towards low-energetic structures and preventing the algorithm from looping its path.

Furthermore, softening is introduced in the molecular dynamic steps to increase the efficiency [71]: To escape the current local minimum of the potential energy surface and follow the Bell-Evans-Polanyi-principle, the curvature of the potential energy surface is investigated at the current position to identify the most promising direction to evolve the current geometry. To follow this direction using molecular dynamic steps, the velocities of the atoms are rotated appropriately.

Besides the calculations of the enthalpies, the algorithm can be parallelized by creating several walkers. They each start with a different parameter set, a different region of the potential energy surface reducing the number of steps needed to identify a valid candidate for the ground-state structure [71]. Furthermore, one should follow a two-step-scheme of applying the minima hopping method first and a refinement step second. Through this strategy, calculation time

is saved in the first step, as the calculations of the enthalpy can be performed with a reduced precision. The conventional precision can be used at the refinement step to relax the structures and verify they are dynamically stable.

Chapter 3

Carbon clathrates

The word 'clathrate' has its origin in the Latin word 'clatratus', which can be translated to latticed or barred [87, 88]. The term has been introduced by H. M. Powell in 1948 [87, 89] to describe molecular cage structures enclosing other molecules. Nevertheless the term is not limited to molecules and is also used to describe crystalline materials. Clathrate vacancies are different from vacancies due to crystal defects, where the vacancy is created by an atom being shifted or missing in the periodic crystal structure. The structure itself creates the empty space which can be described as a cage. Filling the empty space within the cage, offers the potential of specifically varying the properties of the material. Furthermore, every atom or molecule building the framework crystal structure has four neighbors.

An example for clathrate structures are gas hydrates [89, 90]. Water molecules create the basic crystal structure which offers space to enclose the gas molecule. Figure 3.1 shows the example of a cage shaped similarly to a regular dodecahedron. Oxygen atoms mark the vertices. Each oxygen atom has two covalent bonds to the hydrogen atoms of its molecule and two hydrogen bonds to two neighboring water molecules. Edges are represented by the hydrogen atoms and their bonds to two neighboring oxygen atoms. As one of them is covalently bound and the other

Figure 3.1: Sample structure of water clathrates with water molecules forming an irregular dodecahedron [89]. Its vertices are defined by the position of the oxygen atoms. Solid lines represent covalent bonds and dashed lines sketch hydrogen bonds.

Figure 3.2: The periodic table of elements visualizes the role of each element when participating in clathrate structures [90]. The color of the bars indicates if the elements are known to be framework (red) or guest atoms (blue) in clathrate structures. The lengths of the bars refers to the number of known structures.

one is attached via hydrogen-bond, the edges of the cage bend easily with slight movements of the hydrogen atoms. Correspondingly, the cage differs from a regular dodecahedron.

Crystalline structures can be created by combining water dodecahedra with truncated hexagonal trapezohedra (14 faces) or 16-hedra of twelve pentagonal and four hexagonal faces ($\bigcirc^{12}\bigcirc^4$). These can be referred to as type-I and type-II clathrates [89]. Further types are mentioned by Dolyniuk *et al.* in [90]. The nomenclature of labeling clathrates by type originates from the naming of clathrate hydrate compounds [89, 90].

Clathrate structures are not limited to be created by molecules or water. The number of known clathrate structures with respect to the contributing chemical elements is visualized in figure 3.2. Accordingly, most of the known clathrate structures consist of a framework of silicon, germanium or tin atoms [90–92]. Regarding possible applications, there are suggestions to use these clathrate crystals in thermo electrics, for superconductors or even in lithium-ion batteries [90, 91, 93–99].

In contrast to the mentioned group-IV elements, no bulk clathrate structures with a carbon framework are known yet. Doped carbon clathrate structures have been predicted to be promising materials for superconductivity with a high critical temperature [99–102] and super hardness while offering low density [99]. At first this absence seems astonishing, as carbon is the simplest of these group-IV elements. But by private communication we know there has been several unpublished experimental attempts who have failed to synthesize such structures. Independent of these attempts, a paper of of Chan *et al.* [103] presents a powder x-ray diffraction pattern as proof of synthesizing carbon clathrates with nitrogen substitutions (see figure 3.3). However, due to the deviation of the experimental measurement from the theoretic anticipation, we believe that the experimental evidence is inconclusive.

Figure 3.3: The powder x-ray diffraction pattern of a potential sample of nitrogen-substituted carbon clathrates by Chan *et al.* [103]. Chan *et al.* compares an experimentally measured pattern (orange) to a theoretical prediction (purple) and further reference of barium and graphitic carbon nitride [103]. However, the orange curve does not match any of the four most intense predicted peaks (purple).

Other papers investigate carbon-based structures analog to silicon clathrates. They do not look for new geometries [104, 105]. One goal of the investigations of this thesis is to overcome the limitation of solely applying already known clathrate geometries to carbon. Therefore, the approach of section 3.1 is based on global structure prediction calculations. To gain more insights on the geometry of the structures and the relevant differences between the elements carbon, silicon and germanium, further geometric aspects are discussed in the upcoming sections 3.2 and 3.3.

In section 3.4 we shift the focus from carbon-only clathrate structures towards lithium-doped carbon structures with boron-substitutions. This change is motivated by work of Zeng *et al.* [40, 106].

3.1 Global structure prediction - clathrates of carbon-only scaffold structures

As already stated at the introduction of this chapter, the desired carbon structures contain vacancies. Furthermore, each carbon atom should only be present in its diamond-like sp^3-form, where each carbon atom has four carbon neighbors. To achieve these properties, several parameters of the global structure prediction search (see section 2.5) were chosen accordingly:

- Noble gas atoms were added to the composition of the unit cell to create vacancies in the structures. They are chemically inert and are supposed to reserve a spot in the unit cell for a future dopant or an empty vacancy. Using inert atoms to reserve space has already been successfully used predicting silicon clathrates [92]. The noble gases have been chosen with respect to the covalent diameter of the dopants lithium and sodium (see table 3.1):

    - **Neon atoms** are even smaller than carbon. So it is hardly useful to use them in our calculations.

    - **Argon atoms** are larger than carbon but smaller than lithium. They serves as a lower boundary to create small cages.

    - **Krypton atoms** are larger than argon atoms, but still smaller than lithium atoms. Atoms of this element are used to create vacancies of medium size.

    - **Xenon atoms** are larger than lithium atoms. So lithium is supposed to fit in vacancies produced by these place holders.

    - As **radon** is only slightly larger than xenon, a fictive **super-xenon** is used as an upper boundary for the investigation. Such an atom has been chosen to have double the diameter of xenon.

- As the optimal number of carbon atoms within the unit cell is unknown, a large variety regarding the number of atoms within the unit cell needs to be investigated. Besides one or two noble gas atoms per unit cell, the number of carbon atoms per unit cell has been varied from 6 to 60 in correspondence to benzene C_6-rings and C_{60} fullerens. This range includes the size of the unit cell of many known clathrate types [90, 105, 107].

- The thermodynamic stable phase of carbon at low pressures is graphite. There, each carbon atom has three neighbor atoms and forms sp^2 orbitals. Diamond is the sp^3-phase of carbon and stabilizes under pressure. As carbon is needed in its sp^3-form to create clathrates, the search is performed under a pressure of 50 GPa.

Table 3.1: Size of certain elements. The dimensions of the atoms and ions are approximated by double of the covalent or ionic radii [108–110].

alkali metals		group IV		noble gases	
				He	0.56 Å
Li$^+$	1.52 Å	C	1.52 Å	Ne	1.16 Å
Na$^+$	2.04 Å	Si	2.22 Å	Ar	2.12 Å
K$^+$	2.76 Å	Ge	2.40 Å	Kr	2.32 Å
				Xe	2.80 Å
				Rn	3.00 Å
				…	
			fictive super Xe	5.60 Å

To balance calculation time and precision, the calculations do not precisely follow the two-step-scheme, mentioned in section 2.5. An intermediate step has been added:

1. the global structure prediction runs use DFTB+ besides some DFT test calculations

2. removing the noble-gas atom of promising structures and relaxation via DFTB+

3. refinement via VASP (DFT)

1st step - global structure prediction

The global structure prediction calculations are based on the minima hopping method [71, 72]. The goal is to create many low-enthalpic structures with the appropriate number of carbon neighbors. A central point is the energy ordering of the created structures. At this stage, their enthalpies do not need to be compared with other publications yet. To save computational time, besides some initial DFT-runs, the interaction of the atoms has been described using the tight-binding code DFTB+ [61] with the matsci-0-3 parametrization of carbon [111]. The interaction of the noble gas atoms is described by a Lennard-Jones potential. The approach leads to an amount of $\approx 520 \cdot 10^3$ structures, where carbon not always forms cages around the noble as atoms. A brief overview on the variety of geometries is shown in figure 3.4. There, the noble gas and carbon atoms each arrange in planes in figure 3.4(a). Variations of this planarity are shown in figure 3.4(b) and 3.4(c). In contrast to figure 3.4(a) the planes containing the noble gas atoms in figure 3.4(b) show some honeycomb-like carbon structure separating the noble gas atoms from each other. Furthermore, these carbon-only layers are only one atom thin and show a hexagonal, graphite-like geometry. Similar layers also exist in figure 3.4(c), where they are corrugated and arrange the noble gas atoms linearly. In the structure of figure 3.4(d), the noble gas atoms are arranged linearly, too. However, in figure 3.4(d) the carbon environment of the noble gas atoms appears more uniform, channel-like, than in figure 3.4(c). At first, the structure seems to be an expansion of the honeycomb layer structure of figure 3.4(b), but in

(a) plane layers   **(b)** structured layers, top and side view

(c) corrugated layers   **(d)** channels   **(e)** cages
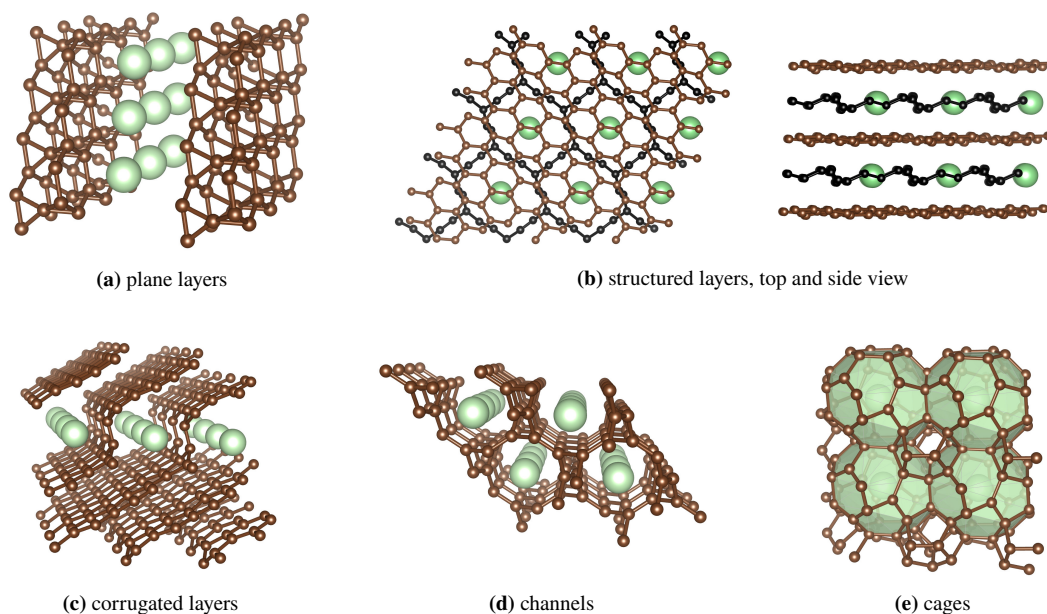
Figure 3.4: Selection of the variety of structures after the minima hopping search. A brief overview on the variety of the $520 \cdot 10^3$ structures received from global structure prediction runs. Carbon atoms are colored in brown and black to highlight different layers of the structure. Noble gas atoms are colored green.

figure 3.4(d) the carbon walls between neighboring channels do not always show the same thickness. Following this trend of separating the noble gas atoms, figure 3.4(e) shows an example structure where they are encapsulated in a carbon cage.

Several properties of the structures have been tried to be taken into account to classify the geometric arrangement. The most successful measures are the formation energy to select the most stable structures and the average number of carbon-carbon neighbors to neglect layered structures in the upcoming steps. Regarding the formation energy, only the five most stable structures of each composition were taken to the next investigation step if their formation energy was smaller than 1 $^{eV}/_{atom}$. To select sp^3-dominated structures, only structures with an average of at least 3.5 carbon-carbon neighbors were taken into account during a second, parallel selection round. By this criteria $58 \cdot 10^3$ structures were selected to be investigated at the next step.

2nd step

The stability of the selected structures from the minima hopping runs has been investigated by removing the noble gas atoms and relaxing the structures. The calculations are still performed with DFTB+ at a pressure of 50 GPa.
The method to select structures for the final refinement did not change. The enthalpy and number of carbon neighbor atoms are the criteria of two independent selections. The energetic selection threshold has been adjusted to $E_{form} < 0.1$ $^{eV}/_{atom}$. Showing on average of at least 3.9 carbon-
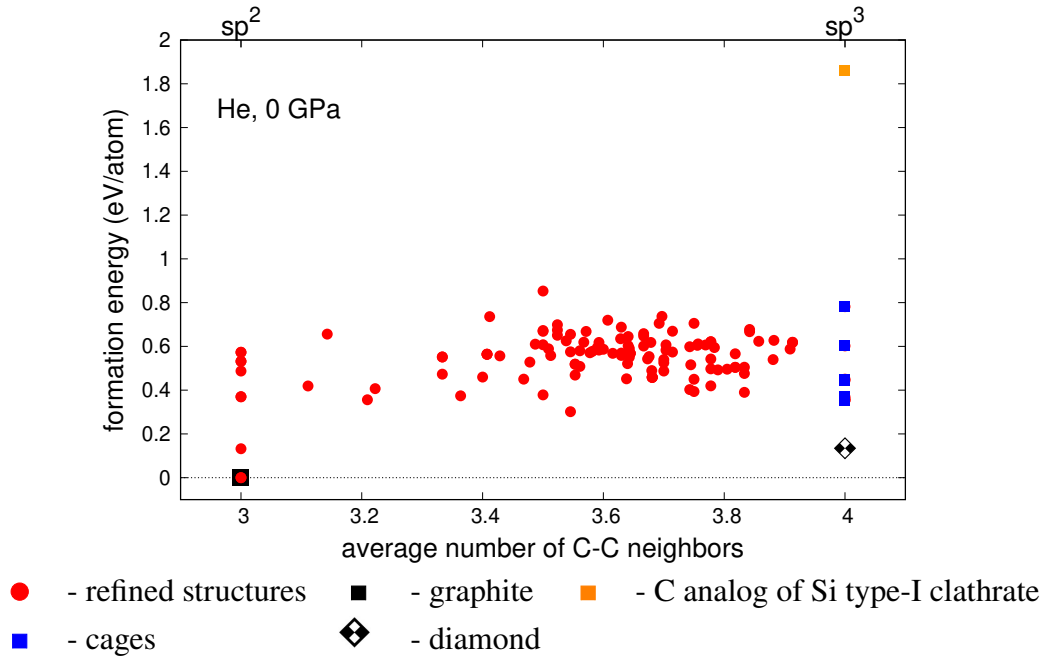
Figure 3.5: Formation energy of the refined structures of the global structure prediction approach filled with a helium atom. Horizontally, the structures are separated with respect to the average number of their carbon-carbon neighbors. Layered, graphite-like structures are shown on the left and structures and spatially connected carbon atoms are plotted on the right.

carbon neighbors is the other criterion. This selection does not prevent from accidentally selecting channel structures or doppelganger. So the selection criterion by the number of neighbors needed do be done partially by hand. Now, only 130 different carbon structures remained.

3rd step - refinement

In this last step the initial structures of the former selection step were used to replace the place holder noble gas atoms with helium, the smallest atom of the periodic system of elements. The structures are relaxed at a pressure of 0 GPa to investigate if the cages are large enough to host an atom inside them at low pressures or if even the smallest atoms disturb the electronic structure of the cage significantly. For comparability within the community, the structures were relaxed using VASP. Using DFT instead of DFTB+, was further enabled as the number of test structures was reduced by the previous two steps to only 130 remaining carbon structures. The formation energy of the structures is plotted in figure 3.5 with respect to the dominance of sp^2- and sp^3-orbitals to distinguish between layered graphite-like and diamond-like structures.

Figure 3.5 reveals the reference of graphite has been matched with intercalated graphite (figure 3.6(a)). On the right side of figure 3.5, above the reference of diamond, the formation energy of some cage structures ■ is shown. These structures are significantly more stable than
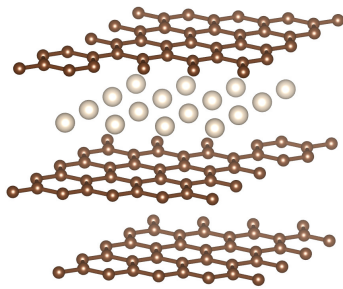
(a) **Intercalated graphite** with a HeC_{12} unit cell.

unit cell	$E_{form}/(\text{eV atom})$	carbon
HeC_{12}	0.004	sp^2
HeC_{17}	0.357	sp^3
HeC_{22}	0.363	sp^3

(b) **Formation energy** of the newly found, most stable structures.
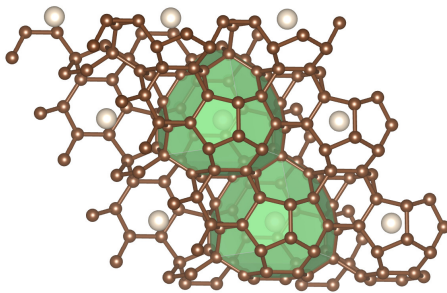
(c) **Cage** HeC_{40} with HeC_{17} unit cell.
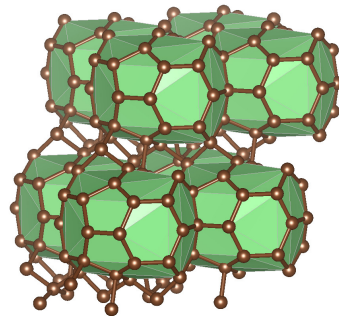
(d) **Cage** with HeC_{22} unit cell.

Figure 3.6: The most stable structures which contain carbon only in its sp^2 or sp^3 form. They were created by the global structure prediction approach and relaxed at a pressure of 0 GPa, while being filled with a helium atom.

the carbon analog ■ of a silicon type-I clathrate [75, 112–133]. The most stable of the clathrate structures ■ is still 225 $^{meV}/_{atom}$ less stable than diamond. This energetic difference translates to a temperature of 2600 K. To rationalize this number one can state it is significantly lower than the melting temperature of carbon ($T^{melt}_{diamond}(p_{norm}) = 3820$ K [134]). Therefore the formation of carbon clathrate structures cannot be seen as impossible. Adding thermal energy and external pressure to the system could further reduce the energetic distance. Additionally the question arises, if the main source of the difference in formation energy can be identified:

> Is the structure directly destabilized by the cage geometry or is the periodical linking via sp^3-bonds in three-dimensional space the main issue, which destabilises the whole structure?

Before transitioning to this specific investigation one should further remember, the investigation of this section is based on placeholder atoms creating the vacancy. Although the size of the placeholders has been chosen correspondingly to the size of actual atoms, concerning for the size of carbon they might not represent the best candidates. It would be better not to have to include such a parameter for the structural investigation.

The different cage geometries of the most stable, empty clathrates of figure 3.5 are shown in figure 3.7(a) - (d). The cages can be relaxed as carbon clusters, passivated with hydrogen (for more details see section 3.2.3). The formation energies of these structures are compared with each other and their bulk origin in figure 3.7(e). Transiting to clusters, the formation energies are reduced significantly, due to the change in composition. Moreover, the energetic spectrum becomes much more narrow. Ergo, stress is created by linking the cages in a 3D-crystal. In these example structures, linking the cages destabilizes the whole structure. The individual, relaxed cages are much more equivalent to each other regarding stability. The question if there are better candidates regarding the cage geometry motivates the investigation of further cage geometries in section 3.2.
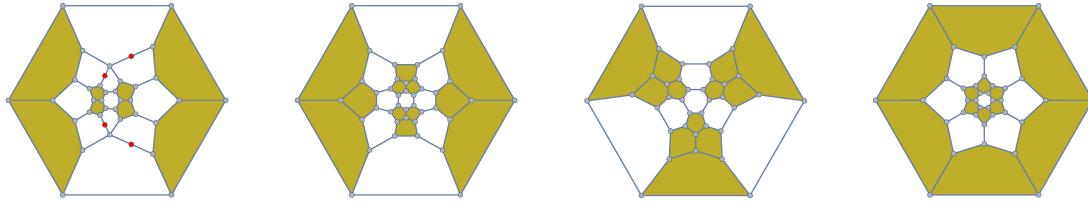
(a) **38 carbon atoms span** ⬠^{8}⬡^{12} :
Pairs of pentagons are surrounded by hexagons. The four red vertices only have two carbon neighbors within the cage.

(b) **40 carbon atoms span** ⬠^{12}⬡^{10} :
There are four groups of three pentagons, which are separated by hexagons.

(c) **36 carbon atoms span** ⬠^{12}⬡^{8} :
There are three stribes of four pentagons, which are separated by hexagons.

(d) **36 carbon atoms span** ⬠^{12}⬡^{8} :
There are two rings of six pentagons, which are separated by hexagons.
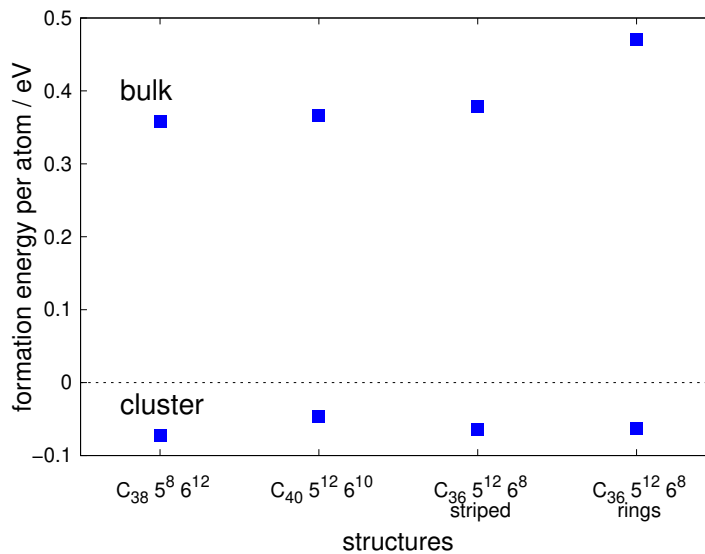
(e) **Comparison of the formation energies** of the identified bulk structures of the cages (a) - (d) and the formation energy of the isolated, passivated and relaxed cages.

Figure 3.7: Comparison of the cages of the most stable clathrate structures found by the global structure prediction runs. The net graphs of the cage geometries (a) - (d) are sorted by their increasing formation energy of the empty, bulk clathrate structure. All pentagons are colored to differentiate them better from any hexagon. The surrounding hexagons also represent a face. The corresponding formation energies are visualized in figure (e). There, the bulk structures are only composed of carbon. To push the carbon atoms in the clusters to their sp^3-form, the clusters are passivated with hydrogen.

3.2 Generalized cluster approach

To approach the questions that were risen by the last section, the stability of isolated cage structures is investigated in this section. The task of identifying bulk carbon clathrate structures is divided into two steps:

- identifying stable cage geometries

- periodically linking such cages in 3D space

This approach breaks the symmetry regarding the neighbors of an atom. Some neighbors are part of the investigated cage and others connect it to the surrounding residual geometry.
The geometry of the investigated polyhedra is interpreted by identifying each vertex with the position of an atom. From a molecular point of view, each edge represents the bond between two atoms. To enable equally stable bonds between neighboring atoms only convex polyhedra with regular faces are taken into account in section 3.2.1. Combining Platonic, Archimedean and Johnson solids, there are 110 structures to be investigated. The groups of prisms and antiprisms offer further candidates. More details about the difference in classifying these polyhedra can be found in section A.1. To enable a large variety of elements or molecules as dopants for the clathrate, cages with a large volume are preferred. One question to discuss later is if there is a general trend of stability of the isolated cages regarding their size, here approximated by the number of vertices.

A second topic is the classification of the vertices of the structures regarding stability. In [135] Nesper *et al.* solely takes planar angles into account when interpreting their results regarding the stability of clathrate structures. As cage geometries can be characterized by more measures than only planar angles, here the distribution of the different types of angles is going to be investigated to create a measure of stability. The first analysis in section 3.2.1 and section 3.2.2 is focused on geometry. DFT calculations as a reference are presented in section 3.2.3.
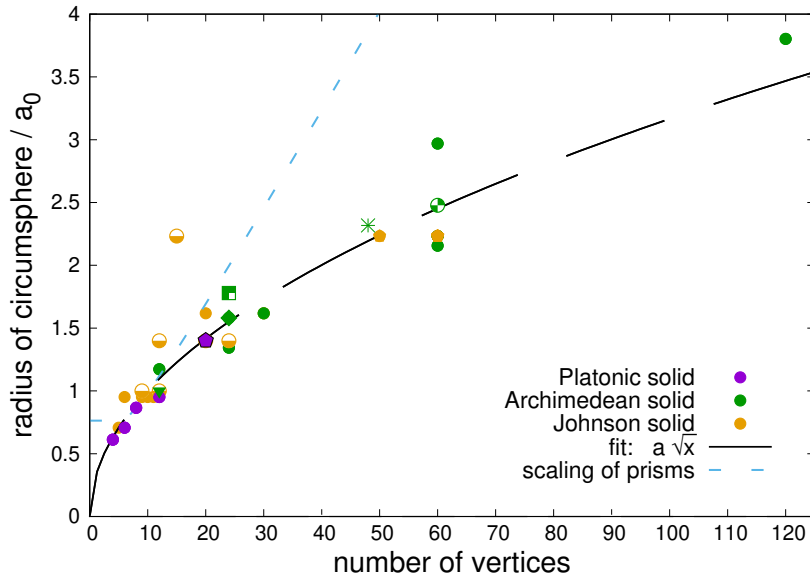
Figure 3.8: Scaling of the size of convex polyhedra with the number of vertices. Mathematica 10.0 [134] provides the circumsphere of 36 convex polyhedra with regular faces. These are the five Platonic solids, the 13 Archimedean solids, and 18 polyhedra from the Johnson solids. The radius of the circumsphere of these polyhedra is normalized by the length of the edges a_0 and scales approximately with the square root of the number of vertices (see black dashed line). Prisms and antiprisms are neglected for the fitted black line. They exist for an arbitrary even number of vertices and they provide their own law of scaling, as can be seen in the comparison of the two dashed lines (also see page A3). The individual plot symbols are listed in table 3.2.

Table 3.2: List of the polyhedra highlighted in section 3.2. On top, the different groups of polyhedra are listed with their individual color. Below, certain candidates of each group are listed with their combination of color and symbol.

Platonic solids	●	prism	●
Archimedean solids	●	antiprism	●
Johnson solids	●	self constructed	●
dodecahedron	⬟	... cupolae	◒
cuboctahedron	▼	augmented truncated tetrahedron	◕
truncated cube	■	augmented dodecahedron	⬟
truncated octahedron	◆	... augmented dodecahedra	⬟
great rhombicuboctahedron	✳	pentagonal prism	⬠
truncated icosahedron	◉	truncated hexagonal trapezohedron	⬟

(a) Dodecahedron ⬠

(b) Truncated Octahedron ◆

(c) Truncated Cube ▣

(d) Truncated Icosahedron 🌐

(e) Great Rhombi-cuboctahedron ✳

(f) Augmented truncated Tetrahedron ◐
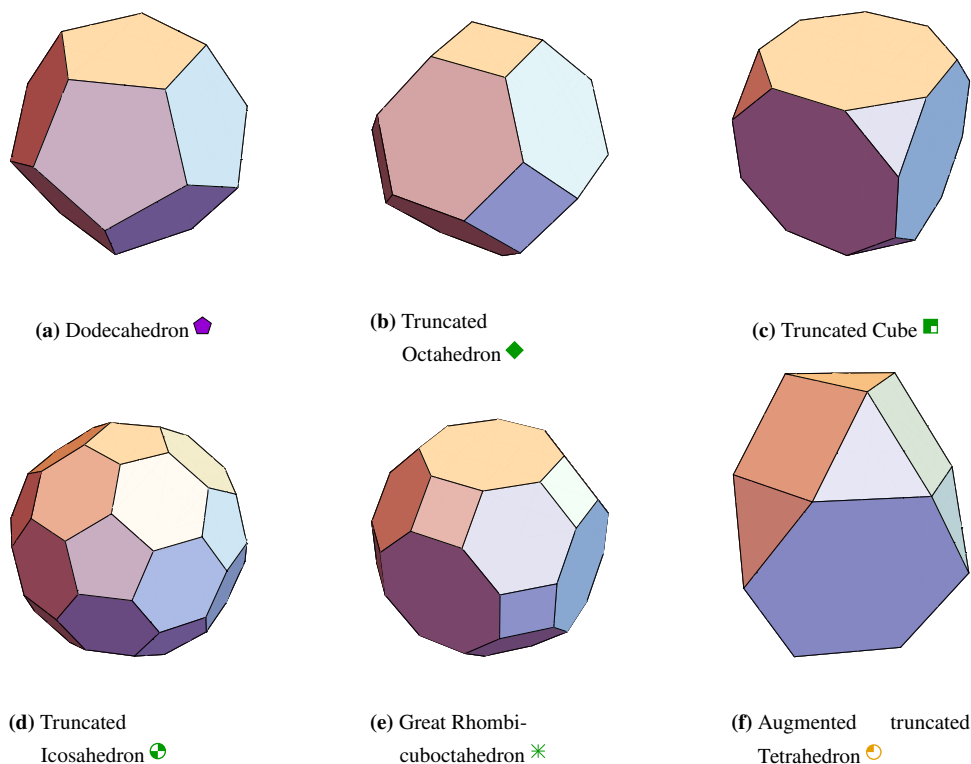
Figure 3.9: Sketches of highlighted polyhedra.

3.2.1 Analysis of geometries

The simplest gauge regarding the size of a convex polyhedron is the number of vertices. In figure 3.8 the scaling of the radius of the circumsphere of ideal, regular polyhedra is visualized. It scales with the square root of the number of vertices. This is not a surprise, as the number of vertices is an approximation to the size of the surface of the polyhedra. Highlighted polyhedra are listed in table 3.2 and examples are sketched in figure 3.9. Searching for stable cage geometries, the geometry of each vertex of the test-polyhedra is compared to the reference of diamond and certain geometric properties become important. Deviations from the reference geometry lead to molecular strain, destabilizing the structure. Liebmann *et al.* [136] mentions five different types of molecular strain:

1. torsion

2. bond angle distortion / Baeyer strain

3. linear bond stretching / compression

4. rotation, twisting of double bonds

5. electrostatic strain

(a) solid angle
$\Omega_{sp^3} = \pi$

(b) dihedral angle
$\theta_{sp^3} = 120°$

(c) planar angle
$\varphi_{sp^3} = 109.47°$
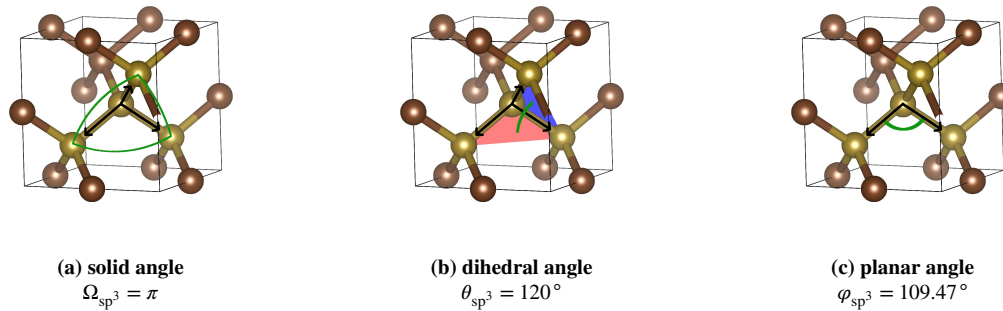
Figure 3.10: Sketches of the reference angles of diamond.

In this section torsion and bond angle distortions are studied via statistics about dihedral and planar angles θ and φ. The distribution of solid angles Ω is investigated, too. Baeyer strain is described as deviations from the 'natural' planar bond angles of carbon [136–138]: 109.47° and 120°. These reference angles correspond to a number of 4 or 3 neighbor atoms and the forming of sp^3 or sp^2 orbitals. The appearance of reference angles in diamond is sketched in figure 3.10. As the solid angle Ω is a two-dimensional angle, it can be used to describe each vertex with only one number. Nevertheless, the single value is not unique and does not reveal any shape of the spanned angle. Therefore the distributions of both dihedral and planar angles need to be investigated as well to open up further perspectives.

Focusing on Platonic, Archimedean and Johnson polyhedra variations of bond lengths do not appear. According to Liebman *et al.* this effect generally plays a minor role [136]. As cage geometries for clathrate structures are searched, each carbon atom shows four neighbors and no double bonds can appear.

The electrostatic strain is hardly of interest as long as solely neutral carbon atoms are used to built the framework. It can only appear due to a change of charge balance with respect to the passivation. Furthermore, carbon and hydrogen show a similar coefficient of electronegativity and therefore hardly any polarization of the structure due to passivation is expected ($\chi_C - \chi_H = 0.30$, [139]).

The characterization of the polyhedra is shown in figure 3.11 and uses the equations provided by section A.2 of the appendix. Each graph visualizes the distribution of solid, dihedral or planar angles. Platonic solids are marked purple • , Archimedean solids green • , Johnson solids yellow • , prisms • and antiprisms • are marked in two types of blue. Within each group, the polyhedra are sorted from few vertices on the left to many vertices on the right.

Each angle shows its own trend of similarity to the reference: Platonic, Archimedean and Johnson solids each show a trend of larger polyhedra leading to larger solid angles (figure 3.11(a)). This behavior is understandable when a polyhedron is approximated by a sphere. Locally the surface of a sphere becomes more and more flat when its radius is increased, up to the limit of an infinite radius, where the spanned solid angle is 2π. Regarding size, the largest solid angle of Platonic solids • can be found at the dodecahedron ⬠ :

$$\Omega_{dodecahedron} < \Omega_{sp^3}$$

(a) Internal solid angles Ω.

(b) Dihedral angles θ.

(c) Planar angles φ of the faces.
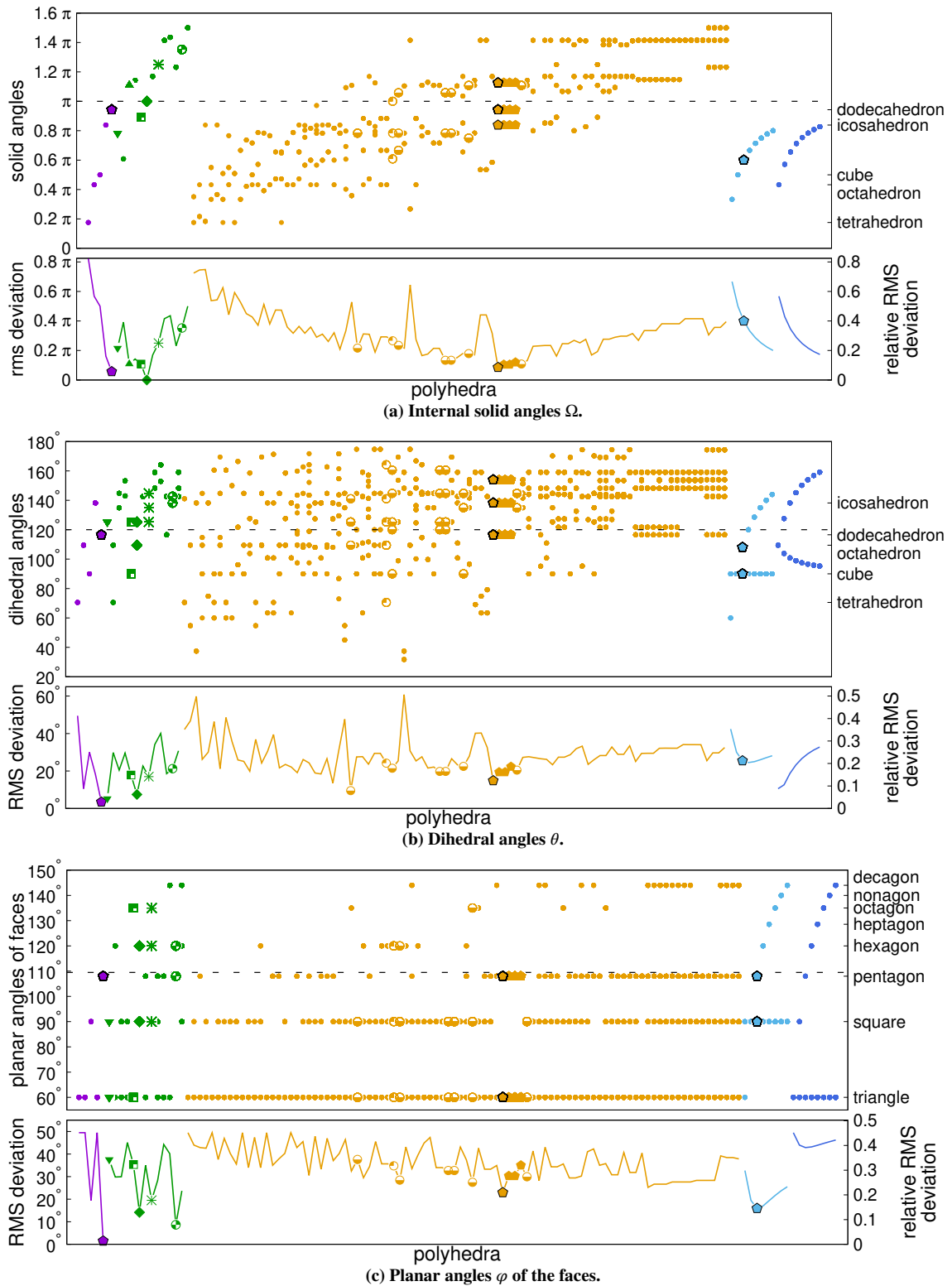
Figure 3.11: Characterizing polyhedra by their angles. Each group of polyhedra is distinguished by its color and the polyhedra of each group are sorted by size with few vertices on the left to many on the right. The dashed line is the reference of diamond. The symbols of highlighted polyhedra are listed in table 3.2. To each polyhedron and its angular distribution, the RMS deviation of the angles from the vertex-geometry of diamond is plotted in the lower graph. There, plotting the data as a line is used to guide the eye and to enhance the difference to the plot of all individual angles above.

Archimedean solids • contain solid angles angles larger and smaller than the reference, but only the truncated octahedron ◆ matches the reference angle at each vertex. As the vertices of a Johnson solid • are not identical, multiple solid angles can be found within each of these polyhedra. There are solids showing only angles smaller or larger than the reference and some contain angles of both ranges. Only the augmented truncated tetrahedron ☋ matches the reference with some of its vertices; its other are smaller and show a size of $0.608\,\pi$ and $0.784\,\pi$. Prisms • and antiprisms • show a different trend:

$$\Omega_{\text{(anti)prism}} \leq \Omega_{\text{sp}^3}$$

Although their solid angles are increasing with the number of vertices, the reference value constitutes the limit of infinitely large (anti)prisms.

The general trend of increasing solid angles translates only partially to dihedral angles (figure 3.11(b)). Now, Platonic solids are the only ones besides the cuboctahedron ▼ , where no multiple measures of dihedral angles can be found within one polyhedron. The dodecahedron ⬠ almost matches the reference. Despite the solid angle of the icosahedron being smaller then the reference, its dihedral angle is the one within Platonic solids • being larger than the reference. Archimedean solids • offer one, two or three different dihedral angles each, but none matches the reference. Each Johnson solid • offers multiple dihedral angles, too. Matches of the reference can only be found at the augmented hexagonal prism, elongated triangular cupola ⊖ , elongated triangular gyrobi cupola ⊖ , elongated triangular orthobi cupola ⊖ , meta biaugmented hexagonal prism and para biaugmented hexagonal prism.

Except the cube and the octahedron, each (anti)prism contains two different dihedral angles. At prisms • , one is always equal to $\pi/2$ and the second one increases with the number of vertices. Some dihedral angles of the hexagonal prism match the reference. Within antiprisms • , one of the two dihedral angles is increasing, while the other is decreasing. None of these angles matches the reference. Ergo, with respect to the number of vertices, antiprisms • show an increasing RMS-deviation of their dihedral angles, while the monotony of the RMS-deviation of prisms changes monotony with the hexagonal prism offering the smallest deviation of all prisms • .

The closest fit of Platonic solids regarding planar angles is offered again by the dodecahedron ⬠ , as it only shows pentagonal faces. Archimedean • and Johnson solids • show similar statistics. One trend can be estimated: The largest planar angle within these polyhedra is increasing with the number of vertices. Besides several structures contain pentagons and therefor partially offer a close fit to the reference, most of them as well contain small planar angles of $60°$, leading to a large RMS-deviation of the whole polyhedron. Two exceptions might be the truncated octahedron ◆ and the truncated icosahedron ⬡ . As these polyhedra only show square and hexagonal or pentagonal and hexagonal faces, their RMS-deviations of the planar reference are the lowest of all Archimedean solids • .

Similar to the dihedral statistics of (anti)prisms • , • , s their statistics of planar angles offer two branches of angles: One constant and one increasing. Both branches intercept at the previously
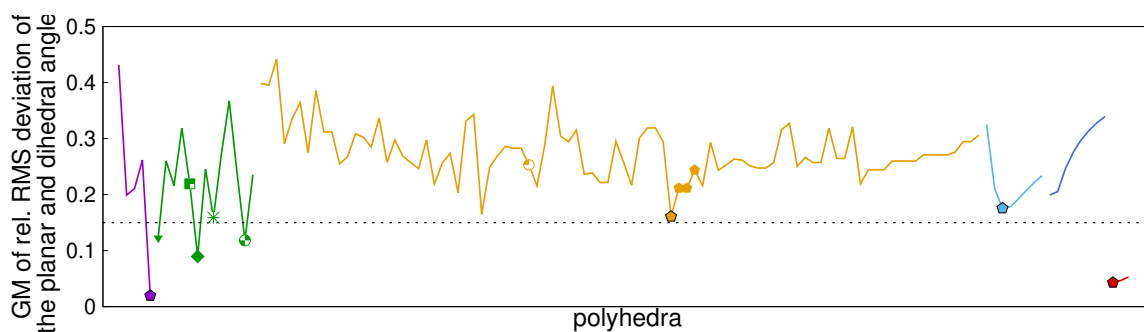
$$GM = \sqrt[4]{\frac{1}{|\{\varphi_i\}|} \sum_i \left(\frac{\varphi_i - \varphi_{\text{ref}}}{\varphi_{\text{ref}}}\right)^2 \cdot \frac{1}{|\{\theta_i\}|} \sum_j \left(\frac{\theta_j - \theta_{\text{ref}}}{\theta_{\text{ref}}}\right)^2} \tag{3.1}$$

Figure 3.12: Geometric mean of the relative RMS-deviations of the planar and dihedral angles presented in figure 3.11. The red curve represents the relaxed geometry of the separately constructed polyhedra of the upcoming section 3.2.2. $|\{\varphi_i\}|$ and $|\{\theta_i\}|$ are the numbers of planar and dihedral angles.

mentioned candidates, the trigonal antiprism (octahedron) and the square prism (cube). No angle precisely matches the reference, but pentagonal (anti)prisms come closest.

To simplify the view on the three statistics of the polyhedra shown in figure 3.11, a combination of the relative deviations of the angles from their reference value is visualized in figure 3.12. It focuses on planar and dihedral angles and plots the geometric mean of their relative RMS-deviation. Plotting this quantity is an approach to combine different measures of the vertices with their different reference values and number of values. Including redundant data should be omitted by only including two measures instead of three to describe 2D angles.

In figure 3.12 it is shown the dodecahedron ⬠ , cuboctahedron ▼ , truncated octahedron ◆ , great rhombicuboctahedron ✳ , truncated icosahedron ☺ and pentagonal prism ⬠ and the hand-constructed polyhedra • (see section 3.2.2) are relatively close fits to the reference. Besides these, the augmented dodecahedron ⬠ is supposed to be the best fit of the Johnson solids. Further combinations of a dodecahedron with pentagonal prisms are represented by further augmented dodecahedra ⬠ and show larger deviations.

The threshold regarding further investigations has been set to a mean deviation of 15 % to select the polyhedra most similar to the reference. This limit is in the range of the smallest deviations shown by the prisms. Antiprisms in general show a larger deviation than prisms. This trend is understandable as each vertex of any antiprism has four neighbors which are all placed within a solid angle smaller than π. In any prism there are only three neighbors within this range, so there are less restrictions.

Table 3.3: Possibilities to combine pentagonal and hexagonal faces at one vertex. Different combinations lead to different dihedral and solid angles θ_i, Ω. The simplest polyhedra containing ($⬠^2$ ⬡^{1})-vertices are shown in figure 3.13. In contrast to the other polyhedra, they contain edges connecting different types of vertices, leading to deformations of the polyhedron. The listed ($⬠^2$ ⬡^{1})-angles are calculated for an isolated vertex so no deformations are considered here. The values are printed as an orientation and different polyhedra containing ($⬠^2$ ⬡^{1})-vertices are listed in table 3.4.

Again, the reference of diamond cannot be reproduced by any of the listed vertices. On both, dihedral and solid angles, the values of ($⬠^3$)- and ($⬠^2$ ⬡^{1})-vertices enclose the reference angles.

vertex	appearance	θ_1	θ_2	Ω/π
	diamond, sp^3	**120°**		**1**
($⬠^3$)	dodecahedron ⬠	116.57°		0.943
($⬠^2$ ⬡^{1})	multiple representatives shown in figure 3.13	124.25°	131.18°	1.109
($⬠^1$ ⬡^{2})	truncated icosahedron ⬤	138.19°	142.62°	1.352
($⬡^3$)	hexagons on a plane	180°		2

3.2.2 Construction of further polyhedra

The investigation of angles in figure 3.11(c) shows pentagons and hexagons are the regular polygons offering the planar angles closest to the reference. Focusing at one vertex, there are four possibilities to combine these two faces: ($⬠^3$), ($⬠^2$ ⬡^{1}), ($⬠^1$ ⬡^{2}) and ($⬡^3$). As the possibilities of combining these vertices within one polyhedron have not been mentioned in the previous section in all detail, this investigation is presented in this section.

Each combination of these faces creates a different set of dihedral and solid angles, which are listed in table 3.3.

The dodecahedron ⬠ , which shows only pentagonal faces, and the truncated icosahedron ⬤ , where each pentagonal face is surrounded by hexagons, have already been discussed. The case ($⬡^3$) is not relevant for polyhedra, as the geometry is planar, but the combination of two pentagons and one hexagon ($⬠^2$ ⬡^{1}) at one vertex leads to several convex polyhedra which have not been discussed yet. Till now, they have been neglected as they lead to deformations. To construct the simplest examples of these new polyhedra, one can always start with the same basis sketched in figure 3.13(a). There, a ring of pentagons surrounds a hexagon creating six ($⬠^2$⬡^{1})-vertices. Different strategies of extrapolating this geometry lead to the different polyhedra presented in figure 3.13(b) - (e). The angular values found in these polyhedra are visualized in figure 3.14. In contrast to the polyhedra presented in figure 3.11, now the angles are calculated from relaxed carbon cages representing the appropriate geometries. The relaxation is achieved by DFT calculations further described in section 3.2.3.

The polyhedra of figure 3.13(b) - (e) are deformed and contain irregular faces, as edges connect vertices of different types. These deformations are also recognizable by the splitting of the angles in figure 3.14. Their composition and arrangement of vertices leads to an increasing deviation from the reference and corresponds to the distribution of vertices, listed in table 3.4. Correspondingly, the truncated hexagonal trapezohedron ⬟ contains the least deformations

(a) **Starting configuration** to create polyhedra which only contain ($\bigcirc^2$ $\bigcirc^1$)-vertices.

(b) **truncated hexagonal trapezohedron** 🔺 , 24 vertices span 12 pentagons and 2 hexagons

(c) **pentakaidecahedron**, 26 vertices span 12 pentagons and 3 hexagons

(d) **hexakaidecahedron**, 28 vertices span 12 pentagons and 4 hexagons

(e) **barrel shaped polyhedron**, 36 vertices span 12 pentagons and 8 hexagons

Figure 3.13: Net graphs of the constructed convex polyhedra with only pentagonal and hexagonal faces. The polyhedra (b) - (e) are constructed completing (a). All pentagons are colored to differentiate them better from hexagons. The surrounding hexagons also represent a face.

and is the most stable candidate of this group.

The geometric construction of polyhedra also has a practical background, as the polyhedra of figure 3.13(b), 3.13(c), 3.13(d) are mentioned by Dolyniuk *et al.* [90] and 3.13(b) - 3.13(e) by Zeng *et al.* [40] as part of bulk clathrate structures.

(a) solid **(b) dihedral** **(c) planar**
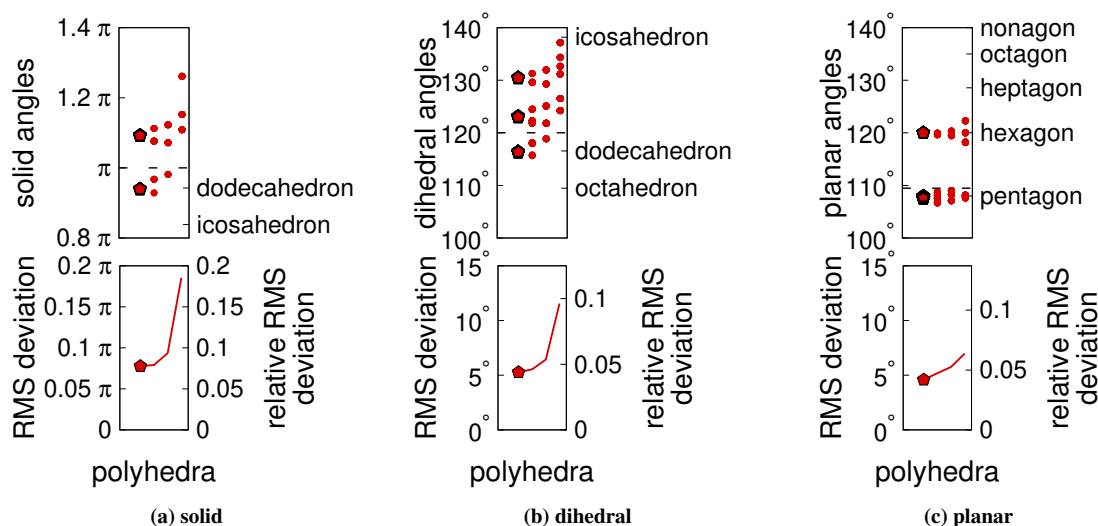
Figure 3.14: Angles of the constructed polyhedra analog to figure 3.11. Statistics about the presence of different vertices are listed in table 3.4. The deformation of the geometry increases with the size of the cluster and can be identified by the splitting of the angles.

Table 3.4: Overview on the presence of the different types of vertices in the constructed polyhedra shown in figure 3.13. The types of vertices are characterized by the types of neighboring polyhedra. The relative attendance of each vertex type is printed.

		number of vertices	types of vertices			
			$(\pentagon^3)$	$(\pentagon^2 \, \hexagon^1)$	$(\pentagon^1 \, \hexagon^2)$	$(\hexagon^3)$
Trunc. Hex. Trapezohedron	⬟	24	50 %	50 %	0 %	0 %
pentakaidecahedron	•	26	30.8 %	69.2 %	0 %	0 %
hexakaidecahedron	•	28	14.3 %	85.7 %	0 %	0 %
barrel shaped polyhedron	•	36	0 %	66.7 %	33.3 %	0 %

(a) Dodecahedron ⬠   (b) Truncated Octahedron ◆   (c) Truncated Cube ▣   (d) Truncated Icosahedron ⊕
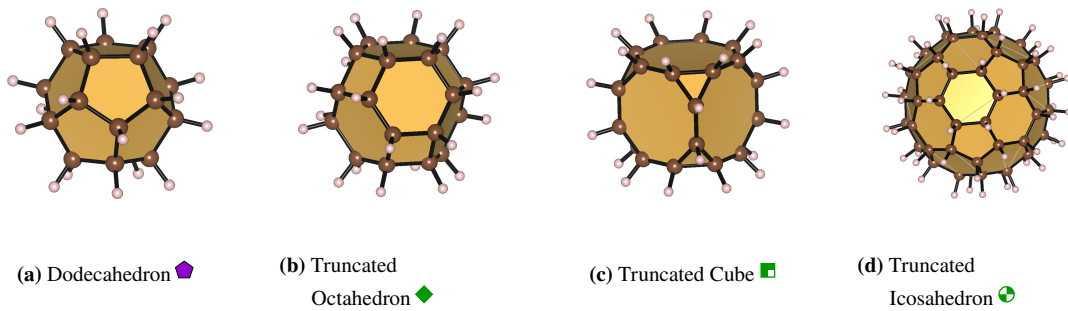
Figure 3.15: Geometry of passivated carbon cages made from the polyhedra of figure 3.9.

3.2.3 Comparison of formation energies

A selection of prototype cage-geometries with vertex-geometries close to diamond is presented in figure 3.12. However, not all of these need to be taken into account. As within the structure of diamond each atom has four nearest neighbor atoms, polyhedra only need to be investigated in DFT-simulations if each of their vertices are part of up to four edges. Additionally, to offer a valid option to connect the geometry with further atoms to form a solid crystal structure, at least one vertex needs to be part of up to three edges. Hence the investigation of all augmented dodecahedra ⬠ and ⬠ is skipped, as these polyhedra are variations of one dodecahedron with attached pentagonal pyramids and contain at least one vertex which is part of five edges and can not represent a sp^3-geometry at each vertex. To increase the field of investigated candidates, the cages found in the most stable clathrate solids ■ of section 3.1 are used for comparison (see figure 3.7 on page 30). All prisms • are included as well, as every vertex of every prism always has three neighbors and the similarity between two prisms can be used to verify the basic approach of combining the distributions of dihedral and planar angles into one quantity via equation (3.1).

To calculate the formation energies of the promising polyhedra via DFT, carbon atoms were placed at the positions of their vertices. Edges are represented by imaginary lines connecting the atoms. To enforce the formation of sp^3-orbitals, hydrogen atoms were added outside the polyhedron to each carbon atom with less than four carbon neighbors to compensate for these 'missing' neighbors (see figure 3.15). The initial distance between neighboring carbon atoms has been set to 1.5 Å (C-C) and 1.1 Å (C-H), which are values close to the reference distances in diamond and methane [75]. Furthermore, the initial positions of the hydrogen atoms were chosen with respect to the positions of the neighboring carbon atoms. Afterwards the geometry was relaxed in a simulation cell of constant volume using VASP (DFT) with an energy cutoff of 520 eV. The initial simulation cell is a cube with an edge length of 15 Å. Its size has been varied in corresponding simulations to verify, the applied 1x1x1 k-point grid allows a convergence of the enthalpy up to 2 $^{meV}/_{atom}$. From the physical point of view, this large cell size was chosen to ensure negligible interaction between the cluster and its copies due to periodic boundary conditions. No external pressure was applied to the system , so the enthalpy becomes identical to the internal energy.

(a) **number of vertices**   (b) **GM from equation (3.1)** of the RMS   (c) **relative RMS deviation of** φ_j
                                     deviations of φ_j, θ_j
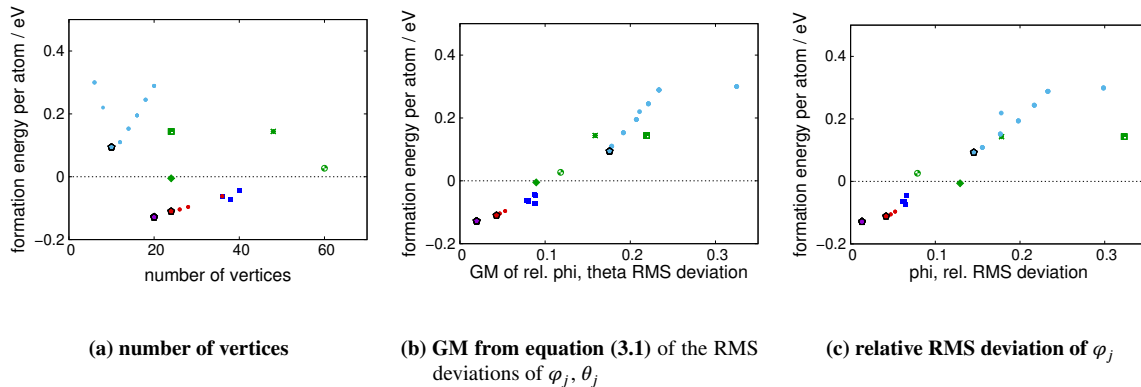
Figure 3.16: **Formation energies of isolated, relaxed, passivated carbon cages.** Each panel shows the forma-
tion energy of the same set of structures and compares their energy ordering concerning (a) the
number of vertices, (b) the geometric mean of equation (3.1) and (c) only the deviation of the planar
angles from the diamond reference.

In figure 3.16, the formation energy of the clusters is plotted with respect to the number of
vertices (a), the geometric mean of equation (3.1) (b) and the relative RMS-deviation of the
planar angles from the diamond reference (c). It is obvious that the carbon dodecahedron
cluster ⬠ energy-wise represents the best fit toward the diamond reference as it features the
lowest formation energy. The constructed polyhedra • deliver the second most stable structures
and the relaxed cages from the global structure prediction ■ (see page 30) are the last shown
structures with an obvious negative formation energy. The truncated octahedron ◆ shows a
formation energy of -5 meV/atom and all further shown structures are even less stable.

Regarding composition, there is only one exception from the 1:1 ratio of carbon and hydrogen
atoms in each structure (carbon content of 50 %): The cage ■ with the lowest formation energy
consists of 38 carbon atoms and is passivated with 44 hydrogen atoms (ratio 19:22, carbon
content of 43.2 %). This lower carbon content allows lower formation energies as, within a
binary phase diagram, the structure is placed closer to methane (1:4, carbon content of 20 %).
Besides representing the most stable structure here, the energetic distance between the dodeca-
hedron ⬠ and the convex hull of configurations of carbon and hydrogen is still 109 meV/atom.
The shape of the hull is defined by the formation energies of graphite, molecular hydrogen
and methane ($E_{\mathrm{form}}(\mathrm{CH}_4) = -377$ meV/atom [75]). Despite this energetic difference Robert J.
Ternansky *et al.* were able to synthesize dodecahedrane in 1982 [140, 141]. Even cubane
showing a positive formation energy of 220 eV/atom has been synthesized [142–144]. As its
bond angles are even more distorted, tetrane is even more unstable. Nevertheless efforts to
synthesize tetrane have been made [145].

Showing formation energies of at least 94 meV/atom, all prisms • are unstable. The pentagonal
prism ⬠ is their most stable candidate. This corresponds to the previously discussed geometric
approach.

Similar to the constructed polyhedra • , the cages ■ from the global structure prediction runs
offer a fundamental difference to the initially discussed polyhedra colored in • , • , • , • and
• . The arrangement of vertices leads to non-flat 'faces'. Therefore they offer more degrees of
freedom, as deformations are allowed. The most stable structure of the constructed ones • is

the truncated hexagonal trapezohedron ⬟ . This is in agreement with the interpretation of the geometric comparison in section 3.2.2 and the distribution of angles of the constructed polyhedra (table 3.4).

Comparing the different plots in figure 3.16, the structures in figure 3.16(a) are hardly ordered by their formation energy. The different abscissas in figure 3.16(b) and 3.16(c) allow for a more suitable ordering of the structures. In both plots, which in the following will only be referenced as (b) and (c), almost all points can be interpolated by a monotonically rising function. However, there are some fine differences between these two plots regarding this graph:

- The prisms • are sorted correctly in (b), but not in (c).

- The cages ▪ of the global structure prediction runs in (b) show two structures with almost the same geometric mean value, but with distinguishable different formation energies. The energetically lower structure represents the cage of figure 3.7(a). It differs from the other cages as four of its carbon atoms only possess two carbon neighbor atoms.
  In (c), their horizontal ordering parameter differ more from each other, but the structure of figure 3.7(a) is still not positioned left to all other ▪ .

- Despite being less stable than some prisms • , the great rhombicuboctahedron ✳ , is sorted left to all prisms in (b). In (c) the great rhombicuboctahedron ✳ is placed close to the heptagonal prism, which offers a similar formation energy.

- The geometric deviation of the truncated cube ▫ from the reference is overestimated in both cases. Nevertheless this artifact is even smaller in (b) than in (c).

- The truncated octahedron ◆ and the truncated icosahedron ◔ exchange their positions within the two plots (b) and (c). Regarding this detail, (b) is correct, as the truncated octahedron ◆ offers the lower formation energy and is plotted left of the truncated icosahedron ◔ .

All in all, in figure 3.16(b) the approach of the geometric mean of equation (3.1) shows its advantages against solely investigating the distribution of planar angles (figure 3.16(c)) and offers a more precise ordering by stability.

Regarding the most stable cages found, the next questions arise:

- How large is the space inside the carbon cages? Which elements can be used as dopant?

- How are the cages optimally linked to create a periodic structure with only diamond-like sp^3-orbitals?
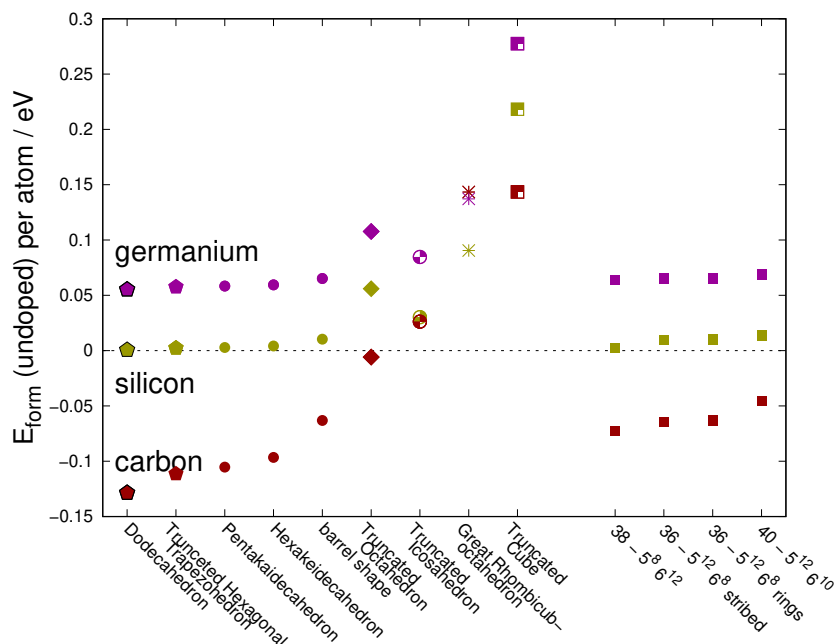
Figure 3.17: Comparison of the formation energy and stability ordering of polyhedra made of carbon, silicon or germanium. The color represents the element forming the cluster and does not highlight the structure as Archimedean solids any more. All polyhedra are passivated with hydrogen as described in section 3.2.3. The formation energy of the most important undoped polyhedra from section 3.2 are compared with each other. Regarding these empty, but passivated cages, all structures besides $38 - \hexagon^8 \pentagon^{12}$ show the same composition of $(C / Si / Ge)H$. This cage structure with 38 vertices deviates and uses a ratio of $(C / Si / Ge)_{19}H_{20}$.

3.2.4 Verification with further group-IV elements

As already stated at the beginning of this chapter, clathrate structures are known for all group-IV-elements but carbon. The geometric approach starting in section 3.2.1 first focuses on the similarity of the geometry of vertices to the sp^3-geometry of diamond without investigating a particular group-IV element. Besides identifying stable, isolated carbon cage structures, bulk carbon clathrates have not been found experimentally yet. As this is an astonishing contrast regarding the next group-IV elements, silicon and germanium, the previously discussed geometric approach needs to be re-evaluated with these two elements.

The most stable cage geometries of figure 3.16 have been recreated and relaxed using silicon and germanium. In figure 3.17 the stability ordering of these structures is visualized and compared to the carbon analog. In the graph the abscissa labels the different polyhedra. All structures, but the four on the right, originate from the geometric approach. Those have been created with the global structure prediction search of section 3.1. In figure 3.17 the structures of each group-IV element follow a similar trend of stability ordering. The formation energy typically increases from carbon to silicon and germanium. Despite the low energetic structures of each element

Table 3.5: Inter-atomic distances of the pure sp^3-phases of carbon, silicon and germanium at 0 GPa [75]. The nearest-neighbor-distance of silicon (germanium) is more than 50 % (60 %) larger than of carbon. Comparing polyhedra, this translates to an even larger increase in volume.

element	inter atomic distance (Å)	normalized distance	$(\text{normalized distance})^3$
C	1.55	1	1
Si	2.37	1.53	3.6
Ge	2.50	1.61	4.2

Table 3.6: Bond energies of carbon, silicon and germanium. [148, 149]

x	$E_{\text{bond}}(x\text{-}x)/\text{eV}$	$E_{\text{bond}}(x\text{-H})/\text{eV}$	$E_{\text{bond}}(x\text{-H})/E_{\text{bond}}(x\text{-}x)$
C	3.59	4.26	1.19
Si	2.30	3.30	1.43
Ge	1.95	2.99	1.53

show a similar trend to each other, there are exceptions in the energy ordering of the structures higher in energy: When comparing carbon with silicon, the truncated octahedron ◆ and the truncated icosahedron ☉ exchange their positions regarding their formation energy. Germanium exhibits the same ordering as silicon.

The great rhombicuboctahedron ∗ highlights another difference in behavior of the three elements. Here, the silicon structure has the lowest formation energy, while germanium and carbon exhibit a higher energy similar to each other. Furthermore, the formation energy of the carbon great rhombicuboctahedron ∗ is almost the same as the carbon truncated cube ▪ . The truncated cubes of silicon and germanium represent even higher formation energies.

Independent of any polyhedron, the most obvious difference between the three chemical elements is the charge of their isolated atomic cores and correspondingly the number of all their electrons. A higher number of electrons increases the size of the atom and the nearest neighbor distance (see table 3.5). However, atoms of carbon, silicon and germanium all possess four valence electrons. The larger inter-atomic distances also lead to lower bond strengths (see table 3.6). Furthermore, silicon and germanium atoms form sp^3-orbitals in their thermodynamic stable phase at low pressures and not a graphite-like sp^2 phase like carbon [75, 146, 147].

Investigating the bond energies (table 3.6), it is visible that all bonds are weakened when transitioning from carbon to silicon and germanium. Hereby, the transition from carbon to silicon represents a larger step than the change from silicon to germanium. This agrees with the former results, where the behavior of germanium and silicon has been similar. However, the passivating x-H-bonds always become stronger with respect to the corresponding x-x-bonds building the polyhedron. Therefore, when comparing carbon with silicon and geranium, bond deformations translate differently to a change in energy. This trend can be seen more easily

Table 3.7: Geometric comparison of the truncated octahedron and truncated icosahedron.

	truncated octahedron ◆	truncated icosahedron ☻	great rhombicuboctahedron ✳
number of faces	$\square^6 \hexagon^8$	$\pentagon^{12} \hexagon^{20}$	$\square^{12} \hexagon^8 \bigcirc^6$
number of vertices	24	60	48
solid angle	π	$1.352\,\pi$	$1.25\,\pi$
dihedral angles	109.47°, 125.26°	138.19°, 142.62°	125.26°, 135°, 144.74°
planar angles	90°, 120°	108°, 120°	90°, 120°, 135°
vertex type	$(\square^1 \hexagon^2)$	$(\pentagon^1 \hexagon^2)$	$(\square^1 \hexagon^1 \bigcirc^1)$
rel. amount of hex. faces	$8/14 \approx 0.571$	$20/32 = 0.625$	$8/26 = 0.308$

comparing prism structures in figure 3.18. There, carbon, silicon and germanium all show their most stable candidate to be the pentagonal prism (10 vertices). Leaving this minimum and forming further prisms, angular strain is added to the cluster and the formation energy rises. However, this rise is more prominent in the case of carbon than with silicon and germanium. With silicon and germanium the deviation from optimal bond angles does translate to a smaller increase in energy.

Going back to the polyhedra, their geometric differences need to be discussed. Vertices of the truncated octahedron ◆ connect a square with two hexagonal faces, vertices of the truncated icosahedron ☻ appear between a pentagonal and two hexagonal faces and vertices of the great rhombicuboctahedron ✳ are even shared by three different types of faces (one square, one hexagon and one octagon). It is possible to express this difference by a variety of measures (see table 3.7). As all these polyhedra contain hexagonal faces and connect them with different n-gons, one might investigate the stability of all appearing n-gons as isolated ring structures. However, the faces of the polyhedra are flat and the rings are twisted in their ground-state geometry. It is possible to force the rings to a flat geometry, but this can lead to accidentally adding further strain. Therefore this strategy should not be followed here. However, the low presence of hexagonal faces at the great rhombicuboctahedron ✳ (30 % vs. ≈ 60 % at the truncated octahedron ◆ and the truncated icosahedron ☻) corresponds to its higher formation energy and hexagons offering low angular strain.

To verify the energetic differences of ☻ , ◆ and ✳ are not artifacts of the applied PBE-functional, the clusters were relaxed using different exchange-correlation-energy functionals. The stability ordering of the three clusters of the three elements with respect to three different functionals is compared in figure 3.19. In comparison of the functionals, the stability ordering of the geometries of each element does not change.
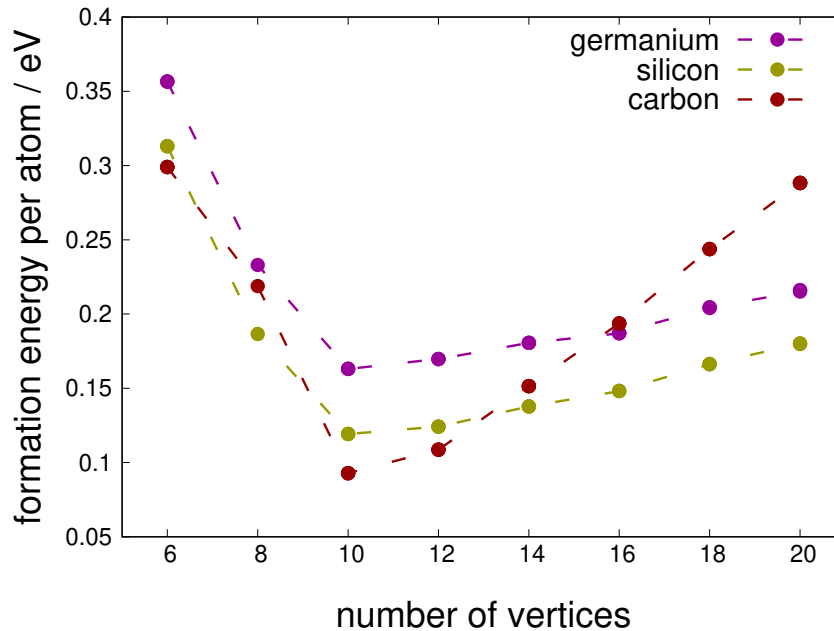
Figure 3.18: Prisms: Comparison of the formation energy of carbon, silicon and germanium structures. All prisms are relaxed and passivated with one hydrogen atom per cage atom. The data points of each element are connected to guide the eye and to highlight that the angular strain increases the formation energy of the carbon structures more than of silicon and germanium structures.
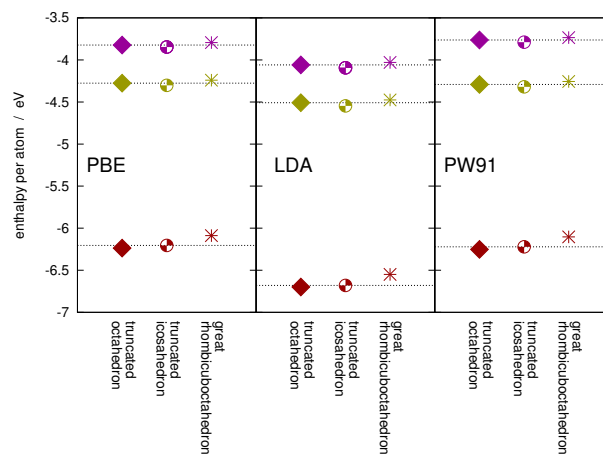
Figure 3.19: Comparison of the stability ordering of the truncated octahedron ◆ , truncated icosahedron ◑ and great rhombicuboctahedron ✳ . The polyhedra were built with carbon ●, silicon ● and germanium ●. All polyhedra are passivated with hydrogen and relaxed using the different exchange-correlation-energy functionals PBE, LDA and PW91 [46, 49, 50, 150, 151]. As all cluster have the composition xH, the enthalpy per atom can be used to investigate the stability ordering of structures with the same x. Each horizontal line guides the eye and highlights the energy of the second most stable structure.
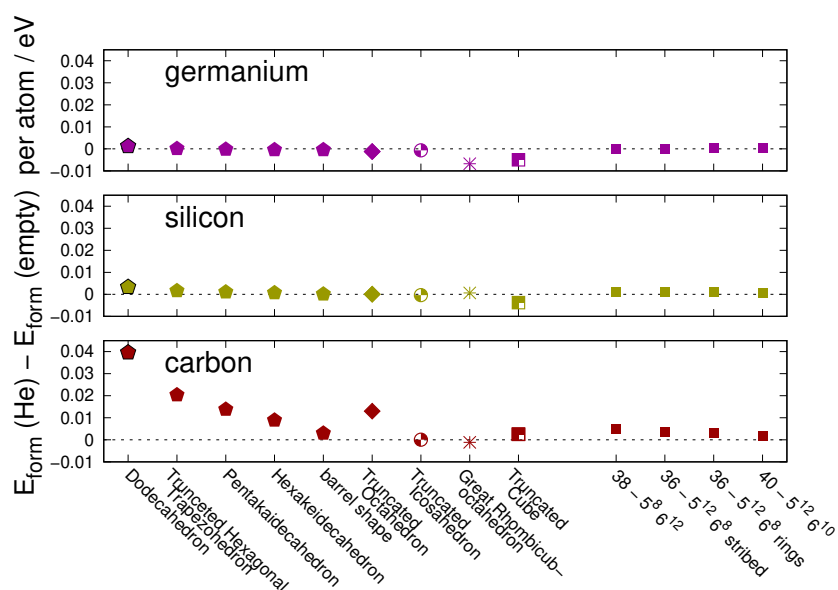
Figure 3.20: Change in formation energy due to filling the cages of figure 3.17 with helium. This energetic change allows an estimation of the cluster size.

To estimate the possibility of filling the cages, the cluster of figure 3.17, each has been filled by a helium test atom. Helium has been chosen to test the structures for small atoms. When the filling atom is too large, its electrons distort the geometry of the atoms forming the cage and the formation energy increases. The resulting changes in formation energy are shown in figure 3.20. It is visible, in contrast to carbon, the formation energy of any of the silicon and germanium structures hardly changes. This can be explained with the amount of space the clusters offer the guest atom. In table 3.5, the (normalized distance)[3] approximates the gain in volume when transitioning from carbon to silicon or germanium cages. Correspondingly, the largest change in formation energy due to filling can be identified at the carbon dodecahedron ⬠ , as the dodecahedron is the smallest shown cage regarding the number of vertices.

This trend of the most stable, empty carbon cages to be destabilized by the test atom the most, leads to the dodecahedron and the constructed polyhedra showing around the same formation energy. Regarding silicon and germanium, these four structures show similar stability independent of being empty or being filled with helium.

Looking for dopable carbon clathrate structures, it can be concluded it does not make any sense only to investigate the most stable cage structures. The constructed structures on the right of figure 3.17 and 3.20 perform well regarding the stability in both cases. This is also reasonable, as they have been identified during the global structure prediction search using placeholder atoms larger than helium.

This result of low-enthalpic carbon-polyhedra structures agrees with the suggestion of Nester *et al.* [135]. There, the energetic change of bulk carbon structures due to stretching was investigated without adding further atoms inside the polyhedron. The most favored structures of Nester *et al.* are clathrate-I and -II structures. They contain dodecahedra, tetrakai-decahedra

(truncated hexagonal trapezohedra) and hexakai-decahedra (see figure 3.13). In the present investigation, these three helium-filled polyhedra show a similar formation energy.

3.3 Linking polyhedra and enforcing sp^3-orbitals

The investigation in section 3.2 reveals dodecahedral carbon clusters are the most stable of the investigated carbon clusters. Possibilities of direct linking it perodically with itself are investigated in section 3.3.1. The issue leads to the question which concerns the failure of experiments to discover stable bulk phases of carbon containing dodecahedra, besides Robert J. Ternansky *et al.* synthesizing dodecahedrane clusters in 1982 [140]. This contradiction was already mentioned at the end of section 3.1, where the problematic of linking cages periodically in 3D space has already been hinted. Dolyniuk *et al.* [90] lists several clathrate geometries containing (pentagonal) dodecahedra. As it cannot tile 3D-space alone ($4\pi/\Omega \notin \mathbb{N}$), I emphasize other details and focus on the quasi-1D case of dodecahedral carbon to investigate the change in formation energy (section 3.3.1). Placing CH_2-groups properly between cages could reduce the formation energy of the total structure, but it shifts the composition towards containing more hydrogen and defeats the purpose of these hydrogen atoms as place holders. It is described as quasi-1D, as the dodecahedra ⬠ are still three-dimensional objects, but they are linked in a row. According to section 3.2 the truncated octahedron ◆ is another good candidate to investigate the problem of periodical linking. The polyhedron solely offers solid angles of π, precisely $1/4$ of the full solid angle. Furthermore, the formation energy of the passivated cluster is negative (see figure 3.16). The possibility of tiling space and forming type-VII clathrates with truncated octahedra is investigated in section 3.3.2.

In section 3.3.3 an alternative strategy regarding tiling 3D-space is discussed, which is based on spirals instead of any polyhedron.

3.3.1 Rows of dodecahedra in quasi-1D

The simplest way of linking dodecahedra is by stacking them (see figure 3.21(a)). Neighboring dodecahedra share faces and each vertex of such a face has two neighbors within this face, a third in one dodecahedron and a fourth neighbor in the second dodecahedron. At an isolated dodecahedron cluster, the hydrogen atoms are oriented to minimize the enthalpy of the structure while enforcing sp^3-geometry of the carbon orbitals. However, the full solid angle of 4π and the internal solid angle of the dodecahedron are not commensurable ($4\pi/\Omega_{\text{dodecahedron}} \approx 4.24$). In contrast to cubes or the truncated octahedron, dodecahedra cannot fill three-dimensional space without creating further polyhedra. When stacking dodecahedron clusters, it is recognizable how the positions of the 'new' carbon atoms deviate from those of the hydrogen atoms by an angle of 5.8° (see figure 3.21(b)). This change in angle and the change in composition increases the formation energy of the structure (see figure 3.21(f)).

Thinking about an alternative strategy, one might wonder if dodecahedra can at least share a single vertex. As every vertex precisely needs four neighbors and this geometry would lead to six neighbors, dodecahedra cannot share only one vertex. Sharing an edge between neighboring dodecahedra is also not possible as this geometry leads to five neighboring atoms. However, it is possible to use one vertex of one dodecahedron as the 4th neighbor of a vertex of a second dodecahedron (see figure 3.21(c)). Applying this strategy, the angles are conserved. Proceeding this way, neighboring dodecahedra can share as well two or five vertices (figure 3.21(d) and (e)). The first case leads to distortions in the geometry as square planar angles appear. In the second case, not only two planar, but five dihedral angles per dodecahedron and link are changed to square angles and the formation energy rises even higher.

All formation energies are plotted in figure 3.21(f) with respect to their composition. The isolated cluster, the single bond and the face-sharing case all show a similar distance to the convex hull(gray dashed line). Although the extrapolation via the yellow line hints to the isolated cluster offering the lowest distance to the hull. Furthermore, the extrapolation hints a lower energetic boundary regarding carbon-only, dodecahedron-based clathrate crystal structures. This limit is shown less than 100 meV above diamond. Consequently there may be space to improve upon the structures from the global structure prediction runs ■ of section 3.1.

(a) Stacked / face-sharing dodecahedra.

(b) Overlay of a single passivated and stacked dodec-ahedra.

(c) One bond.

(d) Two bonds.

(e) Five bonds.

(f) **Formation energy** of the attempts.
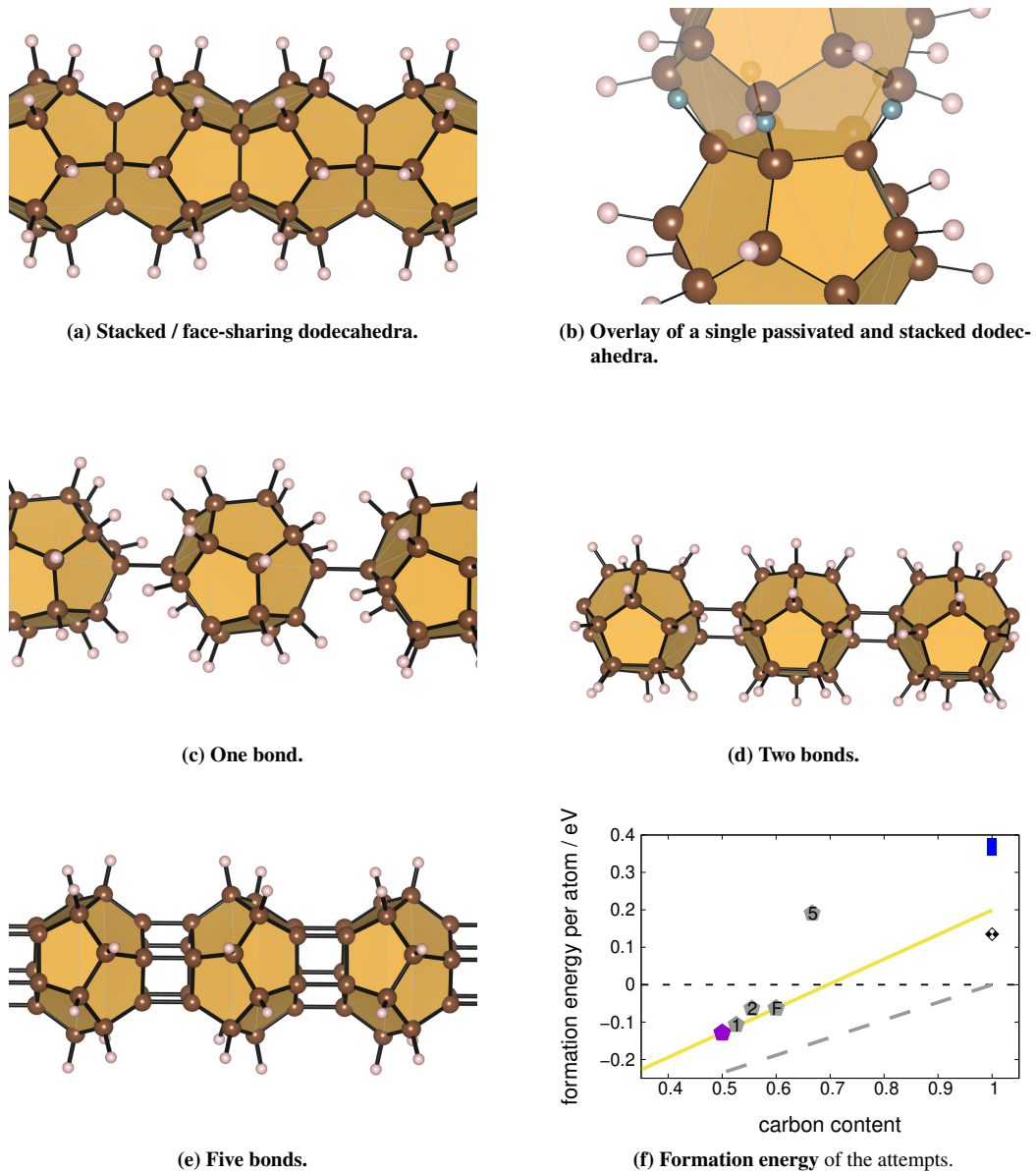
Figure 3.21: Linking dodecahedra ⬠ **in quasi-1D.** There are four main possibilities to directly link dodecahedra in an infinite row. Panel (a) displays the possibility to share faces between neighboring dodecahedra. (b) highlights the resulting positional change of the fourth neighbor atom. Hydrogen atoms are marked blue when they are substituted with carbon while linking the dodecahedra. The positions of these marked atoms and the corresponding carbon atoms deviate by an angle of $5.8°$. The sketches (c) - (e) present the possibility of links via one, two or five 'bonds' between neighboring dodecahedra. The formation energy of these structures is plotted in (f) with respect to their composition. The bottom dashed line marks the convex hull, connecting graphite and methane. The yellow line extrapolates the connection of the isolated cluster and the face-sharing case 'F'. The other data points are labeled with the number of links neighboring dodecahedron. The extrapolation hints to a fictive carbon-only structure, which is energetically positioned above diamond, but below the results of the global structure prediction runs ■ from section 3.1.

(a) 1D: single link

(b) 1D: sharing hexagonal faces

(c) 1D: sharing square faces

(d) 2D: sharing hexagons

(e) 2D: sharing hexagons and squares

(f) 2D: sharing squares

(g) 3D: tilling space completely using only truncated octahedra ◆ . Four colors are used to differentiate the polyhedra from their neighbors and to highlight the periodicity.

(h) Formation energy: The yellow lines interpolates the data points.
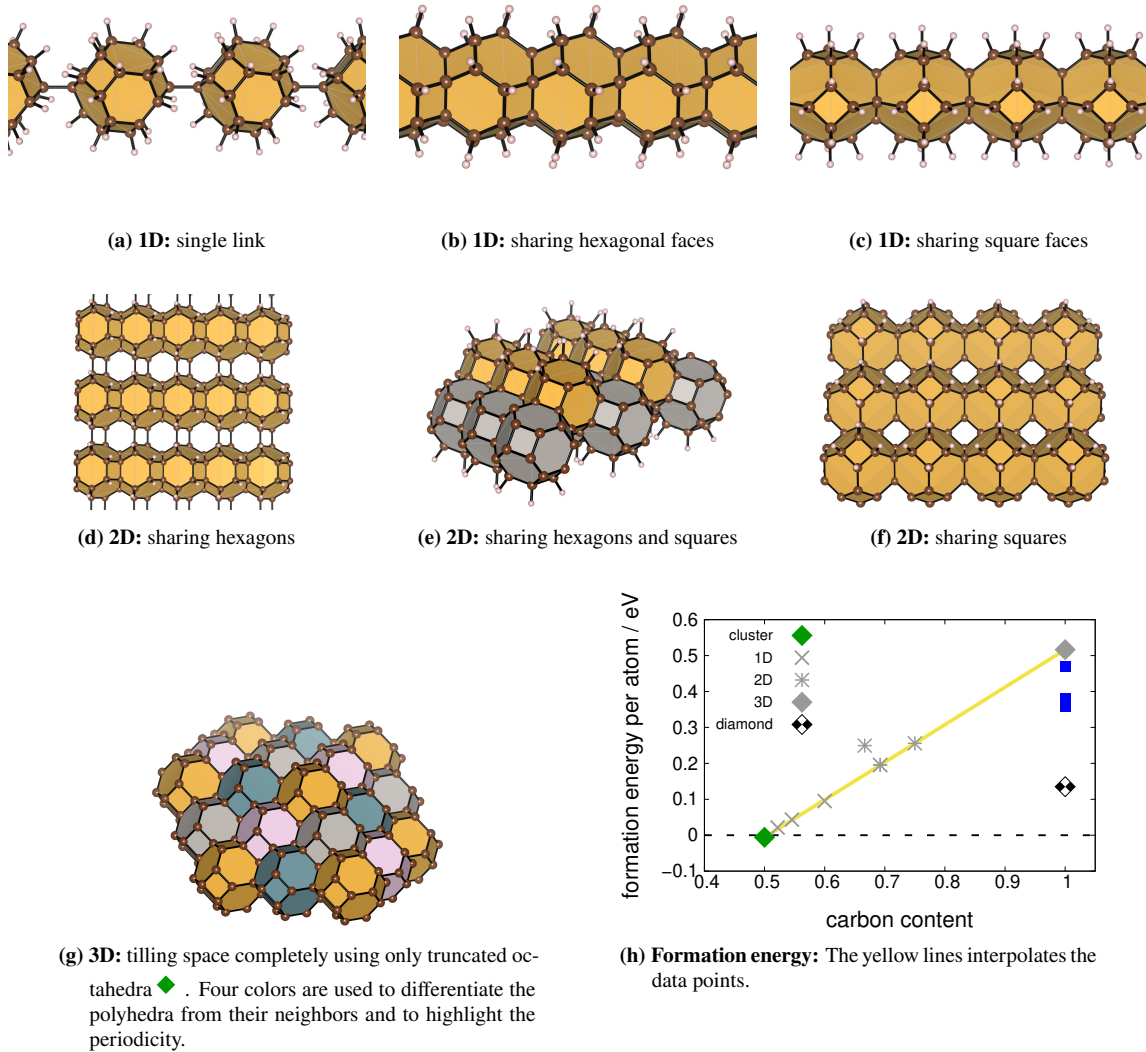
Figure 3.22: Different possibilities of tilling space in a different number of dimensions only using truncated octahedra ◆ **.** The 1D-case is covered by (a) - (c), 2D by (d) - (f) and 3D by (g). Panel (h) shows the formation energy of these structures in a phase diagram. The yellow line interpolates the cases of the isolated cluster and bulk. Most of these structures are positioned on this line. The bulk case does not improve upon the results of the global structure prediction runs ■ from section 3.1.

3.3.2 Linking truncated octahedra

The truncated octahedron ◆ possesses hexagonal and square faces. More importantly, at each vertex these faces span a solid angle of π, precisely ¼ of the full solid angle. This solid angle and the symmetry of the truncated octahedra allow for tiling 3D-space using only copies of itself (see figure 3.22(g)). This 3D crystal structure is also known as a clathrate type-VII structure. Furthermore, the isolated cluster is one of the most stable structures found in figure 3.16. This makes this polyhedron an interesting candidate to investigate the stability of its periodic links within a different number of dimensions (see figure 3.22). The formation energies of these structures are shown by figure 3.22(h) with respect to their composition. There, the formation energy of all structures, but one, is placed on a line. Ergo only the change in composition leads to the change in formation energy and no further deformations appear during the linking process. Only the square-sharing 2D-structure (figure 3.22(f)) shows an increased formation energy, which can be explained by the position of the hydrogen-atoms of neighboring cages. Their close distance lets them interact and destabilizes the structure.

Only the isolated cluster ◆ shows a negative formation energy. Furthermore, figure 3.22 shows the 3D carbon clathrate-VII structure is less stable than the resulting structures ■ of global structure prediction from section 3.1.

As already indicated, sometimes structures can be stabilized under pressure. The formation energy of the bulk, carbon only, clathrate-VII structure of figure 3.22(g) under pressure is shown in figure 3.23. It is compared with the graphite and diamond phase of carbon. Adding pressure stabilizes the geometry against graphite, but not against diamond. In other words, adding low pressures to the system stabilizes diamond more than the clathrate-VII structure. Increasing the pressure further destabilises graphite more than the clathrate-VII structure. Figure 3.23 reveals a minimal formation energy of > 0.4 eV/atom around a pressure of 6 GPa. In this pressure region carbon changes its phase from graphite to diamond. The formation energy level of 0.4 eV correspond to a temperature of 4600 K $> T_{\mathrm{C}}^{\mathrm{melt}}$. Ergo it is unlikely to find the carbon-only type-VII clathrate experimentally at any pressure. If the difference in formation energy or the melting temperature of carbon increases more under pressure has not been further investigated.
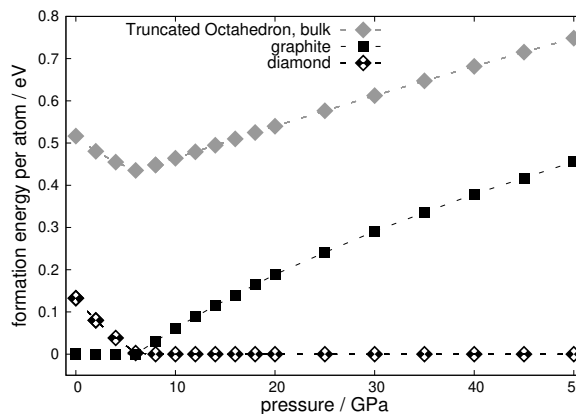
Figure 3.23: Formation energy of bulk carbon phases under pressure.
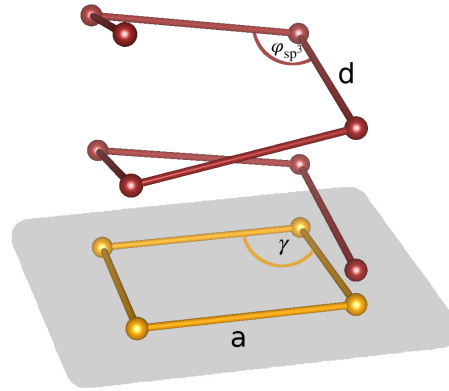
Figure 3.24: Creating spirals. Atoms of the spiral are marked red and are placed equidistantly to their neighbor atoms. The projection of the atoms onto the gray plane is colored in orange. Although the planar angle between the red atoms is equal to φ_{sp^3}, the projection γ can represent a regular polygon. The true inter-atomic distance is d and its projection is labeled a.

3.3.3 Spirals

Facing the issue of creating cage structures periodically in 3D space one can try to go one step back and look for an alternative strategy. At first the strategy is to create quasi-1D structures of sp^3-carbon and to connect them later to 3D-periodic structures to create the hollow areas. As the planar angle of $\varphi_{sp^3} = 109.47°$ does not match the planar angle $\varphi_{polygon}$ of any regular polygon, one can use a different perspective by projecting φ_{sp^3} onto a plane. The atoms can be positioned to create regular polygons within this projection forming the angle γ, while the true angle of the structure remains of the value of φ_{sp^3} (see figure 3.24). Hereby it is easy to see the limit of γ:

$$\gamma \leq \varphi_{sp^3} \tag{3.2}$$

The positions $\mathbf{r}$ of the vertices can be described via cylindrical coordinates. In the simplest case the chained vertices of the spiral follow the same order as in the projected polygon:

$$\mathbf{r}_k\left(n, R, z_0\right) = \begin{pmatrix} R \cos 2\pi\frac{k}{n} \\ R \sin 2\pi\frac{k}{n} \\ z_0 \frac{k}{n} \end{pmatrix} \tag{3.3}$$

n defines the rotational symmetry of the projected spiral and R its radius. z_0 is the shift of the spiral within one period perpendicular to the projection plane and k is the index of the vertices

(a) linear projection   (b) triangular projection   (c) square projection   (d) pentagonal projection
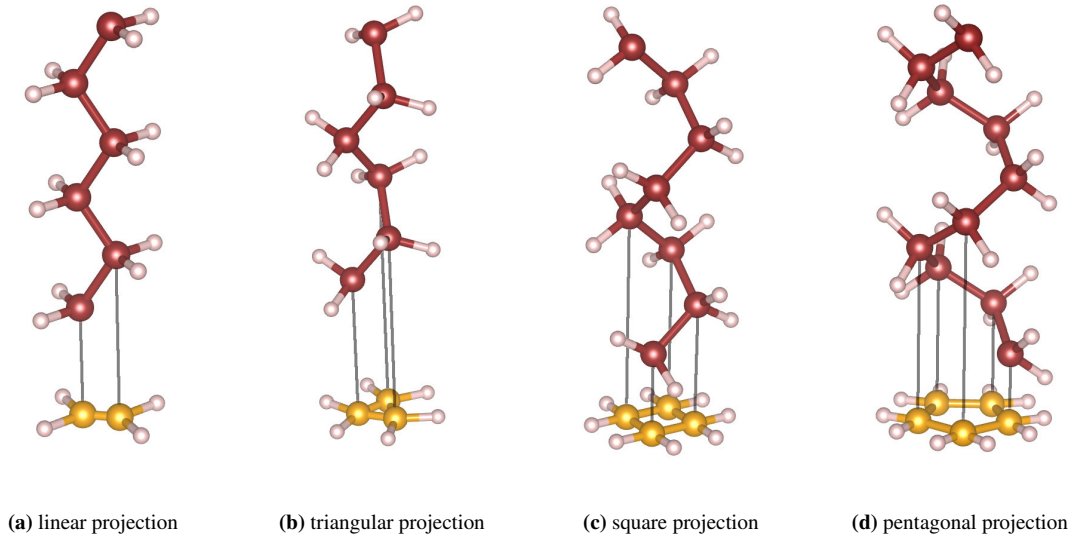
Figure 3.25: Carbon spiral structures. Carbon atoms of the spiral are marked red, their projection is colored yellow. Passivating hydrogen atoms are shown in white.

on the spiral. More in detail, R and z_0 are not constants, but functions of the C-C distance d and the symmetry parameter n. Moreover, a is the projection of d onto the plane:

$$z_0(n) = n\,d\,\sqrt{1 - \left(\frac{a(n)}{d}\right)^2}$$

$$a(n) = d\,\sqrt{\frac{1 + \cos\varphi_{sp^3}}{1 - \cos\frac{2\pi}{n}}} \tag{3.4}$$

$$R(n) = \frac{d}{1 - \cos\frac{2\pi}{n}}\,\sqrt{\frac{1}{2}\left(1 + \cos\varphi_{sp^3}\right)}$$

As the true planar angle within the spiral is set by φ_{sp^3} and the regular hexagon ($120°$) has a larger angle than φ_{sp^3} the possible projections are limited to $-$, $\triangle$, $\square$ and $\varhexagon$. The corresponding spirals are sketched in figure 3.25.

Further degrees of freedom can be unlocked by separating the order of the vertices on the spiral against the order within the projection. Furthermore, there is the possibility to break the symmetry between arbitrary two neighboring vertices within the spiral. The constant z-shift between the two neighboring atoms of each atom of the spiral is changed to two alternately applied z-shift values. Further details how to construct these spirals are available in section A.4 of the appendix. Here this extended strategy should not be pursuit in the following as decoupling the order of the vertices between spiral and projection reduces the space inside the spiral and changing to a pair of z-shifts makes it harder to link the final structure properly in further dimensions.

The possibilities of the basic case of equation (3.3) are shown in figure 3.25. Here, hydrogen is added to the carbon atoms to passivate the structures and to highlight the region, where further carbon atoms can be linked. As the C-C distance within the spiral is the same for all cases, the length of projected edges is the longest at the pentagonal structure of figure 3.25(d). Its projected area is the largest. Nevertheless, a plane cannot be tiled using only regular pentagons. Therefore it is impossible to form an appropriate crystal by only arranging these pentagonal spirals around each other in a parallel way. Tilting some might work.

Regarding the zig-zag structure of figure 3.25(a) and the square structure of figure 3.25(c), it is interesting to see how its extension to further dimensions, while removing hydrogen atoms, creates a 3D-crystal structure: diamond. Extending the square spiral of figure 3.25(c) by itself in the other two dimensions, while removing the hydrogen atoms, leads to the structure of diamond as well.

Unfortunately this approach to tile 3D-space with carbon atoms and their sp^3-orbitals, directly leads to the structure of diamond and sadly not to new geometries offering more vacant space.

3.4 Lithium-doped, boron-substituted carbon clathrates

Zeng *et al.* [40] introduce a different approach for carbon-based clathrate structures. The focus is shifted from dopable clathrate structures made solely of carbon to lithium-doped carbon clathrates with boron-substitutions.

In section 3.1 and 3.2.4 helium is used as an endohedral filler because spatially it is the smallest atom available in the periodic system of elements. Zeng *et al.* change the perspective regarding possible dopants from atoms to ions. The lithium ion Li^+, spatially speaking, is even smaller than a helium atom. Both only contain $1 s^2$-electrons, but the core of lithium has a higher charge than helium ($+3$ e vs. $+2$ e), dragging the two electrons closer to the core. An isolated proton H^+ would use even less space, but lithium is favored as a dopant as its $2 s^1$ valence electron is significantly less bound to the core than the $1 s^1$ electron of a hydrogen atom. The first ionization energies of some elements are listed in table 3.8 showing $E^{ion}(H) = 2.5 \, E^{ion}(Li)$. Boron is used by Zeng *et al.* to substitute single carbon atoms to compensate for the 'additional' electron coming from lithium atoms which have become ionized. The boron atoms dope the carbon framework structure with holes. Zeng *et al.* proposed clathrate structures at a pressure of 40 GPa. They are depicted in figure 3.26 to highlight the different kinds of polyhedra.

In the current section, the stability of the proposed structures is investigated under pressures ranging from 0 to 50 GPa. Their formation energy was calculated according to equation (2.20) on page 14. The highest pressure has been chosen to enable references to the global structure prediction runs of section 3.1 and to show a small trend for the proposed structures toward pressures higher than in [40]. The reference structures of the individual elements carbon, lithium and boron have been created for all pressures in two ways:

- Reference structures for 0 GPa were taken from the Materials Project database [75] and stepwise relaxed to higher pressures.

- Some short global structure prediction runs were initiated for lithium, boron and carbon at a pressure of 40 GPa, the pressure applied by Zeng *et al.* After the refinement at this pressure, the most stable structures have been stepwise relaxed at the next pressure level.

The formation energies of the proposed structures are compared in figure 3.27(a). The image reveals their distinct ordering of stability. The most stable structure has the composition

Table 3.8: **Ionization energies of chemical elements [139].**

			E^{ion} / eV	E^{ion} / $E^{ion}(Li)$
H	$\rightarrow$	H^+	13.6	2.5
Li	$\rightarrow$	Li^+	5.4	1
Be	$\rightarrow$	Be^+	9.3	1.7
Be^+	$\rightarrow$	Be^{2+}	18.2	3.4
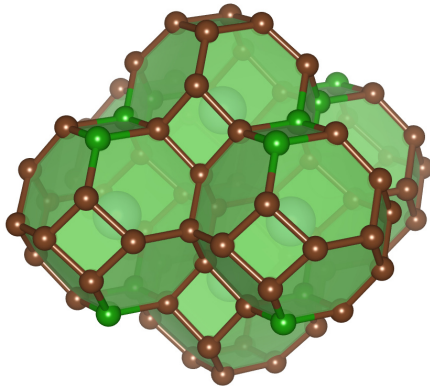
(a) LiBC$_5$. clathrate type-VII / arrangement of truncated
octahedra ◆
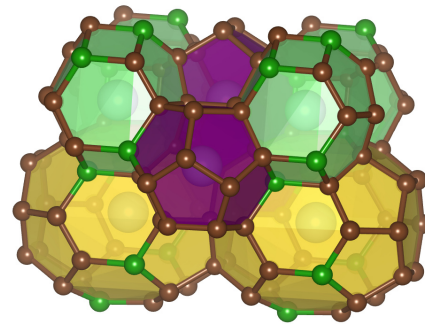
(b) Li$_3$B$_3$C$_{14}$
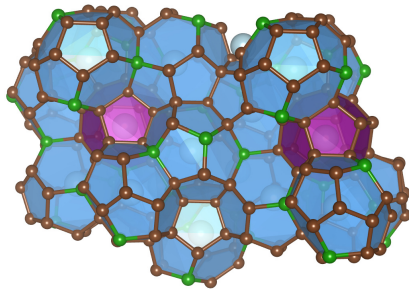
(c) Li$_4$B$_4$C$_{19}$. clathrate type-I
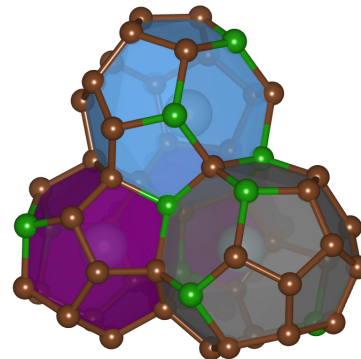
(d) Li$_7$B$_7$C$_{33}$. The whole crystal is built as a combina-
tion of this arrangement of the three polyhedra.

Figure 3.26: Zeng *et al.* [40] proposed four Li-BC-clathrate structures with different compositions at a pressure
of 40 GPa. The structures were replotted to increase the visibility of the present polyhedra. In this
context dodecahedra ⬠ are marked purple, truncated octahedra ◆ green, tetradecahedra / hexagonal
truncated trapezohedron ⬟ blue, pentakaidecahedra gray and barrel shaped polyhedra yellow.
Carbon atoms are brown, boron is green and lithium atoms are blue inside the cages. The label of
the individual figures refers to the content of the unit cell.

(a) Formation energy of the clathrates structures proposed by [40] under different pressures.

(b) Comparison of the formation energies of the 'best' proposed structure, without boron and without lithium.
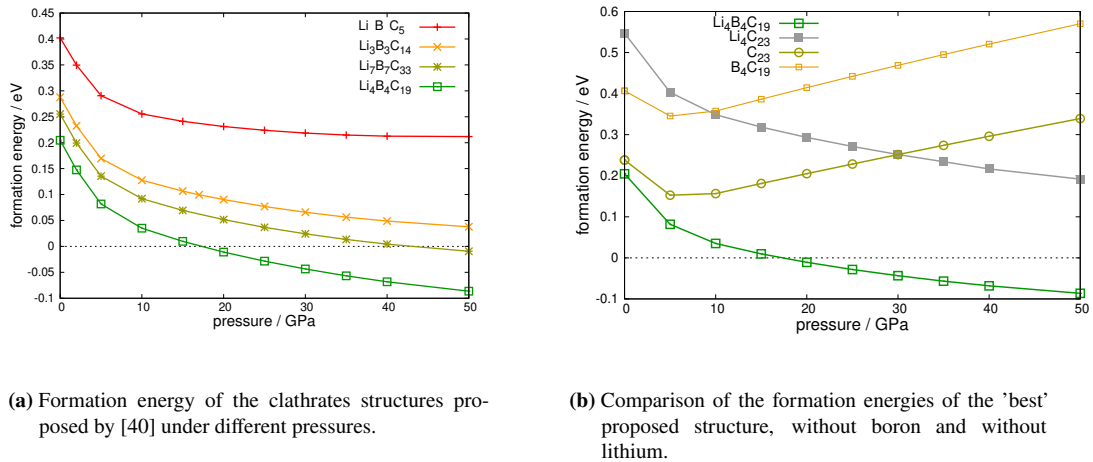
Figure 3.27: Formation energies of the clathrates structures of figure 3.26 at different pressures.

$Li_4B_4C_{19}$. The least stable structure has the composition $LiBC_5$. Furthermore, the crystal of $Li_4B_4C_{19}$ has negative formation energies at pressures above 20 GPa. The next most stable proposed structure is $Li_7B_7C_{33}$ and shows a similar behavior, starting around 40 GPa. The possibility of these two structures to be thermodynamic stable is discussed later around page 62. As the lithium content of the structures hardly varies (see table 3.9), it is not the main reason to explain this stability ordering. The difference in stability is a result of the different structural geometries.

The stabilizing effect of the lithium-boron-strategy is investigated in figure 3.27(b). There, the green curve —□— again represents the most stable proposed structure. The other curves are variations of this structure with either lithium (—■—), only the boron substitutions (—□—) or non of both (—○—). Comparing the —□— and —■— curves, the formation energy of these two lithium-doped structures reveals the importance of the boron atoms. They reduce the formation energy by around 0.3 eV/atom. Under pressure the formation energy of both structures decreases monotonically. In contrast, the formation energies of both lithium-free structures —○— , —□— have a local minimum around a pressure of 5 GPa. This pressure region has already been mentioned to be the coexistence region of graphite and diamond at temperatures of 0 K. At high pressures, the formation energies of these two structures increase as well as their energetic difference. Graph —○— has a lower formation energy than —□— . This is understandable as the first is the carbon-only structure and the last one represents the carbon structure with boron substitutions. It is p-doped, but there are no further electrons to catch. The different tendency of the formation energy of these two groups leads to two further statements:

- Comparing the green —□— with the dark yellow curve —○— , their formation energies are similar at pressures of 0 GPa and increase under pressure.

- The gray curve —■— has a similar formation energy as the orange one —□— at 10 GPa. At pressures of 30 GPa and above the lithium doping reduces the formation energy against the carbon-only framework —○— .

Table 3.9: Overview on the percentage of each element for each composition.

	Li	B	C
LiBC$_5$	0.143	0.143	0.714
Li$_3$B$_3$C$_{14}$	0.15	0.15	0.7
Li$_4$B$_4$C$_{19}$	0.148	0.148	0.704
Li$_4$C$_{23}$	0.148	0	0.852
Li$_7$B$_7$C$_{33}$	0.149	0.149	0.702
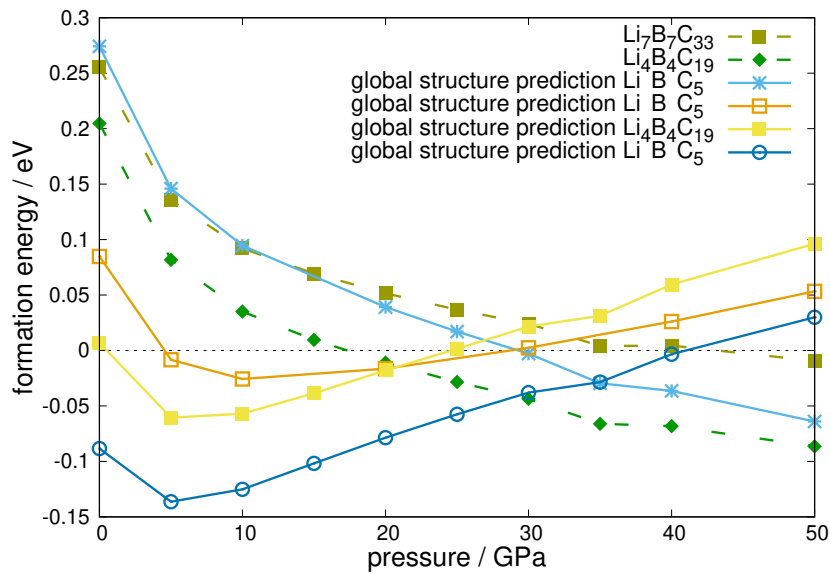
Figure 3.28: Comparison of the formation energies of structures under pressure. The most stable structures from figure 3.27(a) are compared with the most stable structures from further global structure prediction calculations. The structures of the solid lines are sketched in figure 3.29.

(a) LiBC$_5$ —o—

(b) Li$_4$B$_4$C$_{19}$ —■—

(c) LiBC$_5$ —□—

(d) LiBC$_5$ —✱—
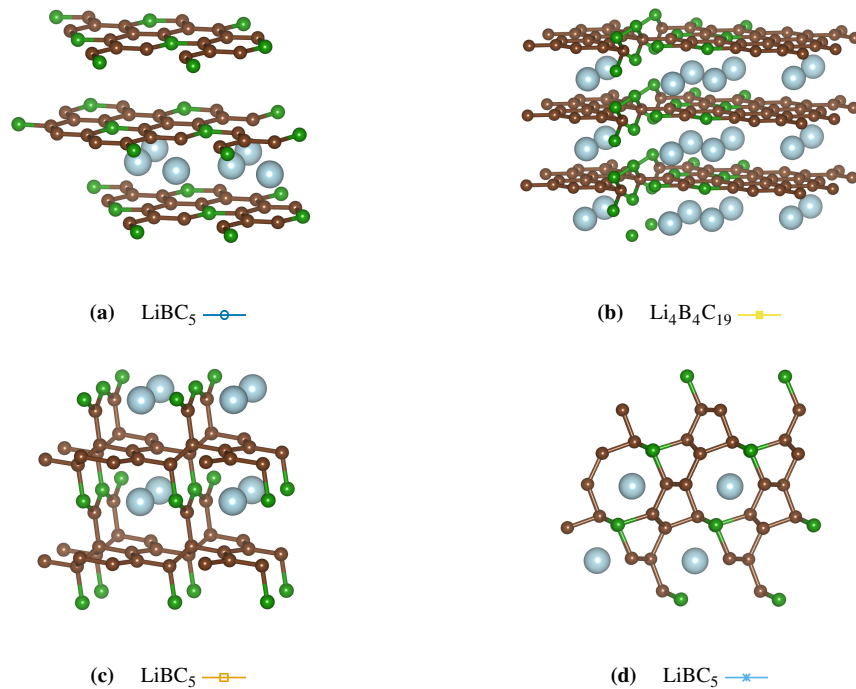
Figure 3.29: Structures of the solid lines of figure 3.28 found with global structure prediction search. Carbon atoms are brown, boron is green and lithium atoms are bright blue.

Further comparison of the proposed structures with global structure prediction runs

Besides calculating the formation energy in figure 3.27(a), we performed global structure prediction calculations with the same composition of chemical elements. The resulting formation energies are shown in figure 3.28 with solid lines. Dashed lines relate to the two most stable clathrate structures already shown in figure 3.27(a).

Comparing the formation energies at pressures below 30 GPa reveals, the new structures are more stable than the proposed clathrates. In contrast to them, they are not clathrates and contain no cages for lithium (see figure 3.29). It is also recognizable, the new structures at pressures below 20 GPa are more stable the closer their structure is to a layered geometry. The formation energies of the structures of figures 3.29(a) and 3.29(b) show a local minimum at pressures around 5 GPa. It originates from the phase transition of carbon between graphite and diamond. The local minimum of the structure of figure 3.29(c) is broader and shifted toward 10 GPa. This is not a surprise, as the same number of carbon atoms have three or four neighbors, enforcing sp^2 and sp^3 orbitals respectively. Within the region of 20 and 35 GPa, the stability ordering of the discussed structures changes dramatically. At higher pressures cages and channels are favored over layered structures.
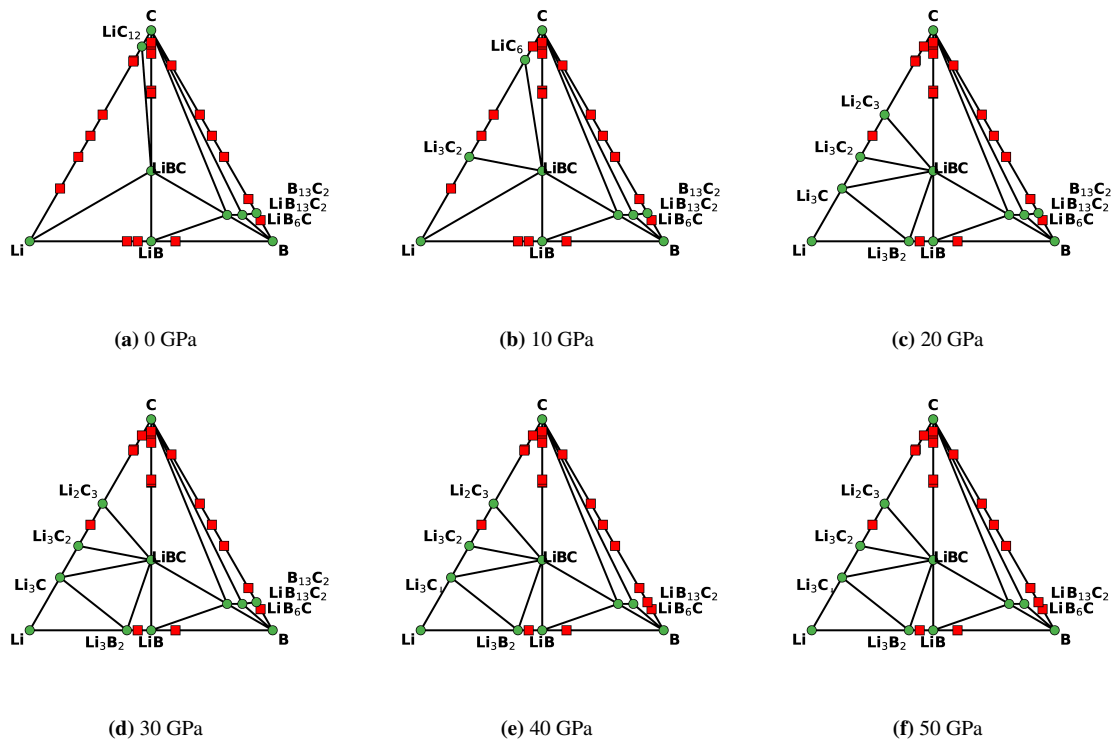
Figure 3.30: **The ternary phase diagrams** of the mixture of lithium, boron and carbon are plotted at different pressures. The structures are arranged in a triangle to represent the composition of each unit cell. Accordingly, each corner represents one of the three concerned elements. The most stable structures are marked green and shape the convex hull, which is sketched by the lines. Structures with a formation energy above the hull are marked red. For each composition and each pressure, only the candidate with the lowest enthalpy / the most stable structure is shown. This candidate of each composition can change between the different diagrams as a structural phase change occurs.

Ternary phase diagrams

To set the structures of figure 3.27 and 3.28 further into perspective, ternary phase diagrams need to be calculated at each pressure to allow comparisons with respect to the convex hull. These phase diagrams are plotted in figure 3.30 for pressures from 0 to 50 GPa. The reference structures were identified again by global structure prediction runs performed at 0 and 40 GPa. The most stable structures have been relaxed at further pressures. Clathrate structures of the global structure prediction approach of section 3.1 have been modified with lithium and boron and added as well.

In figure 3.30, structures forming the convex hull are marked green and thermodynamic unstable structures are plotted red. As the clathrate structures proposed by Zeng *et al.* [40] all contain the same amount of lithium and boron atoms, the important region of the phase diagrams is the central, vertical line connecting C with LiB. There, the only thermodynamic stable structures have the composition C, LiBC or LiB. Furthermore, none of the proposed configurations is highlighted green at pressures up to 50 GPa. Ergo they are not thermodynamic stable. Although the most stable clathrates of figure 3.28 (——□——, $Li_4B_4C_{19}$) has a negative formation

(a) **LiBC** [152–155]
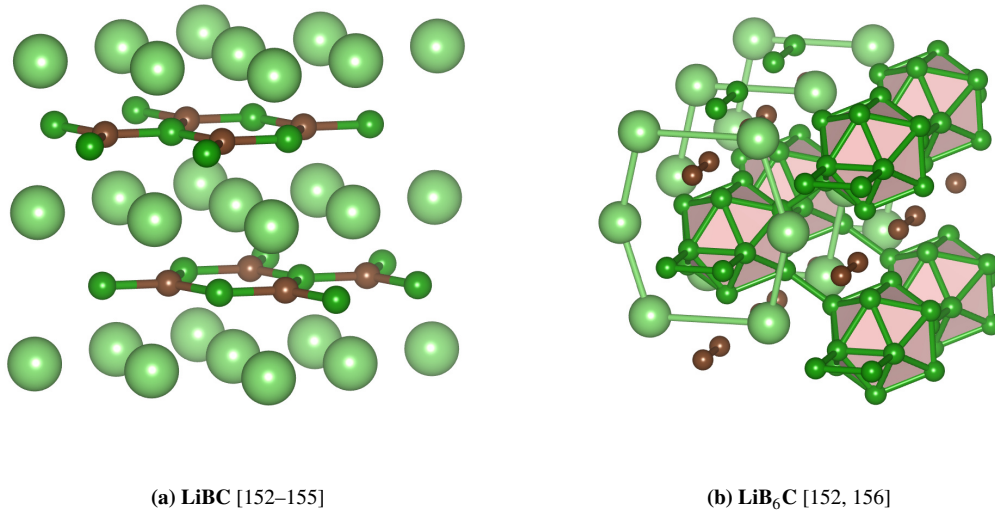
Figure 3.31: The most stable structure of LiBC and LiB$_6$C at pressures between 0 and 50 GPa.

energy at pressures between 20 GPa and 50 GPa, its distance to the convex hull is still around 270 meV/atom in this pressure region. The next most stable clathrate structure (—○—, Li$_7$B$_7$C$_{33}$) shows a distance to the convex hull of around 340 meV/atom at pressures between 10 GPa and 50 GPa. Both energy distances correspond to temperatures above 3000 K. Consequently these structures do not represent the most stable configuration, although the formation energy is negative.

In figure 3.30 some compositions contain all three elements and are always marked thermo-dynamic stable (green). Their structures are shown in figure 3.31 (LiBC and LiB$_6$C) and figure 3.32 (LiB$_{13}$C$_2$). Both structures of figure 3.31 were taken from the Materials Project database [75]. Each structure represents the most stable configuration of its composition at zero pressure. In the pressure regime up to 50 GPa, no more stable structure could be identified. The structure of LiBC (figure 3.31(a)) was also reproduced by global structure prediction runs. It is segmented into layers of lithium triangles and boron-carbon hexagons. The lithium atoms are placed on top of the center of the boron-carbon hexagons. Furthermore, these hexagonal layers alternate between placing carbon and boron atoms at the equivalent position.
In comparison, the excess of boron in LiB$_6$C-structures leads to the formation of rods of boron icosahedra (figure 3.31(b)). Within the rods, the icosahedra are linked directly by two pairs of atoms. Carbon atoms appear in pairs and on a longer range, lithium is arranged in hexagons with edges of 2.9 Å and 3.7 Å. The distance between the planes of the hexagons is 4.7 Å

Regarding the composition LiB$_{13}$C$_2$, two similar structures are know with the same formation energy at zero pressure (see figure 3.32(b)). Under pressure, the formation energy of both structures changes similarly too (figure 3.32(a)). Furthermore, this plot reveals a structural phase change at pressures of 5 GPa. The two identified, most stable structures under pressure are shown in figure 3.32(c) and (d). Comparing these structures, in all four cases boron arranges in the form of icosahedra again.

(a) formation energy

(b) $LiB_{13}C_2$ mp-655591 [152, 156]

(c) $LiB_{13}C_2$ new 1

(d) $LiB_{13}C_2$ new 2
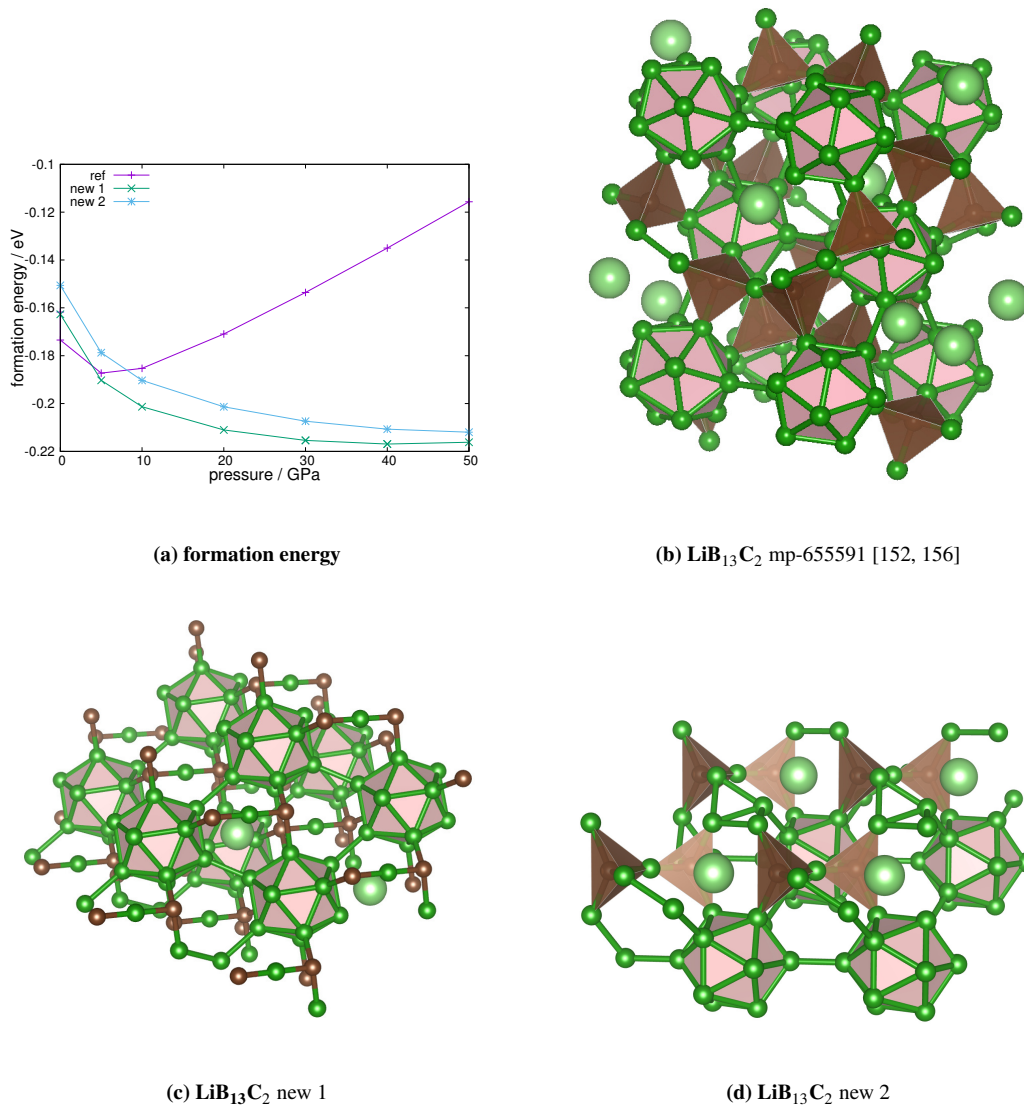
Figure 3.32: The structure of the most stable geometry of $LiB_{13}C_2$ changes at pressure of ≈ 5 GPa. Panel (a) compares the formation energies of the structures shown in (b) - (d) under pressure. (b) has the lowest formation energy at zero pressure. (c) and (d) are the two most stable structures identified under high pressure.

3.5 Summary

Several attempts to search for stable carbon clathrate crystals were presented. The first approach used place holder atoms to create vacancies in global structure prediction calculations (section 3.1). Helium-filled clathrates structures were identified which are significantly more stable than the carbon analog to a silicon type-I clathrate. The most stable of them is still 225 $^{meV}/_{atom}$ less stable than diamond. From the presented point of view, the formation of carbon clathrate structures cannot be seen as impossible. Adding thermal energy and external pressure to the system could further reduce the energetic distance.

Taking a geometric approach reveals, the topic can be separated in three different aspects, which cannot be treated completely isolated from each other (section 3.2 and 3.3):

- stability of the cage geometry

- stability of the structure linking the cages

- cage size and size of candidate atoms to fill the cage

The possibility of filling the vacancy of the clathrate structure has been discussed as well. However, the comparison with silicon and germanium highlighted the spatial limitations of carbon-based structures. Readjusting the point of view to ion dopants in section 3.4, it was shown that boron-substitutions can stabilize lithium-doped carbon clathrate structures. At pressures above 20 GPa, clathrate structures with a negative formation energy were identified. However, their distance to the convex hull of 270 $^{meV}/_{atom}$ is still significant. Adding more pressure to the system hardly changes this distance.

It is unlikely, this approach via lithium and boron can be expanded to further combinations of chemical elements. Ionized beryllium Be^{2+} or hydrogen H^+ would even be smaller than Li^+ and the second electron of beryllium can be compensated by another substitution of carbon to boron. But neither of this is useful, as beryllium and hydrogen show a first ionization energy significantly larger than lithium. Furthermore, after the first ionization, the remaining valence electron of beryllium is bound even tighter to the core than the former.

Chapter 4

Binary compounds of the elements Al, La, Sr, Ti, O

Motivated by quasi-crystals found by Förster *et al.* on a platinum surface [157], in future projects, the possibility to form quasi-crystals of further combinations of the elements aluminum, lanthanum, strontium, titanium and oxygen should be investigated. In contrast to crystal structures, quasi-crystals only offer short-range ordering and no long-range periodicity. Correspondingly a large quasi-crystal can not be simulated using a small number of atoms with periodic boundary conditions. Large simulation cells are required to perform reasonable global structure prediction calculations for quasi-crystals. To perform them in a reasonable amount of time, DFT cannot be used, as it scales $\mathcal{O}(N_{\mathrm{el}}^3)$ with the number of electrons N_{el}. To increase the speed of the search to find candidates worth being refined with DFT calculations, the minima hopping method can be coupled with DFTB+ [62] or neural networks [158] instead of VASP (DFT) to approximate the enthalpy and forces of a structure. However, this path needs to be prepared first: Regarding DFTB+, the corresponding pairwise interactions need to be parameterized. If machine learning code should be used instead of DFTB+, training is still needed.

The aim of this chapter is therefore to create a large number of binary compounds of the corresponding elements via global structure prediction calculations and DFT.

As a balance between structural variety and speed, general simulation cells of the minima hopping runs contain up to 10 atoms. As training sets should be created, the goal is not solely to look for thermodynamic stable structures. To increase the variety of the training set structures should also be taken into account which are higher in energy. Therefore not only candidates for local minima, but also the structures from the molecular dynamic steps are used. Furthermore, the result is compared with the materials project database [75] to add further known structures and compositions to the training sets.

As outlined in section 2.5, the search proceeds in two main steps to reduce calculation time:

1. Structures are created by the minima hopping method.

2. Structures are refined.

No external pressure is applied to any system.

To structure the discussion of the $\binom{5}{2} = 10$ binary phase diagrams, the four containing aluminum are discussed in section 4.1. The three phase diagrams representing binaries of oxygen, but no aluminum are discussed in section 4.2. The remaining binary structures of lanthanum, strontium and titanium are discussed in section 4.3. In each binary phase diagram, the convex hull is sketched two times in different colors. The results of the global structure prediction calculations are presented in black •. This list of structures is complemented by low-enthalpic structures of the Materials Project database, shown in green •. The energies have been calculated with VASP, using the PBE exchange-correlation energy functional [49–54]. The cutoff energy is always 520 eV and no further energy corrections have been applied.

4.1 Binary phases of aluminum

The binary phase diagrams containing aluminum are shown in figure 4.1. In each case, the black and the green reference convex hull match each other well. This indicates many low-energetic structures were identified. If the lower curve is marked green, the known ground-state structure of this composition has not been identified by the global structure prediction calculations. In each case of figure 4.1, at least one stable phase could be identified, which combines aluminum with another element. Each binary phase diagram is combined with a normalized histogram of the energetic distribution of the identified structures. To limit the number of compositions shown in each histogram, different compositions are combined within each graph. One graph represents the composition containing the lowest formation energy. Starting from this composition, in the other two graphs the presence of one of the elements in the unit cell is increased.

Only structures with a formation energy of up to 1 eV are shown. As this energy translates to a temperature of above 10^4 K, structures above are definitely in a region where predicting bulk structures doe not make sense. As the lowest formation energy varies from binary to binary, the shown energetic bandwidth varies significantly. It varies from 4 eV of aluminium and oxygen to 1.5 eV and below for the other binaries.
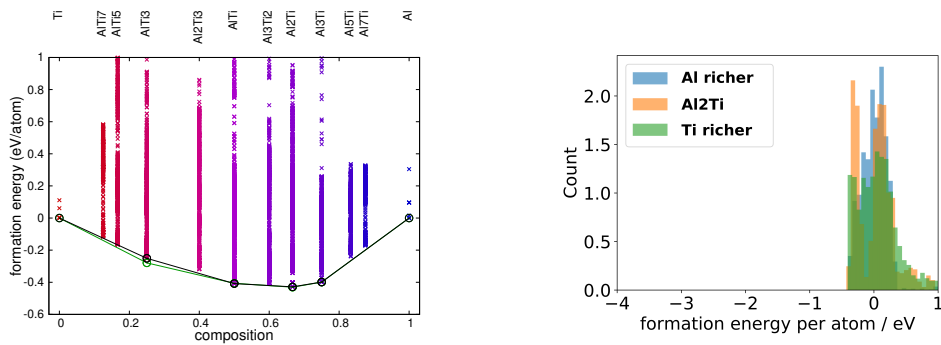
(a) Titanium & aluminum - Besides the pure elements, the convex hull is spanned by the compositions of AlTi, AlTi$_3$, Al$_2$Ti and Al$_3$Ti.
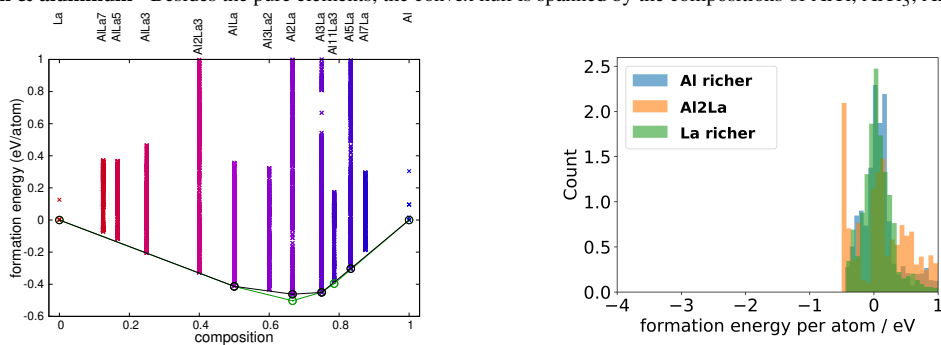
(b) Lanthanum & aluminum - Besides the pure elements, the convex hull is spanned by the compositions of AlLa, Al$_2$La, Al$_3$La, and Al$_{11}$La$_3$.
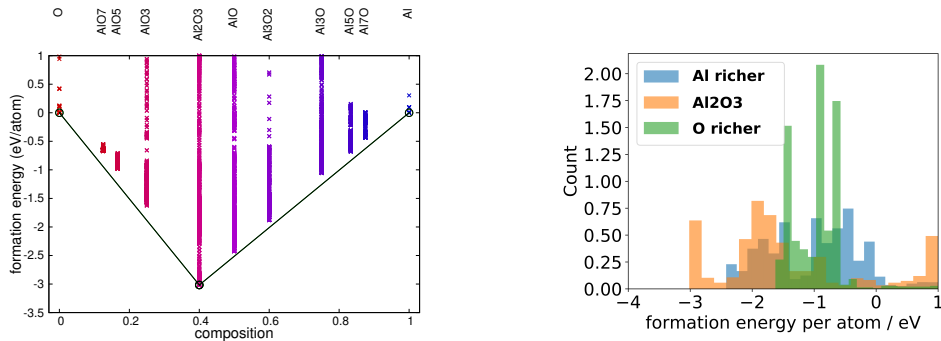
(c) Oxygen & aluminum - Besides the pure elements, the convex hull is spanned by the compositions of Al$_2$O$_3$.
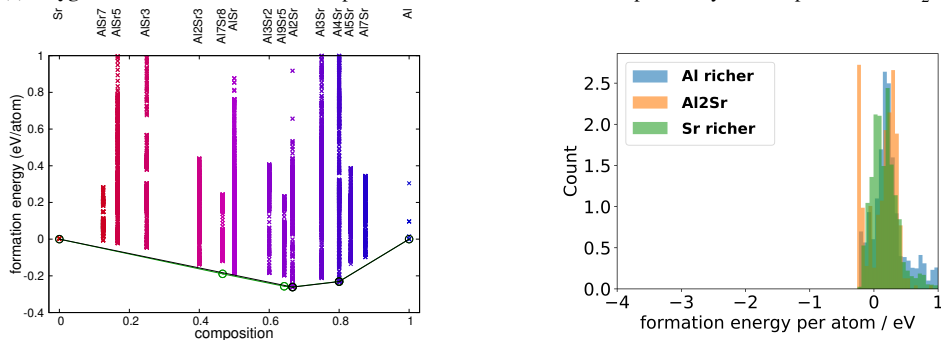
(d) Strontium & aluminum - Besides the pure elements, the convex hull is spanned by the compositions of AlSr$_2$, Al$_4$Sr, Al$_7$Sr$_8$ and Al$_9$Sr$_5$.

Figure 4.1: Binary phase diagrams containing aluminum. On the left side, the phase diagram for the combination (a) - (d) is shown. On the right, the histogram is plotted. It visualized the distribution of identified structures up to a formation energy of 1 eV. There, the structures are only differentiated with respect to which of the two elements has more atoms in the unit cell. The histograms are normalized to span the same area.

4.2 Oxides

The binary phase diagrams of oxygen are shown in figure 4.1(c) and 4.2. The convex hull of the lanthanum oxide and strontium oxide structures roughly matches the reference of the materials project database [75]. In contrast to previous cases, the self-produced convex hull partially seems to improve on the reference hull. The corresponding structures are discussed in the following sections. The histograms show a broad energetic range, which is always above 3 eV. Furthermore, it is interesting to see that all these histograms show at least two distribution maxima. Regarding a single composition this could hint to the origin of the structure: local minimization or molecular dynamics step to escape a local minimum. However, one would expect such local extrema to be smeared out when combining different compositions in one histogram. But the extrema can still be seen. This most probably originates from the different energetic bandwidth of the oxides.
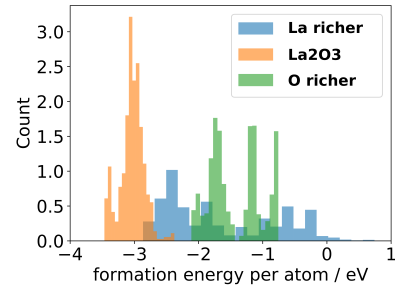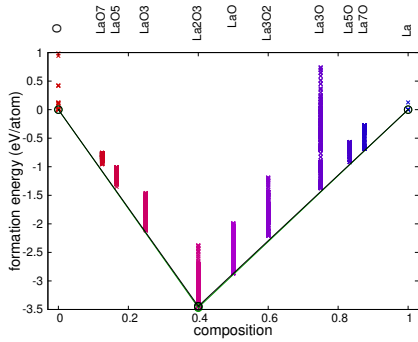
(a) Oxygen & lanthanum - Besides the pure elements, the convex hull is spanned by the composition of La$_2$O$_3$.
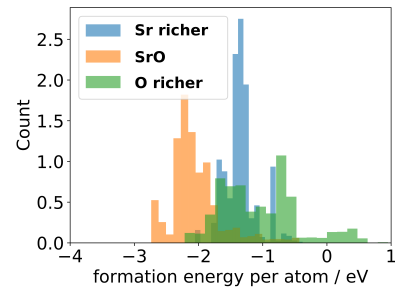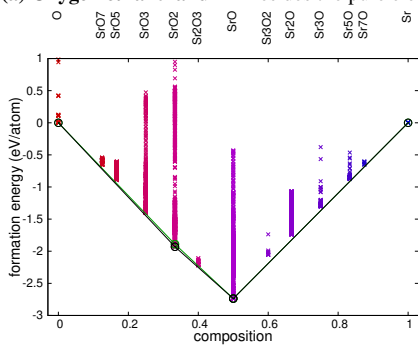
(b) Oxygen & strontium - Besides the pure elements, the convex hull is spanned by the compositions of SrO and SrO$_2$.
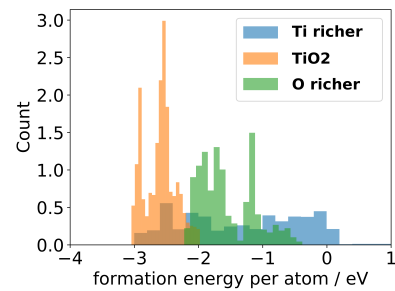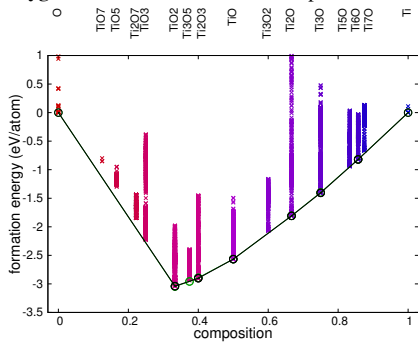
(c) Oxygen & titanium - Besides the pure elements, the convex hull is spanned by the compositions of TiO, TiO$_2$, Ti$_2$O, Ti$_2$O$_3$, Ti$_3$O, Ti$_3$O$_5$ and Ti$_6$O.

Figure 4.2: Further binary phase diagrams containing oxygen and the corresponding histograms.

(a) my candidate   **(b)** MP mp-458 [152, 159–168]   **(c)** MP mp-1046793 [75, 152]
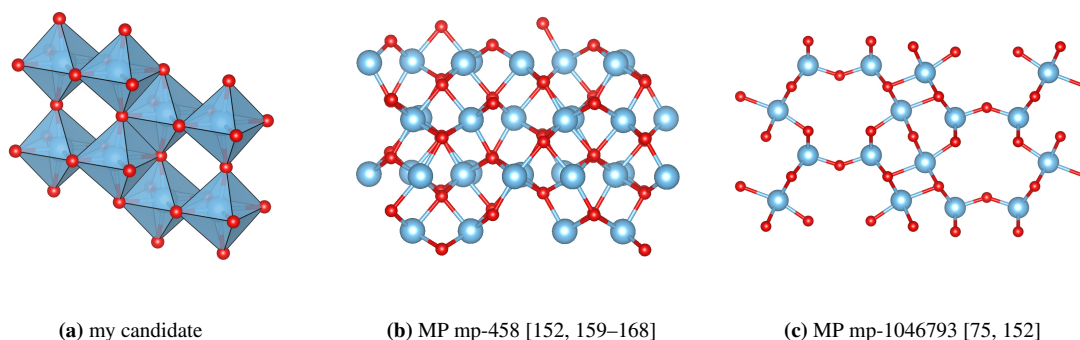
Figure 4.3: Comparison of low-enthalpic Ti$_2$O$_3$ structures.

4.2.1 Ti$_2$O$_3$

The structure of the most stable phases using a Ti$_2$O$_3$ stoichiometry are sketched in figure 4.3. Figure 4.2(c) reveals an energetic advantage of around 10 $^{meV}/_{atom}$ (120 K) of the structure shown in figure 4.3(a) against mp-458 of the materials project database (figure 4.3(b)). However, the structure of figure 4.3(a) is more similar to figure 4.3(c). Both show the same planes of titanium and oxygen, but they are arranged differently.

To check if this energetic difference is only an artifact of the used PBE exchange-correlation functional [49, 50], the enthalpies are recalculated using a local-density approximation (LDA) and the Perdew-Wang functional PW91 [150, 151]. PW91 again is based on the generalized gradient approximation (GGA) like the PBE-functional, which has been derived from PW91. The energetic differences are compared in figure 4.4.
Comparing the different functional approximations, the energetic differences between the new structures varies. Nevertheless the energetic ordering stays the same. The new structure of figure 4.3 always show a lower formation energy than the two references.
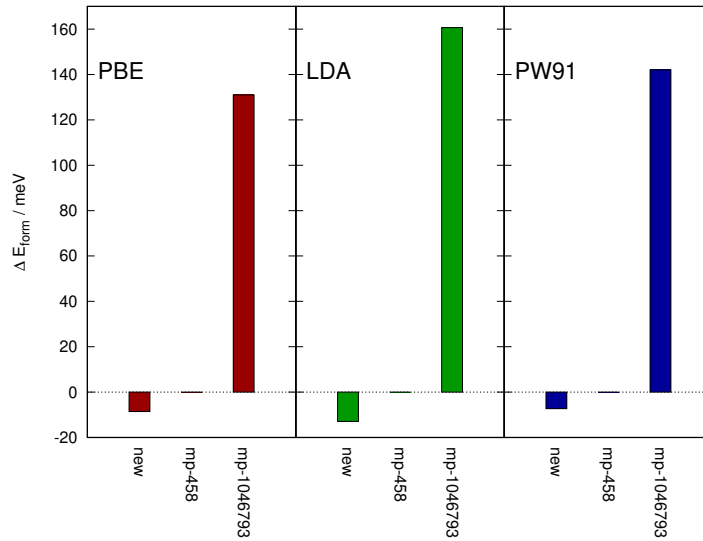
Figure 4.4: Comparison of the energy ordering of a set of structures between different exchange-correlation-energy functionals.

4.2.2 Ti_3O

The structure of the most stable phases using a Ti_3O_1 stoichiometry is sketched in figure 4.5. It reveals an energetic advantage of around 10 $meV/atom$ against the reference, which translates to a temperature of approx. 120 K. Our new structure can be separated into titanium octahedra with oxygen an atom at their center. In figure 4.5(a), the octahedra form slabs like in mp-2591 and mp-557812. In mp-554032 the octahedra form rods.

To verify this energetic difference is not an artifact of the used PBE-functional, again the energies are recalculated using a local-density approximation (LDA) and the Perdew-Wang functional PW91. The energetic differences are compared in figure 4.6.
Despite the energetic ordering of the two reference structures changes between the three approximations of the exchange-correlation functional, the new structures of figure 4.5 always show a lower formation energy then the reference.

4.2.3 SrO_2

The structure of the most stable phases using a Sr_1O_2 stoichiometry are sketched in figure 4.7. It reveals an energetic advantage of around 40 $meV/atom$ against the reference, which translates to a temperature of 460 K.

(a) new

(b) MP mp-2591 [152, 169]

(c) MP mp-557812 [152, 170]

(d) MP mp-554032 [152, 171]
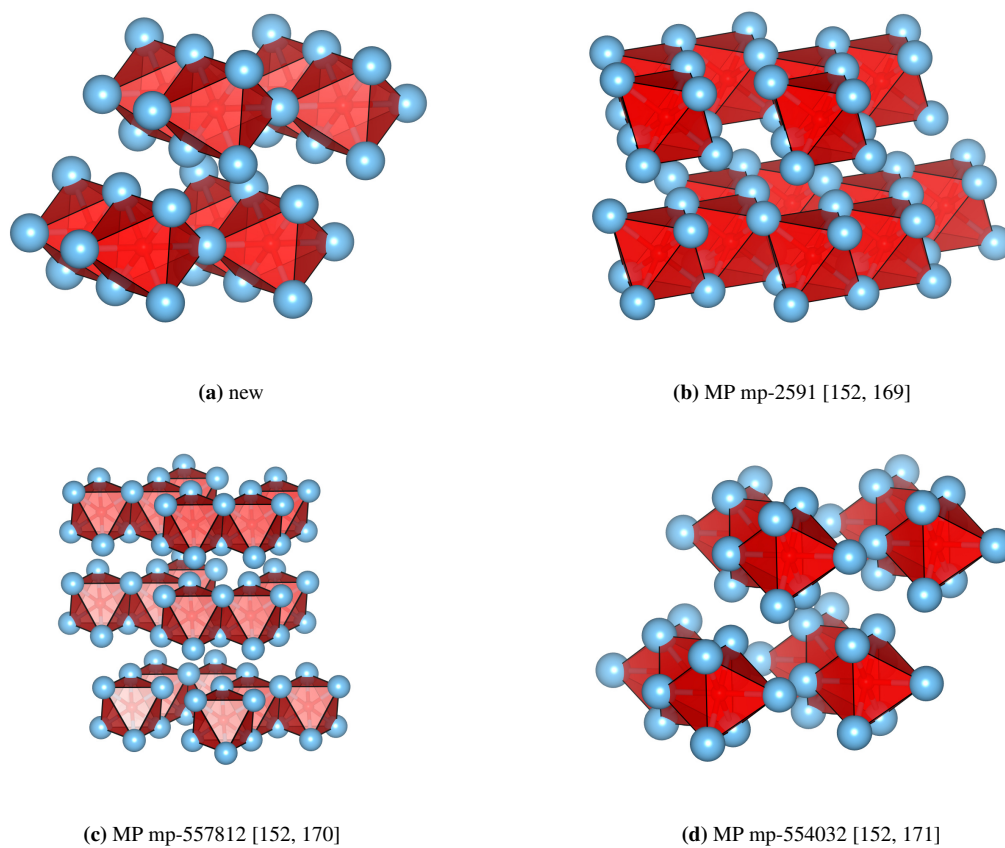
Figure 4.5: Comparison of low-enthalpic Ti_3O_1 structures.
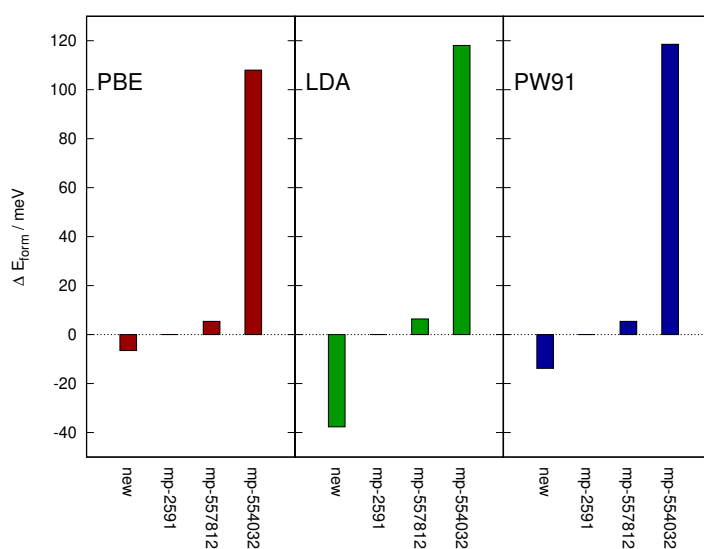
Figure 4.6: Comparison of the energy ordering of a set of structures between different exchange-correlation-energy functionals.

(a) my candidate

(b) MP mp-2697 [152, 172]

(c) MP mp-1179089 [152, 173]
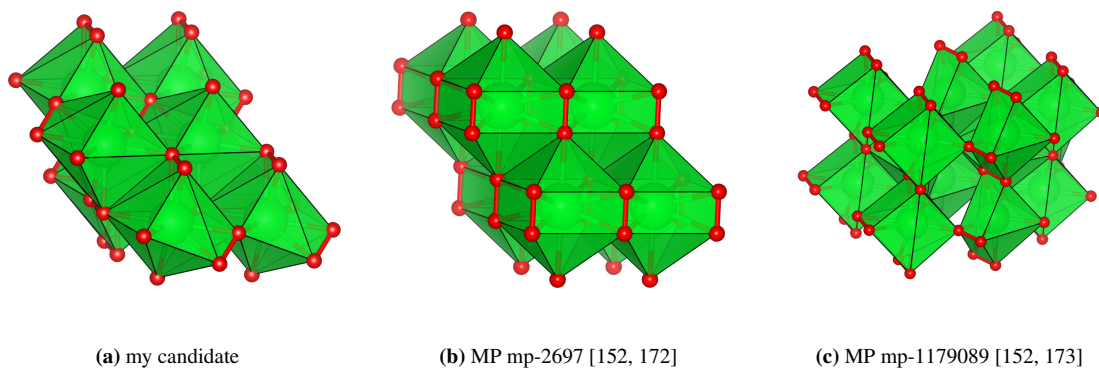
Figure 4.7: Comparison of low-enthalpic Sr$_1$O$_2$ structures.
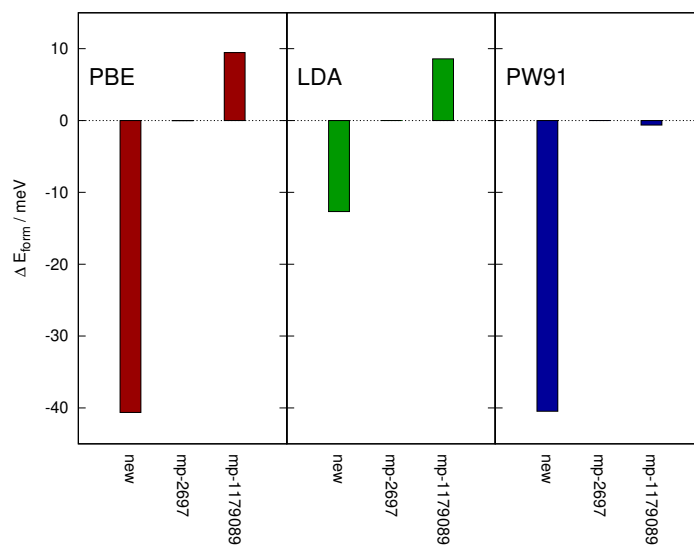
Figure 4.8: Comparison of the energy ordering of a set of structures between different exchange-correlation-energy functionals.

(a) binary phase diagram at 0 GPa

(b) binary phase diagram at 100 GPa

(c) stabilization under pressure
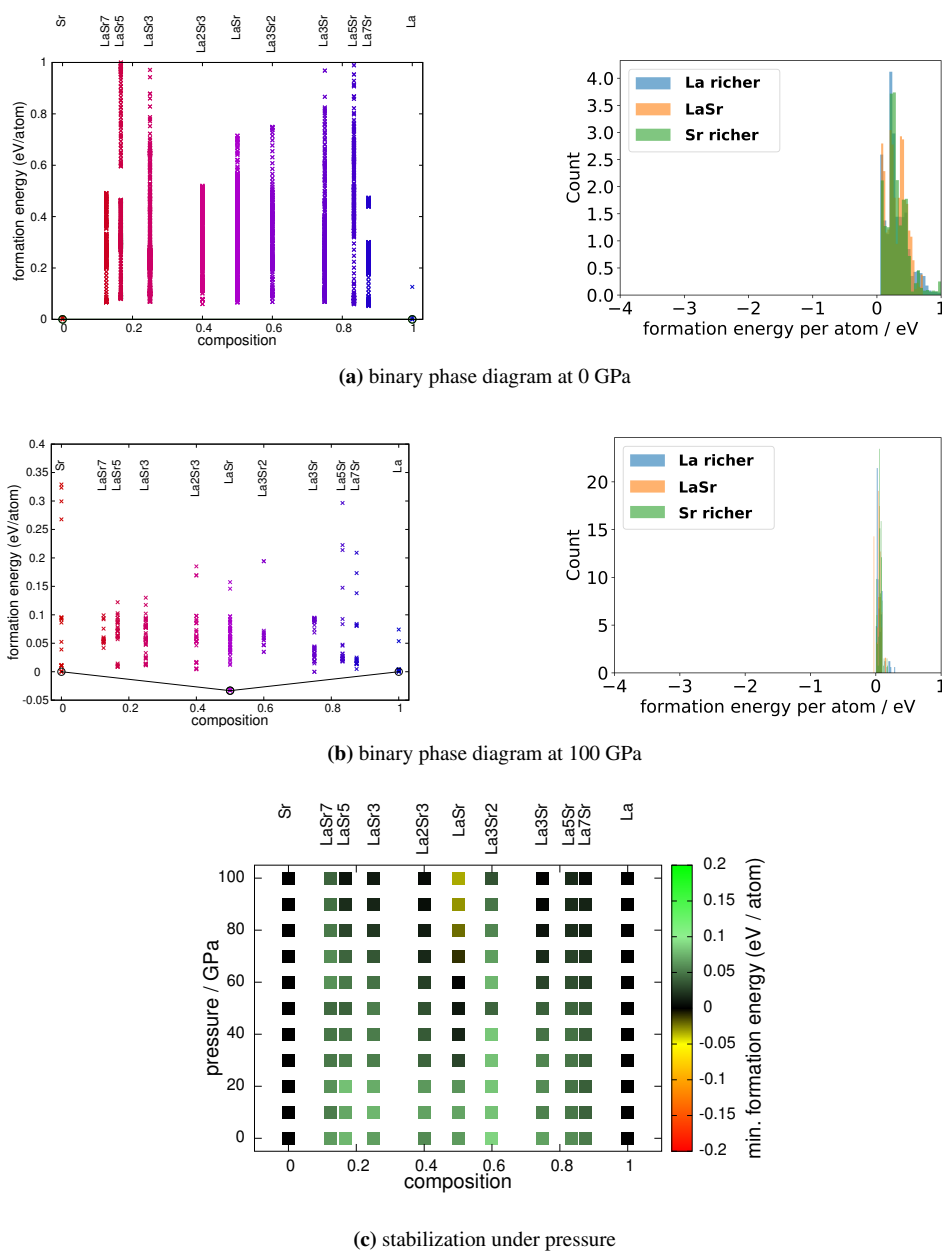
Figure 4.9: Binary materials of lanthanum and strontium. (a) shows the phase diagram at no external pressure. No structure with a negative formation energy was identified. (c) adding pressure stabilizes the mix of both elements. (b) under 100 GPa, the convex hull is dominated by the composition LaSr.
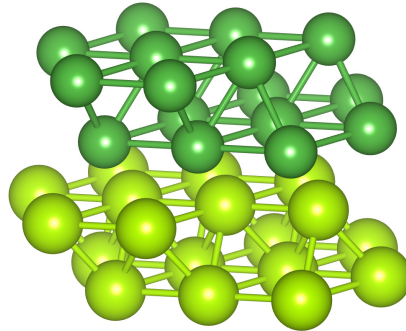
Figure 4.10: LaSr at 100 GPa. The structure consists of alternating slabs of lanthanum (green) and strontium (yellow). Each layer has a width of two atoms.

4.3 Lanthanum, strontium, titanium

The residual binary phase diagrams combine lanthanum, strontium and titanium at zero pressure. They are shown in figure 4.9(a), 4.11(a) and 4.13(a). In contrast to the previously discussed phase diagrams containing aluminum or oxygen, no binary structure with a negative formation energy could be identified here. The Materials Project database [75] also reveals no thermodynamic stable structure.

Pressures up to 100 GPa were applied to the structures to investigate if these conditions help to stabilized some of the structures. The evolution of the minimum formation energy of each composition is shown in figure 4.9(c), 4.11(c) and 4.13(c). To ensure the quality of the reference structures of each element under pressure, additional global structure prediction calculations were performed at pressures of 50 and 100 GPa.

The combination of lanthanum and strontium stabilizes at pressures around 70 GPa to 80 GPa and above. At a pressure of 100 GPa the convex hull of figure 4.9(b) is dominated by the most stable structure with the composition LaSr. In figure 4.9(b), it is the only binary structure with a negative formation energy. The layered structure is shown in figure 4.10 and can be described as a stack of lanthanum and strontium slabs. Within each slab the atoms are arranged triangularly. Both slab types are two atoms thick.

Lanthanum and titanium start mixing in the same pressure regime as lanthanum and strontium (see figure 4.11(c)). However, at a pressure of 100 GPa, several structures of different composition with a negative formation energy were identified. The most stable ones are presented in figure 4.12. The convex hull is defined by $LaTi_7$. The corresponding most stable structure (figure 4.12(a)) consists of lanthanum atoms arranged as cubes with an edge length of 4.5 Å. On each cubic face, a pair of titanium atoms are positioned. Together, they form an icosahedron filled by a 13th titanium atom at the center. The icosahedron is irregular, as its faces are isosceles triangles. The shorter edge (length of 2.2 Å) is positioned on the faces of the lanthanum cube. The longer edges of the icosahedron (length of 2.8 Å) connect titanium atoms on different faces of the cube. The distance between the central titanium atom and another of the icosahedron lies between these two measures (2.5 Å). The most stable structures of $LaTi_3$ and $LaTi_5$ are
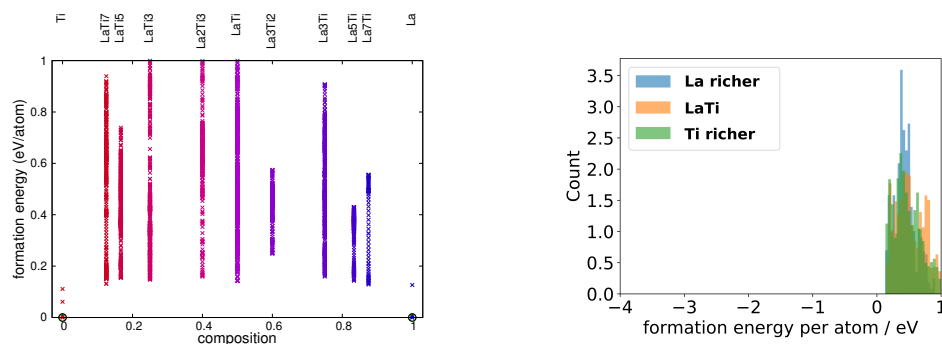
(a) binary phase diagram at 0 GPa
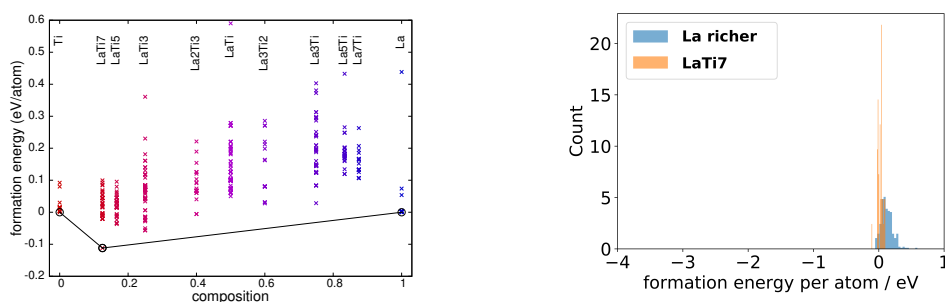
(b) binary phase diagram at 100 GPa
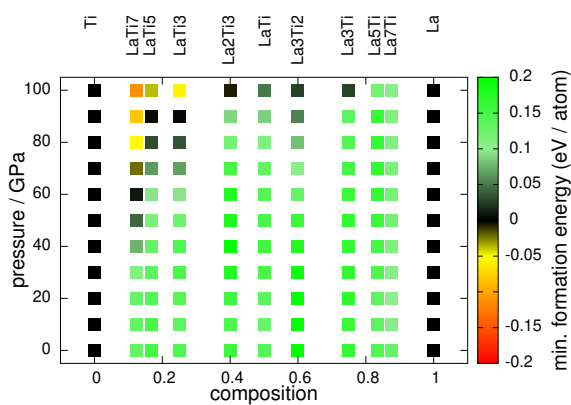
(c) stabilization under pressure

Figure 4.11: Binary materials of lanthanum and titanium. (a) shows the phase diagram at no external pressure. No structure with a negative formation energy was identified. (c) adding pressure stabilizes the mix of both elements. (b) under 100 GPa, the convex hull is dominated by the composition LaTi$_7$. The corresponding structure of lanthanum (green) and titanium (blue) is shown in (a).

(a) LaTi$_7$

(b) LaTi$_3$

(c) LaTi$_5$
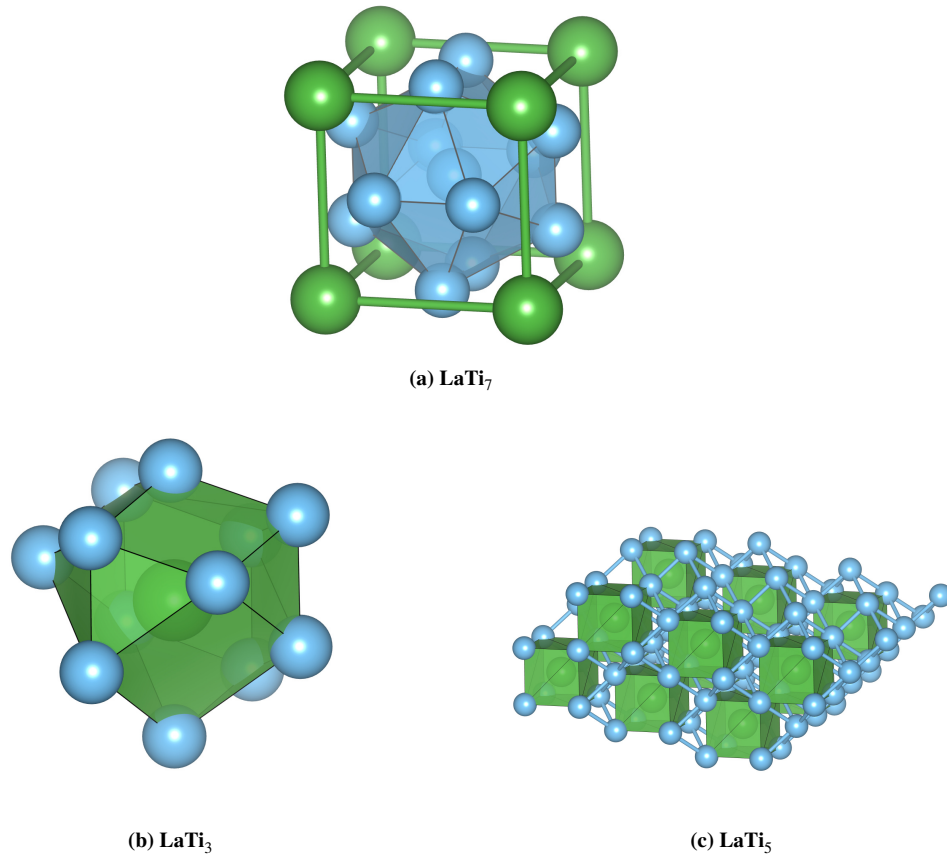
Figure 4.12: The structures of the most stable binary compositions of lanthanum and titanium at 100 GPa. Titanium atoms are blue and lanthanum is green.

sketched in figure 4.12(b) and 4.12(c) . At the composition of LaTi$_3$, titanium forms polyhedra, which contain the lanthanum atom. The polyhedron can be described as cubes with square pyramids attached to four of its side, a quadaugmented cube. However, it is not a Johnson solids, as the faces are irregular as the distance between neighboring titanium atoms varies between 2.5 and 2.9 Å.

Concerning the composition LaTi$_5$, titanium forms cubes, which contain one lanthanum atom. The highlighted connections between the titanum atoms have a length of 2.5 Å. They are shorter than the edge lengths of the highlighted cubes (2.9 Å).

Only strontium and titanium stay separated at pressures up to 100 GPa (see figure 4.13). No binary structure with a negative formation energy could be identified at any pressure between 0 and 100 GPa.
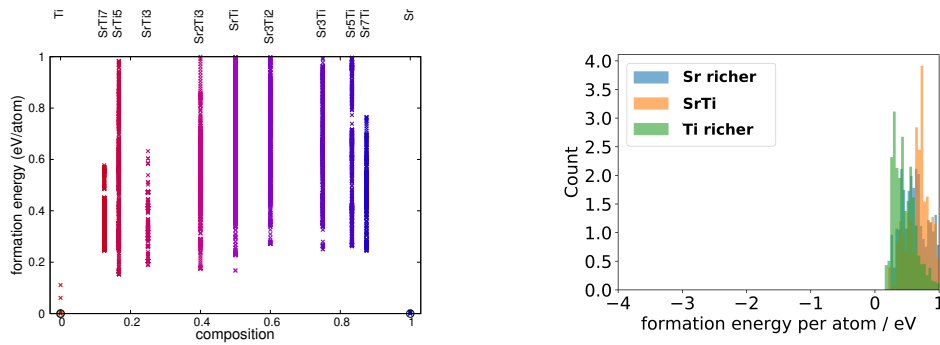
(a) binary phase diagram at 0 GPa
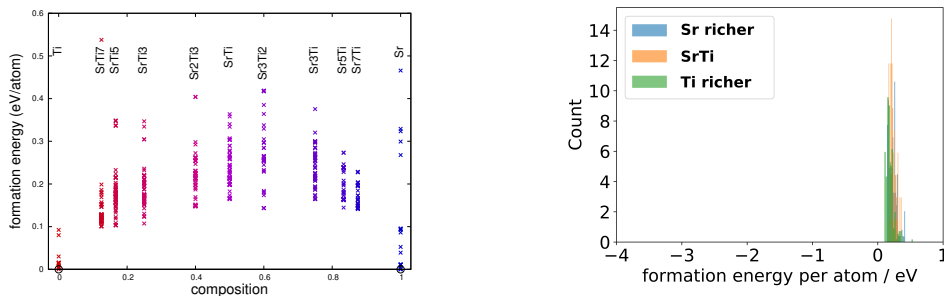
(b) binary phase diagram at 100 GPa
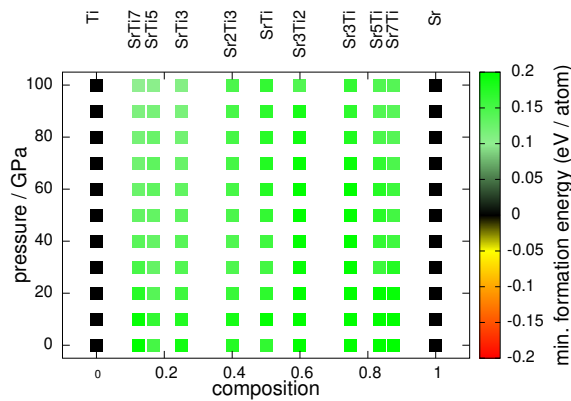
(c) no stabilization under pressure

Figure 4.13: Binary materials of strontium and titanium. (a) shows the phase diagram at no external pressure. No structure with a negative formation energy was identified. Here, adding pressure does not stabilize the mix of both elements (c). (b) under 100 GPa, the convex hull is still a straight line.

Chapter 5

Constrains & grain boundaries

In section 2.5 global structure prediction search was introduced and applied to carbon clathrate structures in section 3.1. There, place holder atoms were added to the carbon atoms in the unit cell to ensure vacancies are built into the carbon framework. It is often useful to perform global structure prediction simulations with geometric restrictions to steer the search into a certain direction. Regarding clathrates for example, following chapter 3 one might be interested in looking for crystal structures containing a certain cage geometry and use global structure prediction techniques to optimize the periodic linkage of the cage. If this search is to restrictive, further degrees of freedom can be created via the cage geometry. Regarding a truncated hexagonal trapezohedron for example, one could constrain a selection of faces and arrange them to form the polyhedron. During the optimization process, these faces are still allowed to shift and rotate relative to each other.

In section 3.1 neither the first nor the second approach is possible. There, all atoms are treated in the same way during the optimization process. Adding constrains restricts the positions of a set of atoms. The movement of some atoms need to be constrained to prevent the cage from dissolving in the residual carbon structure and open up a different search strategy.

Another example besides clathrates is the prediction of 2D-materials [19, 174]. The reconstruction of surfaces or grain boundaries would be possible too. As the simulation cell still contains three spacial dimensions and applies periodic boundary conditions, in these cases the initial configuration needs to contain vacuum, that is supposed to remain and should not vanish during the optimization procedure. Otherwise the result would be a 3D bulk crystal, which was not the center of interest.

5.1 Simple restriction of distances

A software library has been created to restrict the movement of a set of atoms during the global structure prediction process. It has also been used in the work of Borlido *et al.* [19, 174]. The library allows conserving each length and angle of the vectors defining the unit cell, the volume of the unit cell and further allows to conserve the distance between certain atoms. In cases

where the distance between two atoms should be fixed, the difference in forces acting on both atoms A and B needs to be set to zero:

$$0 = \mathbf{F}^{AB} = \mathbf{F}^A - \mathbf{F}^B$$

or rather

$$\forall k \in \{1,2,3\} \qquad 0 = \sum_{j=1}^{3} a_j^k F_j^A + b_j^k F_j^B = \mathbf{a}^k \mathbf{F}^A + \mathbf{b}^k \mathbf{F}^B \tag{5.1}$$

The cartesian coordinate is represented by j. Due to the scalar nature of the lower expression, three parameter sets $(\mathbf{a}^k; \mathbf{b}^k)$ are needed to match the upper expression. Furthermore, the $\mathbf{b}^k$ need to be set to $\mathbf{b}^k = -\mathbf{a}^k$.

Each set conserves the distance between A and B with respect to the orientation of $\mathbf{a}^k$. Consequently if only one set $\mathbf{b}^1 = -\mathbf{a}^1$ is defined, atom A and B are restricted to move each on a plane perpendicular to $\mathbf{a}$. These parameters need to be set in a configuration file like:

			a_1	a_2	a_3	b_1	b_2	b_3
...								
2	A	B	1	0	0	-1	0	0
2	A	B	0	1	0	0	-1	0
2	A	B	0	0	1	0	0	-1
...								

A and B is the index of the corresponding atom. The leading integer '2 ' shows, this line defines a constrain with respect to two particles. Analog, the relation $0 = \mathbf{aF}^A + \mathbf{bF}^B + \mathbf{cF}^C$ is defined by the line '3 A B C a_1 a_2 a_3 b_1 b_2 b_3 c_1 c_2 c_3 '.

5.2 Extended definition of constrains

The basic usage of the first version of the program library is sketched above. Regarding atomic distances enforcing $\mathbf{F}^A - \mathbf{F}^B = \mathbf{0}$ has secondary effects and limits the dynamics beyond the wanted limitations. Now A and B are only allowed to move pairwise parallel to the Cartesian axes. Rotations are not possible. This issue becomes more prominent, when two distances $|\mathbf{r}^{AB}|$ and $|\mathbf{r}^{CD}|$ should be fixed independently from each other in one sample system. Up to now this also conserves the relative orientation of these two vectors $\sphericalangle(\mathbf{r}^{AB}, \mathbf{r}^{CD})$.

To circumvent this issue, one needs to distinguish between an initial, global definition of constrains and their application to the actual geometry of the molecular dynamics step. The syntax introduced above can still be used to define the individual restrictions of an individual structure during the molecular dynamics simutation. But the syntax needs to be modified to define the global, initial constrains. r^{AB} and r^{CD} could be fixed without the discussed limitations by initially defining:

$$
\begin{array}{llll}
\text{dst} & 2 & A & B \\
\text{dst} & 2 & C & D
\end{array}
$$

At each individual molecular dynamics step, this definition needs to be transformed to equation (5.1) by determining the parameter vectors $\mathbf{a}$, $\mathbf{b}$, $\mathbf{c}$ and $\mathbf{d}$. How these parameters are calculated is explained in section 5.2.1. The sections 5.2.2 - 5.2.4 discus how to restrict angles.

A different example highlights the different modes of restricting the distance:

$$
\begin{array}{llllllllll}
\text{fix} & 2 & A & B & 0 & 0 & 1 & 0 & 0 & \text{-1} \\
\text{dst} & 2 & A & B & & & & & &
\end{array}
$$

The first line conserves the distance of the atoms A and B in z-direction. The second line conserves their distance independend of any coordinates. Combination both, the atoms A and B are only allowed to rotate around an axis defined by their center of mass and oriented parallel to the z-axis. However, if no further restrictions are added to any other particle, the translation symmetry of the unit cell leads to the same result as the sample definition in section 5.1.

The described change in the definition of constrains and the corresponding adjustment of the code of the search algorithm allows for a more subtle way to define the restrictions of the system and to expand the field of possible applications concerning global structure prediction. For example, it enables the description of systems composed of clusters, whose vertex positions need to be optimized with respect to each other and the surrounding. Hollow cages can be designed first and can then be constrained individually. The simulation cell can contain further unconstrained atoms to investigate possible geometries of bulk crystals. Furthermore, trigonometric operations are avoid to limit the computational cost of the constrained search. The described strategy also has the advantage that further modes of restriction can be easily added. Only their translation needs to be implemented, which on runtime allows the program to create a set of parameters to be applied to the individual structure.

5.2.1 Fixing distances between two atoms with variable orientation

Before each MD-step the restriction 'dst 2 A B' needs to be adapted to the current geometry. With respect to the geometry, the forces acting on each atom $i \in \{A, B\}$ can be decomposed into $\mathbf{F}^i = \mathbf{F}^i_{\parallel} + \mathbf{F}^i_{\perp}$, where the individual forces can be defined with respect to the axis $\mathbf{r}^{AB} = \mathbf{r}^B - \mathbf{r}^A$:

$$
\mathbf{F}^i_{\parallel} \parallel \mathbf{r}^{AB} \quad \text{and} \quad \mathbf{F}^i_{\perp} \perp \mathbf{r}^{AB}
$$

The forces $\mathbf{F}^A_{\perp}$, $\mathbf{F}^B_{\perp}$ describe a superposition of two motions: One is the collective translation of the pair of atoms A, B perpendicular to the axis $\mathbf{r}^{AB}$ and the second one is a rotation of both atoms around their center of mass. As both individual motions do not affect the distance r^{AB}, only the constrain $\mathbf{F}^A_{\parallel} = \mathbf{F}^B_{\parallel}$ needs to be applied to the geometry at each step of the molecular

dynamics simulation to limit the F^i_j to only allow collective translations of A and B. Each $F^i_\parallel$ can be calculated as the projection of $\mathbf{F}^i$ on the unit vector $\mathbf{r}^{AB}/r^{AB}$:

$$F^i_\parallel = \frac{\mathbf{r}^{AB}}{r^{AB}} \cdot \mathbf{F}^i \qquad \Rightarrow \qquad \mathbf{F}^A_\parallel = \left(\frac{\mathbf{r}^{AB}}{r^{AB}} \cdot \mathbf{F}^A \right) \frac{\mathbf{r}^{AB}}{r^{AB}}$$

$$\mathbf{F}^B_\parallel = \left(\frac{\mathbf{r}^{AB}}{r^{AB}} \cdot \mathbf{F}^B \right) \frac{\mathbf{r}^{AB}}{r^{AB}}$$

$$\mathbf{0} =: \mathbf{F}^A_\parallel - \mathbf{F}^B_\parallel = \frac{\mathbf{r}^{AB}}{\left(r^{AB}\right)^2} \left[\mathbf{r}^{AB} \cdot \left(\mathbf{F}^A - \mathbf{F}^B \right) \right]$$

Independent on the positions of the atoms, this can only be achieved when the square brackets are always equal to zero:

$$0 = \mathbf{r}^{AB} \cdot \left(\mathbf{F}^A - \mathbf{F}^B \right) = \sum_j r^{AB}_j \left(F^A_j - F^B_j \right) \tag{5.2}$$

The new parameters defining the constrain condition are solely defined by the relative distance of the two atoms A and B:

$$a_j = r^{AB}_j \qquad\qquad b_j = -r^{AB}_j \tag{5.3}$$

Cnequently, for each MD-step the constrain 'dst 2 A B' needs to be transformed to:

$$2 \quad A \quad B \quad r^{AB}_1 \quad r^{AB}_2 \quad r^{AB}_3 \quad -r^{AB}_1 \quad -r^{AB}_2 \quad -r^{AB}_3$$

5.2.2 Fixing planar angles

When thinking about fixing the planar angle $\sphericalangle(\mathbf{r}^{AB}, \mathbf{r}^{AC})$, in contrast to the previous example, a third position C needs to be handled. The three points A, B, C define a plane $\square$ and the forces can be decomposed according to the geometry:

$$\mathbf{F}^{AB}_\parallel \parallel \mathbf{r}^{AB} \quad , \quad \mathbf{F}^{AB}_\square \parallel \square \quad \text{and} \quad \mathbf{F}^{AB}_\perp \perp \square$$

$$\mathbf{F}^{AB} = \mathbf{F}^B - \mathbf{F}^A = \underbrace{\mathbf{F}^{AB}_\parallel + \mathbf{F}^{AB}_*}_{\mathbf{F}^{AB}_\square} + \mathbf{F}^{AB}_\perp$$

To perform the decomposition, the proper normal vectors need to be introduced:

$$\mathbf{n} = \frac{\mathbf{r}^{AB} \times \mathbf{r}^{AC}}{|\mathbf{r}^{AB} \times \mathbf{r}^{AC}|} \qquad \text{with} \qquad \mathbf{n} \perp \square$$

$$\mathbf{n}^B = \mathbf{n} \times \frac{\mathbf{r}^{AB}}{r^{AB}} \qquad \text{with} \qquad \mathbf{n}^B \perp \mathbf{r}^{AB}, \, \mathbf{n}^B \parallel \square$$

$$\mathbf{n}^C = \mathbf{n} \times \frac{\mathbf{r}^{AC}}{r^{AC}} \qquad \text{with} \qquad \mathbf{n}^C \perp \mathbf{r}^{AC}, \, \mathbf{n}^C \parallel \square$$

In contrast to $\mathbf{n}$ being perpendicular to the plane $\square$, the $\mathbf{n}^j$ are orthogonal to $\mathbf{r}^{Aj}$ and still parallel to the plane. The forces acting on atom B and C can be introduced accordingly:

$$\mathbf{F}_\perp^{AB} = \mathbf{n} \left(\mathbf{n} \cdot \mathbf{F}^{AB} \right) \qquad \mathbf{F}_\square^{AB} = \mathbf{F}^{AB} - \mathbf{F}_\perp^{AB}$$

$$\mathbf{F}_\perp^{AC} = \mathbf{n} \left(\mathbf{n} \cdot \mathbf{F}^{AC} \right) \qquad \mathbf{F}_\square^{AC} = \mathbf{F}^{AC} - \mathbf{F}_\perp^{AC}$$

The points A, B, C can move in four different ways:

1. translation of the group A, B, C in any direction

2. stretching of $\mathbf{r}^{AB}$, $\mathbf{r}^{AC}$

3. rotation of the plane $\square$

4. rotations of the positions within the plane $\square$

The first two possibilities automatically conserve $\sphericalangle(\mathbf{r}^{AB}, \mathbf{r}^{AC})$ as they only refer to translational movements. As the forces are always taken with respect to A, the rotation axis of case three passes through point A. It needs to be made sure, B rotates around the axis like C does. Therefore the torsional momenta $\mathbf{M}^i$ of B and C need to be the same. In the last case, the situation is similar. Here solely the rotation axis is in plane and not perpendicular to it, so only one different direction for the $\mathbf{M}^i$ needs to be investigated. These two cases of rotation can be combined to:

$$\mathbf{M}^C = \mathbf{r}^{AC} \times \mathbf{F}^{AC} \qquad = \qquad \mathbf{r}^{AB} \times \mathbf{F}^{AB} = \mathbf{M}^B$$

$$0 = \left(\mathbf{r}^{AC} - \mathbf{r}^{AB} \right) \times \mathbf{F}^A + \mathbf{r}^{AB} \times \mathbf{F}^B - \mathbf{r}^{AC} \times \mathbf{F}^C$$

So for any component l it is valid:

$$0 = \sum_{j,k=1}^{3} \varepsilon_{jkl} \left[\left(r_k^C - r_k^B \right) F_j^A + \left(r_k^B - r_k^A \right) F_j^B - \left(r_k^C - r_k^A \right) F_j^C \right] \tag{5.4}$$

The constrain is represented by three sets of parameters $(a_l, b_l, c_l)_j$. Again the parameters are directly defined by the geometry:

$$a_{jl} = \sum_{k=1}^{3} \varepsilon_{jkl} \left(r_k^C - r_k^B \right)$$

$$b_{jl} = \sum_{k=1}^{3} \varepsilon_{jkl} \left(r_k^B - r_k^A \right) \tag{5.5}$$

$$c_{jl} = \sum_{k=1}^{3} \varepsilon_{jkl} \left(r_k^A - r_k^C \right)$$

5.2.3 Fixing dihedral angles

Now four positions A, B, C, D need to be considered to conserve the dihedral angle $\theta(\square_{ABC}, \square_{ABD})$. As A and B are part of both planes, they are reference points of C and D. Local Cartesian coordinates x', y', z' can be introduced according to the geometry (see figure 5.1). There, the position of atom A is chosen as the center of the dashed coordinate system. B is part of the y'-axis, the z'-axis is orthogonal to y' and its orientation is defined by symmetry: The plane (y', z') halves the dihedral angle $\theta(\square_{ABC}, \square_{ABD})$. Consequently, the x'-axis is defined by $\mathbf{e}_{x'} = \mathbf{e}_{y'} \times \mathbf{e}_{z'}$. Besides the positions of the atoms $\mathbf{r}^i$ and their differences $\mathbf{r}^{ij} = \mathbf{r}^j - \mathbf{r}^i$, further vectors can be introduced:

the normal vectors of the planes

$$\mathbf{n}^C = \frac{\mathbf{r}^{AB} \times \mathbf{r}^{AC}}{\left| \mathbf{r}^{AB} \times \mathbf{r}^{AC} \right|}$$

$$\mathbf{n}^D = \frac{\mathbf{r}^{AB} \times \mathbf{r}^{AD}}{\left| \mathbf{r}^{AB} \times \mathbf{r}^{AD} \right|}$$

and the levers

$$\mathbf{d}^B = \mathbf{r}^{AB}$$

$$\mathbf{d}_{i'}^C = \mathbf{r}^{AC} - \left(\mathbf{r}^{AC} \cdot \mathbf{e}_{i'} \right) \mathbf{e}_{i'}$$

$$\mathbf{d}_{i'}^D = \mathbf{r}^{AD} - \left(\mathbf{r}^{AD} \cdot \mathbf{e}_{i'} \right) \mathbf{e}_{i'}$$

So the angle $\sphericalangle(\mathbf{d}^C, \mathbf{d}^D)$ is halved by the plane (y', z').

The movement of the atoms can be decomposed into a different set of restricted and unrestricted movements:

1. collective translation of A, B, C, D; described by $\mathbf{F}^A$ (unrestricted)

2. translation of B parallel to $\mathbf{e}_{y'}$; described by $\left(\mathbf{F}^{AB} \right)_{y'} = \left(\mathbf{F}^B - \mathbf{F}^A \right)_{y'}$ (unrestricted)

3. translation of C and D parallel to their planes (unrestricted)
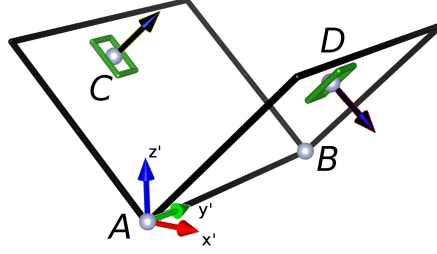
Figure 5.1: Sketch of the geometry of the dihedral angle θ. Besides the positions A, B, C, D and the Cartesian axis x', y', z', the normal vectors $\mathbf{n}^C$, $\mathbf{n}^D$ are shown.

- translation of C parallel to $\mathbf{r}^{AC}$ and D parallel to $\mathbf{r}^{AD}$

- rotation of C and D around A within each plane:

4. collective rotation (restricted)

   a) collective rotation of B, C, D around A / superposition of their rotation around the x' and the z' axis. $\mathbf{M}^B$ is oriented parallel to the $\mathbf{e}_{x'}$, $\mathbf{e}_{z'}$ - plane:

$$\mathbf{M}^B_{x'} = \mathbf{M}^C_{x'} = \mathbf{M}^D_{x'}$$
$$\mathbf{M}^B_{z'} = \mathbf{M}^C_{z'} = \mathbf{M}^D_{z'}$$
$$\mathbf{M}^i \perp \mathbf{r}^{AB}$$

   b) collective rotation around $\mathbf{e}_{y'}$:

$$\mathbf{M}^B_{y'} = 0 \qquad \text{and} \qquad \mathbf{M}^C_{y'} = \mathbf{M}^D_{y'}$$
$$\mathbf{M}^i \parallel \mathbf{r}^{AB}$$

These individual rotations can be distinguished by the orientation of the torsional momenta $\mathbf{M}^i$. So they can be added and the combination of the three rotation modes leads to:

$$0 = \mathbf{M}^C - \mathbf{M}^B$$
$$0 = \mathbf{M}^D - \mathbf{M}^B \tag{5.6}$$

with

$$\mathbf{M}^i = \mathbf{M}^i_{x'} + \mathbf{M}^i_{y'} + \mathbf{M}^i_{z'}$$

Nevertheless the rotation modes possess individual levers $d^j_{i'}$. The individual momenta are written in table 5.1, but they can be combined to simplify equation (5.6) to:

$$0 = \mathbf{r}^{AC} \times \left(\mathbf{F}^{C} - \mathbf{F}^{A}\right) - \mathbf{r}^{AB} \times \left(\mathbf{F}^{B} - \mathbf{F}^{A}\right)$$
$$0 = \mathbf{r}^{AD} \times \left(\mathbf{F}^{D} - \mathbf{F}^{A}\right) - \mathbf{r}^{AB} \times \left(\mathbf{F}^{B} - \mathbf{F}^{A}\right)$$

(5.7)

Nevertheless one needs to have in mind the atoms C and D are allowed to move within their planes unrestrictedly, only the force components perpendicular to their planes need to be restricted. Therefore equation (5.7) becomes:

$$0 = \mathbf{r}^{AC} \times \mathbf{n}^{C} \ \left(\mathbf{F}^{C} - \mathbf{F}^{A}\right) \cdot \mathbf{n}^{C} - \mathbf{r}^{AB} \times \mathbf{n}^{C} \ \left(\mathbf{F}^{B} - \mathbf{F}^{A}\right) \cdot \mathbf{n}^{C}$$
$$0 = \mathbf{r}^{AD} \times \mathbf{n}^{D} \ \left(\mathbf{F}^{D} - \mathbf{F}^{A}\right) \cdot \mathbf{n}^{D} - \mathbf{r}^{AB} \times \mathbf{n}^{D} \ \left(\mathbf{F}^{B} - \mathbf{F}^{A}\right) \cdot \mathbf{n}^{D}$$

(5.8)

This condition leads to:

$$0 = \left[\mathbf{r}^{AC} \left(\mathbf{F}^{C} \cdot \mathbf{n}^{C}\right) - \mathbf{r}^{AB} \left(\mathbf{F}^{B} \cdot \mathbf{n}^{C}\right) - \mathbf{r}^{BC} \left(\mathbf{F}^{A} \cdot \mathbf{n}^{C}\right)\right] \times \mathbf{n}^{C}$$
$$0 = \left[\mathbf{r}^{AD} \left(\mathbf{F}^{D} \cdot \mathbf{n}^{D}\right) - \mathbf{r}^{AB} \left(\mathbf{F}^{B} \cdot \mathbf{n}^{D}\right) - \mathbf{r}^{BD} \left(\mathbf{F}^{A} \cdot \mathbf{n}^{D}\right)\right] \times \mathbf{n}^{D}$$

(5.9)

Ergo it is valid for any i:

$$0 = \sum_{j,k,l} \varepsilon_{ikl} \left[r_k^{AC} F_j^{C} n_j^{C} - r_k^{AB} F_j^{B} n_j^{C} - r_k^{BC} F_j^{A} n_j^{C} \right] n_l^{C}$$
$$0 = \sum_{j,k,l} \varepsilon_{ikl} \left[r_k^{AD} F_j^{D} n_j^{D} - r_k^{AB} F_j^{B} n_j^{D} - r_k^{BD} F_j^{A} n_j^{D} \right] n_l^{D}$$

(5.10)

These equations result for each l into the two conditions that need to be fulfilled :

$$a_{jl} = -\sum_{k,l} \varepsilon_{ikl} \, r_k^{BC} n_j^{C} n_l^{C} \qquad\qquad a_{jl} = -\sum_{k,l} \varepsilon_{ikl} \, r_k^{BD} n_j^{D} n_l^{D}$$

$$b_{jl} = -\sum_{k,l} \varepsilon_{ikl} \, r_k^{AB} n_j^{C} n_l^{C} \qquad \text{and} \qquad b_{jl} = -\sum_{k,l} \varepsilon_{ikl} \, r_k^{AB} n_j^{D} n_l^{D}$$

(5.11)

$$c_{jl} = \sum_{k,l} \varepsilon_{ikl} \, r_k^{AC} n_j^{C} n_l^{C} \qquad\qquad c_{jl} = 0$$

$$d_{jl} = 0 \qquad\qquad\qquad\qquad d_{jl} = \sum_{k,l} \varepsilon_{ikl} \, r_k^{AD} n_j^{D} n_l^{D}$$

Table 5.1: Individual torsional momenta $\mathbf{M}_{j'}^{i}$ of each atom around each axis. Each line describes one rotation axis and each row one atom. $\mathbf{M}_{y'}^{B}$ is always $\mathbf{0}$ as $\mathbf{r}^{AB} \parallel \mathbf{e}_{y'}$.

	B	C	D
x'	$\mathbf{r}^{AB} \times \mathbf{e}_{z'} \left(\mathbf{F}^{AB} \cdot \mathbf{e}_{z'}\right)$	$\mathbf{d}_{x'}^{C} \times \mathbf{e}_{z'} \left(\mathbf{F}^{AC} \cdot \mathbf{e}_{z'}\right)$	$\mathbf{d}_{x'}^{D} \times \mathbf{e}_{z'} \left(\mathbf{F}^{AD} \cdot \mathbf{e}_{z'}\right)$
y'	$\mathbf{0}$	$\mathbf{d}_{y'}^{C} \times \mathbf{n}^{C} \left(\mathbf{F}^{AC} \cdot \mathbf{n}^{C}\right)$	$\mathbf{d}_{y'}^{D} \times \mathbf{n}^{D} \left(\mathbf{F}^{AD} \cdot \mathbf{n}^{D}\right)$
z'	$\mathbf{r}^{AB} \times \mathbf{e}_{x'} \left(\mathbf{F}^{AB} \cdot \mathbf{e}_{x'}\right)$	$\mathbf{d}_{z'}^{C} \times \mathbf{e}_{x'} \left(\mathbf{F}^{AC} \cdot \mathbf{e}_{x'}\right)$	$\mathbf{d}_{z'}^{D} \times \mathbf{e}_{x'} \left(\mathbf{F}^{AD} \cdot \mathbf{e}_{x'}\right)$

5.2.4 Fixing solid angles

Fixing a solid angle $\Omega(\mathbf{r}^{AB}, \mathbf{r}^{AC}, \mathbf{r}^{AD})$ would be the logic follow up to fixing planar and dihedral angles. Nevertheless one needs to think about cases where it is useful to apply this constrain without adding further restrictions. These are cases where the value, but not the shape, of the solid angle should be conserved, which hardly makes sense from the symmetric point of view. Nevertheless fixing the shape of a solid angle fixes its value too. This can be achieved by fixing two of the three dihedral angles present at the vertex of interest.

Chapter 6

Summary & outlook

Within this dissertation, global structure prediction search was showcased in different contexts. The obtained structures were compared with reference structures of similar composition and with structures of the constituent elements to estimate the stability of the structures. Global structure predictions do not deliver a reaction path for synthesizing or directly give a reason why there are no structures that are more stable. Correspondingly a detailed analysis of the geometry was presented. The possibility of stabilizing structures under pressure was investigated as well. Therefore, pressures up to 50 or even 100 GPa were applied. Although these are values up to six orders of magnitude above atmospheric pressure, they should still be applicable in experiments as experiments have been reported applying much higher pressures [175].

To enable the possibility to predict structures besides bulk structures, for example surfaces or grain boundaries, constrained global structure predictions were introduced. Furthermore, a strategy was outlined to enable constrained search besides adding completely rigid structures to the simulation cell. Adding constrained pieces of known bulk crystal structures allows to investigate the transition between different grains. However, if one wants to investigate how certain promising cage geometries can be combined in a 3D bulk structure, it is useful to allow cages to adapt to their environment and not only force the environment to adapt to the cages.

Up to now, the predictions were always performed for a canonical ensemble of atoms. The presented phase diagrams were created by performing multiple prediction runs of different composition and number of atoms in the unit cell. Going further and allowing runs for a grand canonical ensemble would open up a new search perspective [176–178]. Independent of this transition, it is going to be interesting to see the speed-up of the prediction calculations due to the substitution of DFT calculations by methods of machine learning.

Furthermore, based the training sets created by the binary structures of chapter 4, we can report the successful identification of a first stable quasi crystal structure of barium oxide by Ahmad W. Huran, Hai-Chen Wang and Miguel A. L. Marques. Further details are in the process of publication.

Appendix A

A.1 Polyhedra

Polyhedra are classified in a variety of groups depending on their symmetry. As different groups of convex polyhedra are investigated in section 3.2, their definition needs to be introduced. The presented information relies on [179–184]. All in all only convex (bubble-like) polyhedra are discussed and concave polyhedra (star-like) are not further taken into account. To visualize polyhedra, there exist more possibilities than a 2D parallel projection of their 3D shape. A net graph can be used to highlight the composition and arrangement of the faces (figure A.1 and A.2). All polyhedra which show only regular faces are divided in the following groups:

Platonic solids

In Platonic solids each face is a regular polygon and all faces of one solid are arranged congruently to each other. This also means, all vertices are symmetric to each other. Sometimes Platonic solids are also referred to as regular polyhedra. There are only five Platonic solids: tetrahedron, cube / hexahedron, octahedron, dodecahedron and icosahedron (see figure A.1). The solids are named referencing the number of their 4, 6, 8, 12 and 20 faces.

Archimedean solids

To be called an Archimedean solid, the faces of a polyhedron still need to be regular polygons, but all faces of a solid do not need to be congruent anymore. Nevertheless each vertex still connects the same group of faces in the same way. So any vertex is still congruent to any vertex of the same solid. There are 13 different Archimedean solids. Five of them can be constructed from the Platonic solids by truncating them. They are shown in figure A.2. The arrangements of different faces creates a obvious geometric difference to the Platonic solids shown in figure A.1.

Johnson solids

Like Platonic and Archimedean solids, Johnson solids are convex polyhedra and solely show regular polygon faces. In contrast to the previous groups discussed here, the symmetry of the
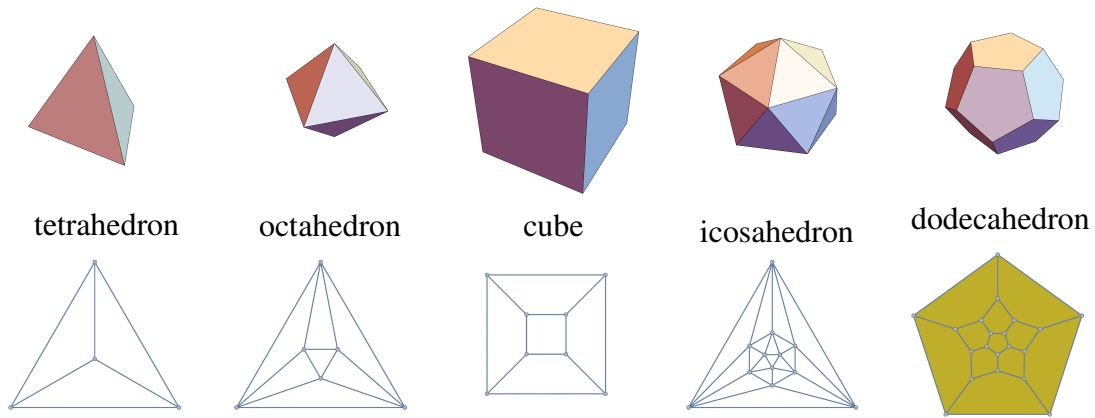
Figure A.1: Different possibilities to visualize polyhedra. Exemplary all Platonic polyhedra are shown. Below each figure on the top, the corresponding net graph is shown, highlighting the arrangement of the faces. The outer polygon surrounding each net graph represents a face too. Here, pentagons are colored to highlight them from other faces.
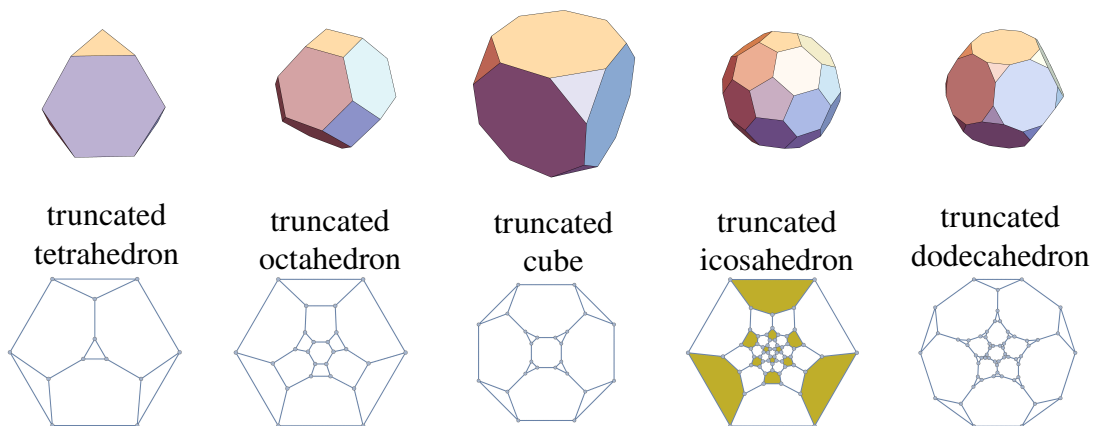
Figure A.2: Examples of Archimedean solids: the truncated Platonic solids. For each polyhedron the conventional plot is shown at the top and the corresponding net graph is shown below. Here, only the truncated icosahedron shows pentagonal faces. They are marked yellow to differentiate them better from the hexagonal faces. Furthermore, it is easy to see each pentagonal face of the truncated icosahedron is surrounded by hexagons.

vertices has vanished. One example out of the 92 different Johnson solids, where this asymmetry is easy to see, is the square pyramid. It has four triangular and one square face. Four of its five vertices connect two triangular with the square face and the fifth vertex connects all four triangular faces.

Prisms and antiprisms

Analog to a rectangle being created when a straight line segment is duplicated and shifted perpendicular to its orientation, a prism is created when a polygon is duplicated and moved perpendicular to its original plane. Connecting each vertex of the original polygon with its copy of the second polygon reveals each vertex has three neighbor vertices. Besides the basic polygon, only rectangles or more specific squares appear as faces. Consequently, there is only one Platonic solid, which is also a prism: the cube.

Antiprisms are created in a similar way, but the two copies of the initial polygon are rotated against each other by $1/2$ of their N-fold rotation symmetry. Connecting the vertices between these two planes, regular triangles appear as further faces. Due to this construction, the trigonal antiprism is a Platonic solid too. It is identical to the octahedron.

Within a non-sheared (anti)prism, the vertices are symmetric to each other. In contrast to Platonic and Archimedean solids, (anti)prisms with many vertices show more of a cylindrical than a spherical shape. Due to the geometric similarity of different (anti)prisms, the radius of the circumsphere can be calculated directly by the number of vertices N of the (anti)prism and the edge length a_0:

$$R_{\text{prism}} = \frac{a_0}{2} \sqrt{1 + \frac{2}{1 - \cos \frac{4\pi}{N}}} \tag{A.1}$$

$$R_{\text{antiprism}} = \frac{a_0}{2} \sqrt{1 + \frac{1 + \cos \frac{2\pi}{N}}{1 - \cos \frac{4\pi}{N}}} \tag{A.2}$$

Both equations can simply be derived by dissecting the geometry and applying the Pythagorean theorem. It is easy to see, both radii scale similarly for large N.

Euler characteristic

Besides the classification according to the symmetry of the vertices, the Euler characteristic χ can be used to classify polyhedra too [185, 186]. It is defined by the number of vertices v, the number of edges e and number of faces f of a polyhedron:

$$\chi = v - e + f \tag{A.3}$$

Platonic, Archimedean, Johnson solids, prisms and antiprisms and even a sphere share the same Euler characteristic $\chi = 2$, indicating to represent the same topology.

A.2 Angles

Looking for carbon clathrates in section 3.2, three different types of angles are discussed to characterize and compare geometries. The basic concepts and the used equations to calculate them from the vertex positions are introduced in this section. To talk about planar angles might sound trivial, but it is used as an entry point and should be mentioned to complete the picture of the other angles.

Planar angles

The planar angle φ is a measure regarding the different orientation of two intersecting lines (see figure A.3(a), [187]). Analog it is a measure regarding the relative orientation of two vectors $\mathbf{r}_1$ and $\mathbf{r}_2$ to each other within one plane. Using the definition of the scalar product of vectors, the angle φ can be calculated straightforward:

$$\begin{aligned}
\varphi(\mathbf{r}_1, \mathbf{r}_2) &\in [0, \pi] \\
\varphi(\mathbf{r}_1, \mathbf{r}_2) &= \arccos \frac{\mathbf{r}_1 \cdot \mathbf{r}_2}{r_1 r_2}
\end{aligned} \tag{A.4}$$

The most common units for planar angles are degree with a full angle of $360\,°$ and radian measure, where the angle is equal to the length of the bow section of a unit circle. Consequently the full angle is equal to 2π, when described with radian measure.

Regarding regular polygons with N vertices, their internal planar angle $\varphi_{\mathrm{int}}(N)$ can be calculated by partitioning the polygon into N isosceles triangles of neighboring vertices and the center of the polyhedron. Using the law of the sum of internal angles for planar triangles, the internal angle of the regular polygon can be calculated by:

$$\varphi_{\mathrm{int}}(N) = \pi \left(1 - \frac{2}{N}\right) \tag{A.5}$$

Solid angles

Analog to defining a planar angle φ as the length of the bow segment of a unit circle, the solid angle Ω is a two-dimensional angle. It is defined as the size of the corresponding segment of a unit sphere (see figure A.3(b)) [188]. While the planar angle φ is spanned between two lines or vectors, Ω is defined by three planes or three position vectors. Accordingly, solid angles are
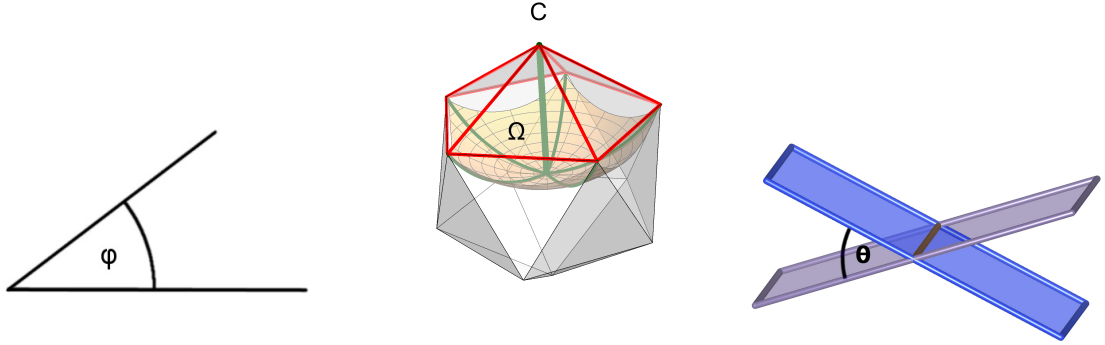
(a) Planar angle φ between two lines.

(b) Solid angle Ω (orange) of an icosahedron spanned at the vertex C. It is defined by the red edges. The green lines highlight partitions of Ω, where each part is defined by only three lines and can be calculated via equation (A.7).

(c) Dihedral angle θ between two planes.

Figure A.3: Sketches of (a) planar, (b) solid and (c) dihedral angle.

measured in steradian (sr) and a full angle is equal to 4π. The corresponding equation regarding three position unit vectors $\mathbf{e}_j = \frac{\mathbf{r}_j}{r_j}$ is presented by Folke Eriksson in [189] :

$$\tan\frac{\Omega}{2} = \frac{\left|\mathbf{e}_1 \cdot (\mathbf{e}_2 \times \mathbf{e}_3)\right|}{1 + \mathbf{e}_2 \cdot \mathbf{e}_3 + \mathbf{e}_3 \cdot \mathbf{e}_1 + \mathbf{e}_1 \cdot \mathbf{e}_2} \tag{A.6}$$

Rewriting equation (A.6) for position vectors $\mathbf{r}_j$ of arbitrary length leads to equation (A.7). Furthermore, reformulating the equation with the 'arctan' instead of the 'tan'-function compensates for the pole of equation (A.6) at $\Omega = \pi$. Due to the nature of the 'tan'-function one needs to distinguish two cases depending on the shown fraction ξ. There are only two cases as no angle Ω larger than 2π can be spanned directly by three vectors. Such an angle $\Omega_{\text{large}} > 2\pi$ can only be represented in equation (A.7) by its adjacent angle $4\pi - \Omega_{\text{large}}$.

$$\Omega(\mathbf{r}_1, \mathbf{r}_2, \mathbf{r}_3) \in [0, 2\pi]$$

$$\Omega(\mathbf{r}_1, \mathbf{r}_2, \mathbf{r}_3) = \begin{cases} 2 \arctan \xi(\mathbf{r}_1, \mathbf{r}_2, \mathbf{r}_3) & \text{for} \quad \xi \geq 0 \\ 2\left(\pi + \arctan \xi(\mathbf{r}_1, \mathbf{r}_2, \mathbf{r}_3)\right) & \text{for} \quad \xi < 0 \end{cases} \tag{A.7}$$

$$\text{with} \qquad \xi(\mathbf{r}_1, \mathbf{r}_2, \mathbf{r}_3) = \frac{\left|\mathbf{r}_1 \cdot (\mathbf{r}_2 \times \mathbf{r}_3)\right|}{r_1 r_2 r_3 + r_1(\mathbf{r}_2 \cdot \mathbf{r}_3) + r_2(\mathbf{r}_3 \cdot \mathbf{r}_1) + r_3(\mathbf{r}_1 \cdot \mathbf{r}_2)}$$

If a vertex of a convex polyhedron connects more than three edges, equation (A.7) canot be applied directly. First, the solid angle needs to be partitioned like the green lines show in

figure A.3(b). The individual solid angles of the sections can be calculated by equation (A.7). Their sum is the desired solid angle.

Dihedral angles

While the planar angle φ is a measure in two dimensions between one-dimensional objects and the solid angle Ω is measured analog as a two-dimensional object in three dimensions, dihedral angles θ are planar angles between planes or more specific their normal vectors (figure A.3(c), [190]). Similar to the planar angle, degree and radian measure are used as units. Regarding the dihedral angle spanned by the two planes A and B, the orientation of each plane can be characterized by three of its points $\mathbf{r}_{A1}, \mathbf{r}_{A2}, \mathbf{r}_{A3}$ and $\mathbf{r}_{B1}, \mathbf{r}_{B2}, \mathbf{r}_{B3}$ or the vectors $\mathbf{n}_A$, $\mathbf{n}_B$ perpendicular to the planes:

$$\mathbf{n}_A = (\mathbf{r}_{A2} - \mathbf{r}_{A1}) \times (\mathbf{r}_{A3} - \mathbf{r}_{A1})$$
$$\mathbf{n}_B = (\mathbf{r}_{B2} - \mathbf{r}_{B1}) \times (\mathbf{r}_{B3} - \mathbf{r}_{B1})$$

$$\theta(\mathbf{n}_A, \mathbf{n}_B) \in [0, \pi]$$
$$\theta(\mathbf{n}_A, \mathbf{n}_B) = \arccos \frac{\mathbf{n}_A \cdot \mathbf{n}_B}{n_A n_B} \tag{A.8}$$

A.3 Characterizing polyhedra - calculation issues

Many polyhedra, in fact more than mentioned in section A.1, are implemented in Mathematica [134]. It is a useful source to analyze the geometry of the vertices and export vertex coordinates as a basis to create structure files for DFT calculations. Besides these coordinates, regarding angles only a function regarding dihedral angles is implemented to directly calculate them. To calculate all planar and solid angles for all the polyhedra introduced in section A.1 and for further convex cage structures in section 3.2, several strategies have been created. Each evolved from the predecessor to resolve its issues.

The purpose of this section is to give an example of the issues creating an algorithm and its evolution and to furthermore give an example on how to compare the result of multiple algorithms and on how to identify the wrong results within deviating data. Furthermore, a bug in the basic software has been identified.

The main problem of the different algorithms was the correct identification of the two neighbors of a third vertex sharing a face of the polyhedron. The corresponding calculation of the planar, dihedral and solid angles is performed by applying the equations introduced in section A.2 to this list of vertices.

There are two main ways to check the strategies for errors: One possibility is to calculate all planar angles and to check them for angles not represented by any regular polygon. A second possibility relies on dihedral angles. They can be compared with the result of the implemented function of Mathematica. This second check lead to surprising deviations.

The final, complete characterization of polyhedra is shown in figure 3.11 on page 35.

1st attempt

1. scan over all vertices as centers of the angle for a given polyhedron

2. for each center: find all neighboring vertices

3. scan within those neighbors of a vertex all pairs of vertices neighboring each other too: sort the initial neighbor list of the central vertex for each neighbor (second vertex) by the distance to them and take the two closest vertices as third vertices sharing a face with the second one

4. calculate the angle for each of the two triples (center, 2nd partner, 3rd partner)

This attempt shows issues for example with the hexagonal antiprism (see figure A.4(a)). As the distance $|\overline{BD}|$ is smaller than $|\overline{BC}|$, the vertices of the faces are incorrectly detected and the angle $\sphericalangle BAD$ inside of the polyhedron is calculated instead of the angle $\sphericalangle BAC$ within the top face. This error of detecting neighbors does not only impact the calculation of the planar angles, but also impacts the calculation of dihedral and solid angles. There, neighboring vertices need to be identified as well.

2nd attempt

1. for a given polyhedron scan over all vertices as centers of the angle

2. for each center: find all neighboring vertices

3. within those neighbors: create all triples of vertices with the centering vertex and neighbours as 2nd and 3rd partner

4. test: Is the planar angle of these vertices represented by a regular polygon?
   If it does, accept the triple of vertices to share one face, otherwise neglect it.

This strategy lead to an issue for example with the icosahedron (see figure A.4(b)), where not only triangles but pentagonal faces are detected too. It is correct the angle $\sphericalangle BAC$ is part of a pentagon, but this pentagon lies inside the icosahedron and does not represent a face.
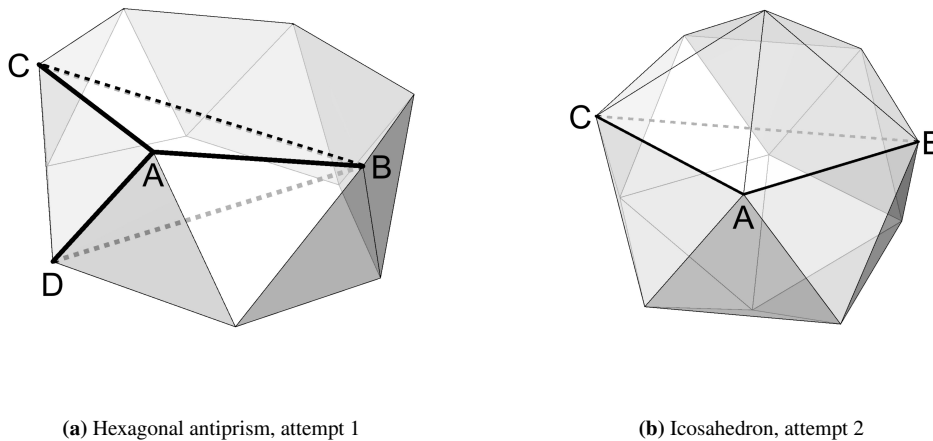
(a) Hexagonal antiprism, attempt 1

(b) Icosahedron, attempt 2

Figure A.4: Example issues of detecting the correct set of vertices to calculate angles. The images show example errors of the first and second attempt to identify the proper set of vertices $\{A, B, C\}$ sharing one face. These sets are needed to calculate all angles of the investigated polyhedra. In figure (a) the planar angle $\sphericalangle BAD$ is calculated despite lying inside the polyhedron and $\sphericalangle BAC$ is ignored. In figure (b) $\sphericalangle BAC$ is calculated although is not part of the surface of the polyhedron.

3rd attempt

1. scan over all vertices as centers of the angle for a given polyhedron

2. for each center: find all neighboring vertices and describe their coordinates in cylindrical coordinates on a cylinder which central axis passes through the center of the polyhedron and the vertex, which currently is investigated for neighbors

3. order these neighbors by their azimuth angle to identify the correct pairs sharing one face

4. calculate angles with the neighboring pairs of neighbors

With this 3rd strategy, no awkward planar angles could be identified anymore. Nevertheless comparing the dihedral angles calculated by this strategy with those angles calculated directly by the implemented function showed deviations listed in table A.1:
Regarding the gyroelongated square dipyramid which combines two square pyramids with a square antiprism (see figure A.5(a)), Mathematica 10.0 [134] identifies an additional dihedral angle of 30.7°. According to the program, this angle occurs in the lower half of the polyhedron between the faces (5,13), (6,14), (7,15) and (8,16). Obviously this classification violates the symmetry of the polyhedron, as the dihedral angles on the upper half of the polyhedron, between the faces (1, 12), (2, 9), (3, 10) and (4, 11) are identified with 158.6°. Furthermore, both angles do not add up to π, so it is not an error about choosing the supplementary angle. Comparing this deviation with Mathematica 11.2 [191] resolves this dispute as a bug of the implemented function of Mathematica 10.0. The dihedral angle of 30.7° does not appear in Mathematica 11.2 any more and the dihedral angles represent the symmetry of the polyhedron correctly.

Repeating the calculation of the angles for the same list of polyhedra with Mathematica 11.2 reveals a deviation regarding the gyroelongated square pyramid (see figure A.5(b)). The angle are listed in table A.1 too. The largest dihedral angle identified by my algorithm and Mathematica 10.0 is characterized with 158.6°, whereas Mathematica 11.2 identifies the largest dihedral angles with 149.3°. It is located between the faces (2, 13), (3, 10), (4, 11) and (5, 12). Despite this being the region present in both gyroelongated square (di)pyramids discussed here, Mathematica 11.2 does not calculate the same dihedral angles. As the other presented calculation methods of this angle reveal a dihedral angle of 158.6° in both pyramids and this angle is also present in the dipyramid, I consider the 149.3° as a bug, It has been reported to Wolfram Research, the creator of Mathematica.

Table A.1: **Comparison of dihedral angles identified by different methods.** Wrong identified angles are printed bold. In both tested versions of Mathematica the command 'PolyhedronData[*polyhedron*,"DihedralAngles"]' has been used to calculate the dihedral angles. The calculations for attempt 3 have been performed on the same machines as the other two cases and has been repeated with both versions of Mathematica.

polyhedron	attempt 3	Mathematica 10.0 [134]	Mathematica 11.2 [191]
		30.7°	
gyroelongated	109.5°	109.5°	109.5°
square dipyramid	127.6°	127.6°	127.6°
	158.6°	158.6°	158.6°
	103.8°	103.8°	103.8°
gyroelongated	109.5°	109.5°	109.5°
square pyramid	127.6°	127.6°	127.6°
	158.6°	158.6°	**149.3°**
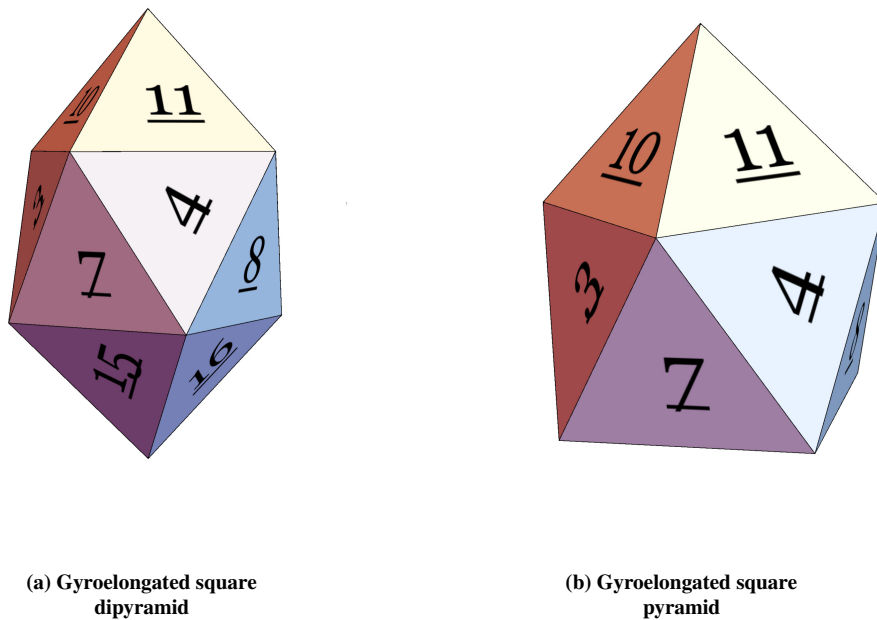
(a) Gyroelongated square
dipyramid

(b) Gyroelongated square
pyramid

Figure A.5: Issues of calculating the correct dihedral angles of polyhedra. The pictures above show the two
Johnson solids gyroelongated square dipyramid (a) and gyroelongated square pyramid (b) with labeled
faces. On both polyhedra one of the investigated versions of Mathematica struggled to evaluate
the dihedral angles properly. These are the only two polyhedra out of the investigated Platonic,
Archimedean, Johnson solids and (anti)prisms where such problems occurred. The angles are listed
in table A.1.

A.4 Spirals

Separating the order of the vertices on the spiral from the order of the projected polygon

The basic construction of spirals is introduced in section 3.3.3. There, the projection of neighboring vertices of the spiral are also neighbors and are visited consecutively when traveling along the spiral. However, this is not the case on all possible spirals. When moving along the spiral from one vertex to the next, l vertices can be skipped in the projection. For these spirals the coordinates of the vertices are:

$$\mathbf{r}_{k,l}(n, z_0, R) = \begin{pmatrix} R\cos 2\pi \frac{k(1+l)}{n} \\ R\sin 2\pi \frac{k(1+l)}{n} \\ z_0 \frac{k}{n} \end{pmatrix} \tag{A.9}$$

Furthermore, it is possible to add another parameter to allow for a pairwise non-equal separation along the z-axis by introducing l_1 and l_2 instead of only l. This geometry can be seen at a DNA double helix for example. l_1 and l_2 are still the number of vertices skipped in the projection between neighboring vertices of the spiral. Going forward l_1 is applied when going from even vertices $2k$ to odd $2k+1$ and l_2 is used going from odd $2k+1$ to even $2(k+1)$. In this case the vertices need to be defined as pairs of even and odd vertices:

$$\mathbf{r}_{2k,l_1,l_2}(n, z_0, R) = \begin{pmatrix} R\cos 2\pi \frac{2k+k(l_1+l_2)}{n} \\ R\sin 2\pi \frac{2k+k(l_1+l_2)}{n} \\ z_0 \frac{2k}{n} \end{pmatrix}$$

$$\mathbf{r}_{2k+1,l_1,l_2}(n, z_0, R) = \begin{pmatrix} R\cos 2\pi \frac{2k+1+(k+1)l_1+kl_2}{n} \\ R\sin 2\pi \frac{2k+1+(k+1)l_1+kl_2}{n} \\ z_0 \left(\frac{2k+1}{n} + \zeta(l_1, l_2) \right) \end{pmatrix} \tag{A.10}$$

ζ describes the different z-shift in this asymmetric case. One can go back to the symmetric case by setting $l_1 = l_2 = l$ and it is easy to see equation (A.10) becomes equation (A.9) while ζ vanishes.

Bibliography

[1] P. Hohenberg and W. Kohn, "Inhomogeneous electron gas," *Physical Review*, vol. 136, pp. B864–B871, 1964.

[2] W. Kohn and L. J. Sham, "Self-consistent equations including exchange and correlation effects," *Physical Review*, vol. 140, pp. A1133–A1138, 1965.

[3] M. Gimbutas, R. J. Braidwood, H. L. Movius, F. M. Keesing, R. M. Adams, and R. Pittioni, "Stone Age | Definition, Tools, Art, & Facts | Britannica.com." `https://www.britannica.com/event/Stone-Age`. Accessed: 2018-12-18.

[4] R. Erbrecht, *Das große Tafelwerk : [Sekundarstufen I und II] ; ein Tabellen- und Formelwerk für den mathematisch-naturwissenschaftlichen Unterricht bis zum Abitur.* Berlin: Volk-und-Wissen-Verl, 1999.

[5] A. Augustyn, A. Zeidan, A. Zelazko, A. Eldridge, A. McKenna, A. Tikkanen, A. Gadzikowski, B. A. Schreiber, B. Duignan, D. Mahajan, D. Promeet, E. Goldstein, E. Rodriguez, E. Gregersen, G. Shukla, G. Liesangthem, G. Lotha, G. Young, H. Bolzon, J. E. Luebering, J. Wallenfeldt, J. Hibler, J. P. Rafferty, K. Gupta, K. Rogers, K. Chmielewski, K. Manchanda, K. Heintz, L. Chaveriat, L. Dixon, M. Matthias, M. Petruzzello, M. Ray, M. Metych, P. Bauer, P. Riley, P. Bhathya, S. Vasich, S. Hollar, S. Singh, G. Shweta, and S. Seddon, "Bronze Age | Britannica.com." `https://www.britannica.com/event/Bronze-Age`. Accessed: 2018-12-18.

[6] A. Augustyn, A. Zeidan, A. Zelazko, A. Eldridge, A. McKenna, A. Tikkanen, A. Gadzikowski, B. A. Schreiber, B. Duignan, D. Mahajan, D. Promeet, E. Goldstein, E. Rodriguez, E. Gregersen, G. Shukla, G. Liesangthem, G. Lotha, G. Young, H. Bolzon, J. E. Luebering, J. Wallenfeldt, J. Hibler, J. P. Rafferty, K. Gupta, K. Rogers, K. Chmielewski, K. Manchanda, K. Heintz, L. Chaveriat, L. Dixon, M. Matthias, M. Petruzzello, M. Ray, M. Metych, P. Bauer, P. Riley, P. Bhathya, S. Vasich, S. Hollar, S. Singh, G. Shweta, and S. Seddon, "History of Europe - The Metal Ages | Britannica.com." `https://www.britannica.com/topic/history-of-Europe/The-Metal-Ages`. Accessed: 2018-12-18.

[7] L. Vitos, *Alloy steel: Properties and use first-principles quantum mechanical approach to stainless steel alloys.* Janeza Trdine 9, 51000 Rijeka, Croatia: InTech, 2011.

[8] H.-W. Schütt, "Martin Heinrich Klaproth als Archäometer," *Chemie in unserer Zeit*, vol. 23, no. 2, pp. 50–52, 1989.

[9] A. B. Reed, "The history of radiation use in medicine," *Journal of Vascular Surgery*, vol. 53, no. 1, Supplement, pp. 3S–5S, 2011.

[10] F. P. Carvalho, "Marie Curie and the discovery of radium," in *The new uranium mining boom: Challenge and lessons learned* (B. Merkel and M. Schipek, eds.), pp. 3–13, Berlin Heidelberg: Springer, 2012.

[11] O. Hahn, "Über eine neue Erscheinung bei der Aktivierung mit Aktinium," *Physikalische Zeitschrift*, vol. 10, pp. 81–88, 1909.

[12] O. Hahn, "Über ein neues radioaktives Zerfallsprodukt im Uran," *Naturwissenschaften*, vol. 9, pp. 84–84, 1921.

[13] L. Meitner and O. R. Frisch, "Disintegration of uranium by neutrons: A new type of nuclear reaction," *Nature*, vol. 143, pp. 239–240, 1939.

[14] O. Hahn and F. Strassmann, "Über den Nachweis und das Verhalten der bei der Bestrahlung des Urans mittels Neutronen entstehenden Erdalkalimetalle," *Naturwissenschaften*, vol. 27, no. 1, pp. 11–15, 1939.

[15] J. Chadwick, "The existence of a neutron," *Proceedings of the Royal Society of London. Series A, Containing Papers of a Mathematical and Physical Character*, vol. 136, no. 830, pp. 692–708, 1932.

[16] A. Einstein, "Ist die Trägheit eines Körpers von seinem Energieinhalt abhängig?," *Annalen der Physik*, vol. 323, no. 13, pp. 639–641, 1905.

[17] T. Mang and C. Busch, "Lubricants in the tribological system," in *Lubricants and lubrication* (W. Dresel and T. Mang, eds.), ch. 2, pp. 11–30, John Wiley & Sons, Ltd, 2017.

[18] W. Choi, I. Lahiri, R. Seelaboyina, and Y. S. Kang, "Synthesis of graphene and its applications: A review," *Critical Reviews in Solid State and Materials Sciences*, vol. 35, no. 1, pp. 52–71, 2010.

[19] P. Borlido, C. Steigemann, N. N. Lathiotakis, M. A. L. Marques, and S. Botti, "Structural prediction of two-dimensional materials under strain," *2D Materials*, vol. 4, no. 4, p. 045009, 2017.

[20] K. S. Ibrahim, "Carbon nanotubes-properties and applications: A review," *Carbon letters*, vol. 14, no. 3, pp. 131–144, 2013.

[21] E. Salernitano and C. Migliaresi, "Composite materials for biomedical applications: A review," *Journal of Applied Biomaterials and Biomechanics*, vol. 1, no. 1, pp. 3–18, 2003.

[22] A. L. Shimpi, "Inside ATI & NVIDIA: How they make frames fly." `https://www.anandtech.com/print/998/`, 2002. Accessed: 2019-11-04.

[23] "TITAN RTX Ultimate PC Graphics Card with Turing | NVIDIA." `https://www.nvidia.com/en-us/deep-learning-ai/products/titan-rtx/`. Accessed: 2019-11-05.

[24] P. Alcron, "AMD Ryzen 9 3900X and Ryzen 7 3700X Review: Zen 2 and 7 nm Unleashed." `https://www.tomshardware.com/reviews/ryzen-9-3900x-7-3700x-review,6214.html`, 2019. Accessed: 2019-11-05.

[25] R. Zafar, "Apple A13 For iPhone 11 Has 8.5 billion transistors, quad-core GPU." `https://wccftech.com/apple-a13-iphone-11-transistors-gpu/`, 2019. Accessed: 2019-11-08.

[26] G. E. Moore, "Cramming more components onto integrated circuits," *Electronics*, vol. 38, no. 8, 1965.

[27] M. Sauter, "EUV-Halbleiterfertigung: Wie Chips aus Plasma-Fladen entstehen - Golem.de." `https://www.golem.de/news/euv-halbleiterfertigung-wie-chips-aus-plasma-fladen-entstehen-1908-130247.html`, 2019. Accessed: 2019-08-29.

[28] Leonidas, "Die Flächen-normierten Fertigungskosten steigen nach dem 14 / 16 nm - Prozeß um +30 % pro Node | 3DCenter.org." `https://www.3dcenter.org/news/die-flaechen-normierten-fertigungskosten-steigen-nach-dem-1416nm-prozess-um-30-pro-node`, 2019. Accessed: 2019-08-29.

[29] P. Gray, *Analysis and design of analog integrated circuits.* New York: Wiley, 2009.

[30] K. Mistry, C. Allen, C. Auth, B. Beattie, D. Bergstrom, M. Bost, M. Brazier, M. Buehler, A. Cappellani, R. Chau, C. . Choi, G. Ding, K. Fischer, T. Ghani, R. Grover, W. Han, D. Hanken, M. Hattendorf, J. He, J. Hicks, R. Huessner, D. Ingerly, P. Jain, R. James, L. Jong, S. Joshi, C. Kenyon, K. Kuhn, K. Lee, H. Liu, J. Maiz, B. McIntyre, P. Moon, J. Neirynck, S. Pae, C. Parker, D. Parsons, C. Prasad, L. Pipes, M. Prince, P. Ranade, T. Reynolds, J. Sandford, L. Shifren, J. Sebastian, J. Seiple, D. Simon, S. Sivakumar, P. Smith, C. Thomas, T. Troeger, P. Vandervoorn, S. Williams, and K. Zawadzki, "A 45 nm logic technology with high-k + metal gate transistors, strained Silicon, 9 Cu interconnect layers, 193 nm dry patterning, and 100 % Pb-free packaging," in *2007 IEEE International Electron Devices Meeting*, pp. 247–250, 2007.

[31] Robertson, J., "High dielectric constant oxides," *European Physical Journal Applied Physics*, vol. 28, no. 3, pp. 265–291, 2004.

[32] M. Jones, Y. Kwon, and D. Norton, "Dielectric constant and current transport for HfO_2 thin films on ITO," *Applied Physics A*, vol. 81, no. 2, pp. 285–288, 2005.

[33] J. Robertson and R. M. Wallace, "High-k materials and metal gates for CMOS applications," *Materials Science and Engineering: R: Reports*, vol. 88, pp. 1–41, 2015.

[34] S. Natarajan, M. Armstrong, M. Bost, R. Brain, M. Brazier, C. . Chang, V. Chikarmane, M. Childs, H. Deshpande, K. Dev, G. Ding, T. Ghani, O. Golonzka, W. Han, J. He, R. Heussner, R. James, I. Jin, C. Kenyon, S. Klopcic, S. . Lee, M. Liu, S. Lodha, B. McFadden, A. Murthy, L. Neiberg, J. Neirynck, P. Packan, S. Pae, C. Parker, C. Pelto, L. Pipes, J. Sebastian, J. Seiple, B. Sell, S. Sivakumar, B. Song, K. Tone, T. Troeger, C. Weber, M. Yang, A. Yeoh, and K. Zhang, "A 32 nm logic technology featuring 2nd-generation high-k + metal-gate transistors, enhanced channel strain and 0.171 μm^2 SRAM cell size in a 291 Mb array," in *2008 IEEE International Electron Devices Meeting*, pp. 1–3, 2008.

[35] H. Stöcker, *Taschenbuch der Physik: Formeln, Tabellen, Übersichten*. Frankfurt am Main: Verlag Harri Deutsch, 2005.

[36] "Intel microprocessor quick reference guide - year | Intel.com." `https://www.intel.com/pressroom/kits/quickrefyr.htm`. Accessed: 2019-10-23.

[37] U. Pirzada, "Exclusive: Is Intel really starting to lose its process lead? 7 nm node slated for release in 2022." `https://wccftech.com/intel-losing-process-lead-analysis-7nm-2022/`, 2016. Accessed: 2019-10-23.

[38] K. Kumawat, "7 nm vs 10 nm vs 14 nm: Fabrication technology explained - Tech Centurion." `https://www.techcenturion.com/7nm-10nm-14nm-fabrication`, 2019. Accessed: 2019-10-23.

[39] R. Sarmiento-Pérez, T. F. T. Cerqueira, S. Körbel, S. Botti, and M. A. L. Marques, "Prediction of stable nitride perovskites," *Chemistry of Materials*, vol. 27, no. 17, pp. 5957–5963, 2015.

[40] T. Zeng, R. Hoffmann, R. Nesper, N. W. Ashcroft, T. A. Strobel, and D. M. Proserpio, "Li-filled, B-substituted carbon clathrates," *Journal of the American Chemical Society*, vol. 137, no. 39, pp. 12639–12652, 2015.

[41] E. Schrödinger, "Quantisierung als Eigenwertproblem," *Annalen der Physik*, vol. 384, no. 4, pp. 361–376, 1926.

[42] W. P. Schleich, D. M. Greenberger, D. H. Kobe, and M. O. Scully, "Schrödinger equation revisited," *Proceedings of the National Academy of Sciences*, vol. 110, no. 14, pp. 5374–5379, 2013.

[43] F. Heiße, F. Köhler-Langes, S. Rau, J. Hou, S. Junck, A. Kracke, A. Mooser, W. Quint, S. Ulmer, G. Werth, K. Blaum, and S. Sturm, "High-precision measurement of the proton's atomic mass," *Physical Review Letters*, vol. 119, p. 033001, 2017.

[44] M. Born and R. Oppenheimer, "Zur Quantentheorie der Molekeln," *Annalen der Physik*, vol. 389, no. 20, pp. 457–484, 1927.

[45] H. Mustroph, "Potential-energy surfaces, the Born–Oppenheimer approximations, and the Franck–Condon principle: Back to the roots," *ChemPhysChem*, vol. 17, no. 17, pp. 2616–2629, 2016.

[46] R. van Leeuwen, "Density functional approach to the many-body problem: Key concepts and exact functionals," *Advances in Quantum Chemistry*, vol. 43, pp. 25–94, 2003.

[47] M. A. Marques, M. J. Oliveira, and T. Burnus, "Libxc: A library of exchange and correlation functionals for density functional theory," *Computer Physics Communications*, vol. 183, no. 10, pp. 2272–281, 2012.

[48] S. Lehtola, C. Steigemann, M. J. Oliveira, and M. A. Marques, "Recent developments in libxc — A comprehensive library of functionals for density functional theory," *SoftwareX*, vol. 7, pp. 1–5, 2018.

[49] J. P. Perdew, K. Burke, and M. Ernzerhof, "Generalized gradient approximation made simple," *Physical Review Letters*, vol. 77, pp. 3865–3868, 1996.

[50] J. P. Perdew, K. Burke, and M. Ernzerhof, "Generalized gradient approximation made simple [Physical Review Letters 77, 3865 (1996)]," *Physical Review Letters*, vol. 78, pp. 1396–1396, 1997.

[51] G. Kresse and J. Hafner, "Ab initio molecular dynamics for liquid metals," *Physical Review B*, vol. 47, pp. 558–561, 1993.

[52] G. Kresse and J. Hafner, "Ab initio molecular-dynamics simulation of the liquid-metal–amorphous-semiconductor transition in germanium," *Physical Review B*, vol. 49, pp. 14251–14269, 1994.

[53] G. Kresse and J. Furthmüller, "Efficiency of ab-initio total energy calculations for metals and semiconductors using a plane-wave basis set," *Computational Materials Science*, vol. 6, no. 1, pp. 15–50, 1996.

[54] G. Kresse and J. Furthmüller, "Efficient iterative schemes for ab initio total-energy calculations using a plane-wave basis set," *Physical Review B*, vol. 54, pp. 11169–11186, 1996.

[55] X. Gonze, J.-M. Beuken, R. Caracas, F. Detraux, M. Fuchs, G.-M. Rignanese, L. Sindic, M. Verstraete, G. Zerah, F. Jollet, M. Torrent, A. Roy, M. Mikami, P. Ghosez, J.-Y. Raty, and D. Allan, "First-principles computation of material properties: The ABINIT software project," *Computational Materials Science*, vol. 25, no. 3, pp. 478–492, 2002.

[56] X. Gonze, B. Amadon, P.-M. Anglade, J.-M. Beuken, F. Bottin, P. Boulanger, F. Bruneval, D. Caliste, R. Caracas, M. Côté, T. Deutsch, L. Genovese, P. Ghosez, M. Giantomassi, S. Goedecker, D. Hamann, P. Hermet, F. Jollet, G. Jomard, S. Leroux, M. Mancini, S. Mazevet, M. Oliveira, G. Onida, Y. Pouillon, T. Rangel, G.-M. Rignanese, D. Sangalli, R. Shaltaf, M. Torrent, M. Verstraete, G. Zerah, and J. Zwanziger, "ABINIT: First-principles approach to material and nanosystem properties," *Computer Physics Communications*, vol. 180, no. 12, pp. 2582–2615, 2009.

[57] X. Gonze, F. Jollet, F. A. Araujo, D. Adams, B. Amadon, T. Applencourt, C. Audouze, J.-M. Beuken, J. Bieder, A. Bokhanchuk, E. Bousquet, F. Bruneval, D. Caliste, M. Côté, F. Dahm, F. D. Pieve, M. Delaveau, M. D. Gennaro, B. Dorado, C. Espejo, G. Geneste, L. Genovese, A. Gerossier, M. Giantomassi, Y. Gillet, D. Hamann, L. He, G. Jomard, J. L. Janssen, S. L. Roux, A. Levitt, A. Lherbier, F. Liu, I. Lukačević, A. Martin, C. Martins, M. Oliveira, S. Poncé, Y. Pouillon, T. Rangel, G.-M. Rignanese, A. Romero, B. Rousseau, O. Rubel, A. Shukri, M. Stankovski, M. Torrent, M. V. Setten, B. V. Troeye, M. Verstraete, D. Waroquiers, J. Wiktor, B. Xu, A. Zhou, and J. Zwanziger, "Recent developments in the ABINIT software package," *Computer Physics Communications*, vol. 205, pp. 106–131, 2016.

[58] P. Giannozzi, S. Baroni, N. Bonini, M. Calandra, R. Car, C. Cavazzoni, D. Ceresoli, G. L. Chiarotti, M. Cococcioni, I. Dabo, A. D. Corso, S. de Gironcoli, S. Fabris, G. Fratesi, R. Gebauer, U. Gerstmann, C. Gougoussis, A. Kokalj, M. Lazzeri, L. Martin-Samos, N. Marzari, F. Mauri, R. Mazzarello, S. Paolini, A. Pasquarello, L. Paulatto, C. Sbraccia, S. Scandolo, G. Sclauzero, A. P. Seitsonen, A. Smogunov, P. Umari, and R. M. Wentzcovitch, "QUANTUM ESPRESSO: A modular and open-source software project for quantum simulations of materials," *Journal of Physics: Condensed Matter*, vol. 21, no. 39, p. 395502, 2009.

[59] P. Giannozzi, O. Andreussi, T. Brumme, O. Bunau, M. B. Nardelli, M. Calandra, R. Car, C. Cavazzoni, D. Ceresoli, M. Cococcioni, N. Colonna, I. Carnimeo, A. D. Corso, S. de Gironcoli, P. Delugas, R. A. DiStasio, A. Ferretti, A. Floris, G. Fratesi, G. Fugallo, R. Gebauer, U. Gerstmann, F. Giustino, T. Gorni, J. Jia, M. Kawamura, H.-Y. Ko, A. Kokalj, E. Küçükbenli, M. Lazzeri, M. Marsili, N. Marzari, F. Mauri, N. L. Nguyen, H.-V. Nguyen, A. O. de-la Roza, L. Paulatto, S. Poncé, D. Rocca, R. Sabatini, B. Santra, M. Schlipf, A. P. Seitsonen, A. Smogunov, I. Timrov, T. Thonhauser, P. Umari, N. Vast, X. Wu, and S. Baroni, "Advanced capabilities for materials modelling with Quantum ESPRESSO," *Journal of Physics: Condensed Matter*, vol. 29, no. 46, p. 465901, 2017.

[60] M. Elstner, D. Porezag, G. Jungnickel, J. Elsner, M. Haugk, T. Frauenheim, S. Suhai, and G. Seifert, "Self-consistent-charge density-functional tight-binding method for simulations of complex materials properties," *Physical Review B*, vol. 58, pp. 7260–7268, 1998.

[61] B. Aradi, B. Hourahine, and T. Frauenheim, "DFTB+, a sparse matrix-based implementation of the DFTB method," *The Journal of Physical Chemistry A*, vol. 111, no. 26, pp. 5678–5684, 2007.

[62] A. W. Huran, C. Steigemann, T. Frauenheim, B. Aradi, and M. A. L. Marques, "Efficient automatized density-functional tight-binding parametrizations: Application to group IV elements," *Journal of Chemical Theory and Computation*, vol. 14, no. 6, pp. 2947–2954, 2018.

[63] C.-P. Chou, Y. Nishimura, C.-C. Fan, G. Mazur, S. Irle, and H. A. Witek, "Automatized parameterization of DFTB using particle swarm optimization," *Journal of Chemical Theory and Computation*, vol. 12, no. 1, pp. 53–64, 2016.

[64] G. Zheng, S. Irle, and K. Morokuma, "Performance of the DFTB method in comparison to DFT and semiempirical methods for geometries and energies of C_{20}–C_{86} fullerene isomers," *Chemical Physics Letters*, vol. 412, no. 1, pp. 210–216, 2005.

[65] M. Elstner, "The SCC-DFTB method and its application to biological systems," *Theoretical Chemistry Accounts*, vol. 116, no. 1, pp. 316–325, 2006.

[66] M. P. Allen, *Computer simulation of liquids*. Oxford: Oxford University Press, 1997.

[67] L. Verlet, "Computer "experiments" on classical fluids. I. Thermodynamical properties of Lennard-Jones molecules," *Physical Review*, vol. 159, pp. 98–103, 1967.

[68] L. Verlet, "Computer "experiments" on classical fluids. II. Equilibrium correlation functions," *Physical Review*, vol. 165, pp. 201–214, 1968.

[69] M. P. Allen, *Computer simulation of liquids*. Oxford England New York: Clarendon Press Oxford University Press, 1987.

[70] W. Heitler and F. London, "Wechselwirkung neutraler Atome und homöopolare Bindung nach der Quantenmechanik," *Zeitschrift für Physik*, vol. 44, no. 6, pp. 455–472, 1927.

[71] M. Amsler and S. Goedecker, "Crystal structure prediction using the minima hopping method," *The Journal of Chemical Physics*, vol. 133, no. 22, p. 224104, 2010.

[72] S. Goedecker, "Minima hopping: An efficient search method for the global minimum of the potential energy surface of complex molecular systems," *The Journal of Chemical Physics*, vol. 120, no. 21, pp. 9911–9917, 2004.

[73] R. P. Bell, "The theory of reactions involving proton transfers," *Proceedings of the Royal Society of London A: Mathematical, Physical and Engineering Sciences*, vol. 154, no. 882, pp. 414–429, 1936.

[74] M. G. Evans and M. Polanyi, "Inertia and driving force of chemical reactions," *Transactions of the Faraday Society*, vol. 34, pp. 11–24, 1938.

[75] A. Jain, S. P. Ong, G. Hautier, W. Chen, W. D. Richards, S. Dacek, S. Cholia, D. Gunter, D. Skinner, G. Ceder, and K. a. Persson, "The Materials Project: A materials genome approach to accelerating materials innovation," *APL Materials*, vol. 1, no. 1, p. 011002, 2013.

[76] F. Bundy, W. Bassett, M. Weathers, R. Hemley, H. Mao, and A. Goncharov, "The pressure-temperature phase and transformation diagram for carbon; updated through 1994," *Carbon*, vol. 34, no. 2, pp. 141–153, 1996.

[77] L. M. Ghiringhelli and E. J. Meijer, "Liquid carbon: Freezing line and structure near freezing," in *Computer-based modeling of novel carbon systems and their properties: Beyond nanotubes* (L. Colombo and A. Fasolino, eds.), pp. 1–36, Dordrecht: Springer, 2010.

[78] E. W. Weisstein, "Method of steepest descent," *From MathWorld - A Wolfram Web Resource.* https://mathworld.wolfram.com/MethodofSteepestDescent.html, Accessed: 2018-07-01.

[79] O. Forster, *Analysis 2 : Differentialrechnung im $\mathbb{R}^n$, gewöhnliche Differentialgleichungen*. Wiesbaden: Vieweg+Teubner Verlag / GWV Fachverlage, 2008.

[80] M. R. Hestenes and E. Stiefel, "Methods of conjugate gradients for solving linear systems," *Journal of Research of the National Bureau of Standards*, vol. 49, no. 6, pp. 409–436, 1952.

[81] R. Heggelien Refsnæs, "A brief introduction to the conjugated gradient method." `https://www.idi.ntnu.no/~elster/tdt24/tdt24-f09/cg.pdf`, 2009. Accessed: 2019-01-15.

[82] A. Törn, *Global optimization*. Berlin New York: Springer, 1989.

[83] M. Schumer and K. Steiglitz, "Adaptive step size random search," *IEEE Transactions on Automatic Control*, vol. 13, no. 3, pp. 270–276, 1968.

[84] R. Eberhart and J. Kennedy, "A new optimizer using particle swarm theory," in *MHS'95. Proceedings of the sixth International Symposium on micro machine and human science*, pp. 39–43, 1995.

[85] Y. Wang, J. Lv, L. Zhu, and Y. Ma, "Crystal structure prediction via particle-swarm optimization," *Physical Review B*, vol. 82, p. 094116, 2010.

[86] T. F. Cerqueira, *Structural prediction and materials design: From high throughput to global minima optimization methods*. PhD thesis, Friedrich-Schiller-Universität Jena, Jena, 2017.

[87] H. M. Powell, "15. The structure of molecular compounds. Part IV. Clathrate compounds," *Journal of the Chemical Society*, pp. 61–73, 1948.

[88] "Latin definitions for: clatratus (Latin Search) - Latin Dictionary and Grammar Resources - Latdict," `https://latin-dictionary.net/search/latin/clatratus`, Accessed: 2019-01-22.

[89] G. A. Jeffrey, "Hydrate inclusion compounds," *Journal of inclusion phenomena*, vol. 1, no. 3, pp. 211–222, 1984.

[90] J.-A. Dolyniuk, B. Owens-Baird, J. Wang, J. V. Zaikina, and K. Kovnir, "Clathrate thermoelectrics," *Materials Science and Engineering: R: Reports*, vol. 108, pp. 1–46, 2016.

[91] M. Beekman and G. S. Nolas, "Inorganic clathrate-II materials of group 14: Synthetic routes and physical properties," *Journal of Materials Chemistry*, vol. 18, pp. 842–851, 2008.

[92] M. Amsler, S. Botti, M. A. L. Marques, T. J. Lenosky, and S. Goedecker, "Low-density silicon allotropes for photovoltaic applications," *Physical Review B*, vol. 92, p. 014101, 2015.

[93] C. Gatti, L. Bertini, N. P. Blake, and B. B. Iversen, "Guest–framework interaction in type I inorganic clathrates with promising thermoelectric properties: On the ionic versus neutral nature of the alkaline-earth metal guest A in $A_8Ga_{16}Ge_{30}$ (A=Sr, Ba)," *Chemistry – A European Journal*, vol. 9, no. 18, pp. 4556–4568, 2003.

[94] M. Christensen, S. Johnsen, and B. B. Iversen, "Thermoelectric clathrates of type I," *Dalton Transactions*, vol. 39, pp. 978–992, 2010.

[95] S. Bobev and S. C. Sevov, "Clathrates of group 14 with alkali metals: An exploration," *Journal of Solid State Chemistry*, vol. 153, no. 1, pp. 92–105, 2000.

[96] K. A. Kovnir and A. V. Shevelkov, "Semiconducting clathrates: Synthesis, structure and properties," *Russian Chemical Reviews*, vol. 73, no. 9, p. 923, 2004.

[97] A. V. Shevelkov and K. Kovnir, "Zintl clathrates," in *Zintl phases: Principles and recent developments* (T. F. Fässler, ed.), pp. 97–142, Berlin Heidelberg: Springer, 2011.

[98] G. S. Nolas, *The physics and chemistry of inorganic clathrates.* Dordrecht: Springer, 2014.

[99] X. Blase, G. Benedek, and M. Bernasconi, "Structural, mechanical, and superconducting properties of clathrates," in *Computer-based modeling of novel carbon systems and their properties: Beyond nanotubes* (L. Colombo and A. Fasolino, eds.), pp. 171–206, Dordrecht: Springer, 2010.

[100] E. A. Ekimov, V. A. Sidorov, E. D. Bauer, N. N. Mel'nik, N. J. Curro, J. D. Thompson, and S. M. Stishov, "Superconductivity in diamond," *Nature*, vol. 428, no. 6982, pp. 542–545, 2004.

[101] O. Gunnarsson, "Superconductivity in fullerides," *Reviews of Modern Physics*, vol. 69, pp. 575–606, 1997.

[102] A. F. Hebard, M. J. Rosseinsky, R. C. Haddon, D. W. Murphy, S. H. Glarum, T. T. M. Palstra, A. P. Ramirez, and A. R. Kortan, "Superconductivity at 18 K in potassium-doped C_{60}," *Nature*, vol. 350, no. 6319, pp. 600–601, 1991.

[103] K. S. Chan, M. A. Miller, W. Liang, and C. Ellis-Terrell, "Computational design and synthesis of nitrogen-substituted carbon and silicon clathrates," *Materials Research Letters*, vol. 2, no. 2, pp. 70–75, 2014.

[104] C. Perottoni and J. Da Jornada, "The carbon analogues of type-I silicon clathrates," *Journal of Physics: Condensed Matter*, vol. 13, no. 26, p. 5981, 2001.

[105] A. San-Miguel, P. Mélinon, D. Connétable, X. Blase, F. Tournus, E. Reny, S. Yamanaka, and J. P. Itié, "Pressure stability and low compressibility of intercalated cagelike materials: The case of silicon clathrates," *Physical Review B*, vol. 65, p. 054109, 2002.

[106] K. S. Chan, "Hybrid carbon-based clathrates for energy storage," *C*, vol. 4, no. 1, 2018.

[107] G. Benedek, E. Galvani, S. Sanguinetti, and S. Serra, "Hollow diamonds: stability and elastic properties," *Chemical Physics Letters*, vol. 244, no. 5, pp. 339–344, 1995.

[108] "Covalent radius for all the elements in the periodic table | Periodictable.com."
      `https://periodictable.com/Properties/A/CovalentRadius.v.log.html`.
      Accessed: 2019-11-06.

[109] S. Ruben, *Handbook of the elements*. La Salle, Ill: Open Court Pub. Co, 1985.

[110] A. K. Rappe, C. J. Casewit, K. S. Colwell, W. A. G. III, and W. M. Skiff, "UFF, a full
      periodic table force field for molecular mechanics and molecular dynamics simulations,"
      Journal of the American Chemical Society, vol. 114, no. 25, pp. 10024–10035, 1992.

[111] J. Frenzel, A. Oliveira, N. Jardillier, T. Heine, and G. Seifert, "Semi-relativistic, self-
      consistent charge Slater-Koster tables for density-functional based tight-binding (DFTB)
      for materials science simulations," *TU-Dresden*, 2004–2009.

[112] R. Nunez-Gonzalez, A. Posada-Amarillas, D. Galvan, and A. Reyes-Serrato,
      "Concentration-dependent study of electronic and optical properties of c-Si and c-Si:H,"
      Physica Status Solidi B - Basic Solid State Physics, vol. 248, no. 7, pp. 1712–1717, 2011.

[113] D. Batchelder and R. Simmons, "Lattice constants and thermal expansivities of silicon
      and of calcium fluoride between 6 and 322 K," *Journal of Chemical Physics*, vol. 41,
      pp. 2324–2329, 1964.

[114] W. Parrish, "Results of the IUCr precision lattice-parameter project," *Acta Crystallo-
      graphica*, vol. 13, no. 10, pp. 838–850, 1960.

[115] P. Debye and P. Scherrer, "Interferenzen an regellos orientierten Teilchen im Röntgen-
      licht," *Physikalische Zeitschrift*, vol. 17, pp. 277–283, 1916.

[116] K. Lejaeghere, V. V. Speybroeck, G. V. Oost, and S. Cottenier, "Error estimates for
      solid-state density-functional theory predictions: An overview by means of the ground-
      state elemental crystals," *Critical Reviews in Solid State and Materials Sciences*, vol. 39,
      pp. 1–24, 2014.

[117] H. Küstner and H. Remy, "Struktur des Siliziums," *Physikalische Zeitschrift*, vol. 24,
      pp. 25–29, 1923.

[118] W. Bond and W. Kaiser, "Interstitial versus substitutional oxygen in silicon," *Journal of
      Physics and Chemistry of Solids*, vol. 16, pp. 44–45, 1960.

[119] D. Többens, N. Stüßer, K. Knorr, H. Mayer, and G. Lampert, "E9: The new high-
      resolution neutron powder diffractometer at the Berlin neutron scattering center,"
      Materials Science Forum, vol. 378, pp. 288–293, 2001.

[120] M. Straumanis and E. Aka, "Lattice parameters, coefficients of thermal expansion and
      atomic weights of purest silicon and germanium," *Journal of Applied Physics*, vol. 23,
      pp. 330–334, 1952.

[121] M. Straumanis, P. Borgeaud, and W. James, "Perfection of the lattice of dislocation-free
      silicon, studies by the lattice-constant and density method," *Journal of Applied Physics*,
      vol. 32, pp. 1382–1384, 1961.

[122] S.-L. Qiu and P. Marcus, "Structure and stability under pressure of cubic and hexagonal diamond crystals of C, BN and Si from first principles," *Journal of Physics: Condensed Matter*, vol. 23, no. 21, p. 215501, 2011.

[123] W. Yim and R. Paff, "The thermal expansion of of AlN, sapphire, and silicon," *Journal of Applied Physics*, vol. 45, pp. 1456–1457, 1974.

[124] S. Nan and L. Yi-huan, "X-ray measurement of the thermal expansion of germanium, silicon, indium antimonide and gallium arsenenide," *Acta Physica Sinica*, vol. 112, no. 8, pp. 699–704, 1964.

[125] A. Kohno, N. Aomine, Y. Soejima, and A. Okazaki, "Anomalous behaviour of silicon single-crystals observed by X-ray diffraction," *Japanese Journal of Applied Physics, Part 1*, vol. 33, pp. 5073–5077, 1994.

[126] C.-Y. Yeh, Z. W. Lu, S. Froyen, and A. Zunger, "Zinc-blende–wurtzite polytypism in semiconductors," *Physical Review B*, vol. 46, pp. 10086–10097, 1992.

[127] Y. Okada and Y. Tokumaru, "Precise determination of lattice parameter and thermal expansion coefficient of silicon between 300 and 1500 K," *Journal of Applied Physics*, vol. 56, pp. 314–320, 1984.

[128] B. N. Dutta, "Lattice constants and thermal expansion of silicon up to 900 °C by X-ray method," *Physica Status Solidi (b)*, vol. 2, no. 8, pp. 984–987, 1962.

[129] A. Kitano, K. Moriguchi, M. Yonemura, S. Munetoh, A. Shintani, H. Fukuoka, S. Yamanaka, E. Nishibori, M. Takata, and M. Sakata, "Structural properties and thermodynamic stability of Ba-doped silicon type-I clathrates synthesized under high pressure," *Physical Review B*, vol. 64, p. 045206, 2001.

[130] C. Hubbard, H. Swanson, and F. Mauer, "A silicon powder diffraction standard reference material," *Journal of Applied Crystallography*, vol. 8, pp. 45–48, 1975.

[131] E. Jette and F. Foote, "Precision determination of lattice constants," *Journal of Chemical Physics*, vol. 3, pp. 605–616, 1935.

[132] C. Filippi, D. J. Singh, and C. J. Umrigar, "All-electron local-density and generalized-gradient calculations of the structural properties of semiconductors," *Physical Review B*, vol. 50, pp. 14947–14951, 1994.

[133] F. Wu, D. Jun, E. J. Kan, and Z. Y. Li, "Density functional predictions of new silicon allotropes: Electronic properties and potential applications to Li-battery anode materials," *Solid State Communications*, vol. 151, pp. 1228–1230, 2011.

[134] Wolfram Research, Inc., "Mathematica, Version 10.0," Champaign, IL, 2014.

[135] R. Nesper, K. Vogel, and P. E. Blöchl, "Hypothetical carbon modifications derived from zeolite frameworks," *Angewandte Chemie International Edition in English*, vol. 32, no. 5, pp. 701–703, 1993.

[136] J. F. Liebman and A. Greenberg, "A survey of strained organic molecules," *Chemical Reviews*, vol. 76, no. 3, pp. 311–365, 1976.

[137] R. Gillespie, "The valence-shell electron-pair repulsion (VSEPR) theory of directed valency," *Journal of Chemical Education*, vol. 40, no. 6, p. 295, 1963.

[138] L. Bartell, "Molecular geometry: Bonded versus nonbonded interactions," *Journal of Chemical Education*, vol. 45, no. 12, p. 754, 1968.

[139] "The periodic table of the elements by WebElements." `https://www.webelements.com`. Accessed: 2018-11-15.

[140] R. J. Ternansky, D. W. Balogh, and L. A. Paquette, "Dodecahedrane," *Journal of the American Chemical Society*, vol. 104, no. 16, pp. 4503–4504, 1982.

[141] L. A. Paquette, R. J. Ternansky, D. W. Balogh, and G. Kentgen, "Total synthesis of dodecahedrane," *Journal of the American Chemical Society*, vol. 105, no. 16, pp. 5446–5450, 1983.

[142] P. E. Eaton and T. W. Cole, "Cubane," *Journal of the American Chemical Society*, vol. 86, no. 15, pp. 3157–3158, 1964.

[143] P. E. Eaton and T. W. Cole, "The cubane system," *Journal of the American Chemical Society*, vol. 86, no. 5, pp. 962–964, 1964.

[144] R. L. Johnston and R. Hoffmann, "Superdense carbon, C_8: Supercubane or analog of γ-Si?," *Journal of the American Chemical Society*, vol. 111, no. 3, pp. 810–819, 1989.

[145] G. Maier, S. Pfriem, U. Schäfer, and R. Matusch, "Tetra-tert-butyltetrahedrane," *Angewandte Chemie International Edition in English*, vol. 17, no. 7, pp. 520–521, 1978.

[146] M. T. Yin and M. L. Cohen, "Structural theory of graphite and graphitic silicon," *Physical Review B*, vol. 29, pp. 6996–6998, 1984.

[147] A. Acun, L. Zhang, P. Bampoulis, M. Farmanbar, A. van Houselt, A. N. Rudenko, M. Lingenfelder, G. Brocks, B. Poelsema, M. I. Katsnelson, and H. J. W. Zandvliet, "Germanene: The germanium analogue of graphene," *Journal of Physics: Condensed Matter*, vol. 27, no. 44, p. 443002, 2015.

[148] T. L. Cottrell, *The strengths of chemical bonds*. London: Butterworths Scientific Publications, 1958.

[149] B. T. Connell, "Selected bond energies and bond lengths." `https://www.chem.tamu.edu/rgroup/connell/linkfiles/bonds.pdf`, 2003. Accessed: 2019-11-07.

[150] J. P. Perdew and Y. Wang, "Accurate and simple analytic representation of the electron-gas correlation energy," *Physical Review B*, vol. 45, pp. 13244–13249, 1992.

[151] K. Burke, J. P. Perdew, and Y. Wang, "Derivation of a generalized gradient approximation: The PW91 density functional," in *Electronic density functional theory: Recent progress and new directions* (J. F. Dobson, G. Vignale, and M. P. Das, eds.), pp. 81–111, Boston, MA: Springer, 1998.

[152] A. Jain, S. P. Ong, G. Hautier, W. Chen, W. D. Richards, S. Dacek, S. Cholia, D. Gunter, D. Skinner, G. Ceder, and K. a. Persson, "Commentary: The Materials Project: A materials genome approach to accelerating materials innovation," *APL Materials*, vol. 1, no. 1, p. 011002, 2013.

[153] M. Wörle, R. Nesper, G. Mair, M. Schwarz, and H. von Schnering, "LiBC - ein vollständig interkalierter Heterographit," *Zeitschrift für Anorganische und Allgemeine Chemie*, vol. 621, pp. 1153–1159, 1995.

[154] T. Langer, S. Dupke, C. Dippel, M. Winter, H. Eckert, and R. Pöttgen, "LiBC - Synthesis, electrochemical and solid-state NMR investigations," *Zeitschrift für Naturforschung B*, vol. 67, no. 11, pp. 1212–1220, 2012.

[155] A. Fogg, J. Meldrum, G. Darling, J. Claridge, and M. Rosseinsky, "Chemical control of electronic structure and superconductivity in layered borides and borocarbides: Understanding the absence of superconductivity in $Li_x BC$," *Journal of the American Chemical Society*, vol. 128, pp. 10043–10053, 2006.

[156] N. Vojteer and H. Hillebrecht, "$Li_2B_{12}C_2$ and $LiB_{13}C_2$: Colorless boron-rich boride carbides of lithium," *Angewandte Chemie International Edition*, vol. 45, no. 1, pp. 165–168, 2006.

[157] S. Förster, K. Meinel, R. Hammer, M. Trautmann, and W. Widdra, "Quasicrystalline structure formation in a classical crystalline thin-film system," *Nature*, vol. 502, pp. 215–218, 2013.

[158] M. R. G. Marques, J. Wolff, C. Steigemann, and M. A. L. Marques, "Neural network force fields for simple metals and semiconductors: Construction and application to the calculation of phonons and melting temperatures," *Physical Chemistry Chemical Physics*, vol. 21, no. 12, pp. 6506–6516, 2019.

[159] C. Rice and W. Robinson, "Structural changes in the solid solution $(Ti_{1-x} V_x)_2 O_3$ as x varies from zero to one," *Journal of Solid State Chemistry*, vol. 21, pp. 145–154, 1977.

[160] E. Newnham and Y. de Haan, "Refinement of the α Al_2O_3, Ti_2O_3, V_2O_3 and Cr_2O_3 structures," *Zeitschrift für Kristallographie*, vol. 117, pp. 235–237, 1962.

[161] S. Abrahams, "Magnetic and crystal structure of titanium sesquioxide," *Physical Review*, vol. 130, pp. 2230–2237, 1963.

[162] C. Rice and W. Robinson, "Structural changes associated with the semiconductor-to-metal transition in Ti_2O_3," *Materials Research Bulletin*, vol. 11, pp. 1355–1360, 1976.

[163] V. Goldschmidt, T. Barth, and G. Lunde, "Untersuchungen über die Kristallstruktur von Sesquioxyden und Verbindungen ABO_3," *Skrifter utgitt av det Norske Videnskaps-Akademi i Oslo 1: Matematisk-Naturvidenskapelig Klasse*, vol. 1928, pp. 1–165, 1928.

[164] L. Eckert and R. Bradt, "Thermal expansion of corundum structure Ti_2O_3 and V_2O_3," *Journal of Applied Physics*, vol. 44, pp. 3470–3472, 1973.

[165] G. Shirane, S. Pickart, and R. Newnham, "Neutron-diffraction study of Ti_2O_3," *Journal of Physics and Chemistry of Solids*, vol. 13, pp. 166–167, 1960.

[166] W. Robinson, "The crystal structure of Ti_2O_3, a semiconductor, and $(Ti_{0.900} V_{0.100})_2O_3$, a semimetal," *Journal of Solid State Chemistry*, vol. 9, pp. 255–260, 1974.

[167] M. G. Vincent, K. Yvon, A. Grüttner, and J. Ashkenazi, "Electron-density studies of metal–metal bonds. I. The deformation density of Ti_2O_3 at 295 K," *Acta Crystallographica Section A*, vol. 36, no. 5, pp. 803–808, 1980.

[168] D. Taylor, "Thermal expansion data: III Sesquioxides, M_2O_3, with the corundum and the A-, B- and C-M_2O_3 structures," *Transactions and Journal of the British Ceramic Society*, vol. 83, pp. 92–98, 1984.

[169] B. Holmberg, "Disorder and order in solid solutions of oxygen in α-titanium," *Acta Chemica Scandinavica*, vol. 16, pp. 1245–1250, 1962.

[170] A. Jostsons and A. S. Malin, "The ordered structure of Ti_3O," *Acta Crystallographica Section B*, vol. 24, no. 2, pp. 211–213, 1968.

[171] I. Kornilov, V. Vavilova, L. Fykin, R. Ozerov, S. Solov'ev, and V. Smirnov, "Neutron diffraction investigation of ordered structures in the titanium-oxygen system," *Metallurgical Transactions*, vol. 1, pp. 2569–2571, 1970.

[172] J. Bernal, E. Djatlowa, I. Kasarnowsky, S. Reichstein, and A. Ward, "The structure of strontium and barium peroxides SrO_2 and BaO_2," *Zeitschrift für Kristallographie - Crystalline Materials*, vol. 92, pp. 344–354, 1935.

[173] H. Bärnighausen, H. Beck, H. Grüninger, E. Rietschel, and N. Schultz, "Neue AB_2-Strukturtypen mit siebenfach koordiniertem Kation.," *Zeitschrift für Kristallographie - Crystalline Materials*, vol. 128, p. 430, 1969.

[174] P. Borlido, C. Rödl, M. A. L. Marques, and S. Botti, "The ground state of two-dimensional silicon," *2D Materials*, vol. 5, no. 3, p. 035010, 2018.

[175] N. Dubrovinskaia, L. Dubrovinsky, N. A. Solopova, A. Abakumov, S. Turner, M. Hanfland, E. Bykova, M. Bykov, C. Prescher, V. B. Prakapenka, S. Petitgirard, I. Chuvashova, B. Gasharova, Y.-L. Mathis, P. Ershov, I. Snigireva, and A. Snigirev, "Terapascal static pressure generation with ultrahigh yield strength nanodiamond," *Science advances*, vol. 2, no. 7, pp. e1600341–e1600341, 2016.

[176] W. W. Tipton and R. G. Hennig, "A grand canonical genetic algorithm for the prediction of multi-component phase diagrams and testing of empirical potentials," *Journal of Physics: Condensed Matter*, vol. 25, no. 49, p. 495401, 2013.

[177] F. Calvo, D. Schebarchov, and D. J. Wales, "Grand and semigrand canonical basin-hopping," *Journal of Chemical Theory and Computation*, vol. 12, no. 2, pp. 902–909, 2016.

[178] Q. Zhu, A. Samanta, B. Li, R. E. Rudd, and T. Frolov, "Predicting phase behavior of grain boundaries with evolutionary search and machine learning," *Nature Communications*, vol. 9, no. 1, p. 467, 2018.

[179] I. Bronstein, K. Semendjajew, G. Musiol, and H. Mühlig, *Taschenbuch der Mathematik*. Frankfurt am Main: Verlag Harri Deutsch, 2005.

[180] E. W. Weisstein, "Platonic solid.," *From MathWorld - A Wolfram Web Resource.* `https://mathworld.wolfram.com/PlatonicSolid.html`, Accessed: 2018-11-12.

[181] E. W. Weisstein, "Archimedean solid.," *From MathWorld - A Wolfram Web Resource.* `https://mathworld.wolfram.com/ArchimedeanSolid.html`, Accessed: 2018-11-12.

[182] E. W. Weisstein, "Johnson solid.," *From MathWorld - A Wolfram Web Resource.* `https://mathworld.wolfram.com/JohnsonSolid.html`, Accessed: 2018-11-12.

[183] E. W. Weisstein, "Prism.," *From MathWorld - A Wolfram Web Resource.* `https://mathworld.wolfram.com/Prism.html`, Accessed: 2018-11-12.

[184] E. W. Weisstein, "Antiprism.," *From MathWorld - A Wolfram Web Resource.* `https://mathworld.wolfram.com/Antiprism.html`, Accessed: 2018-11-12.

[185] E. W. Weisstein, "Euler characteristic.," *From MathWorld - A Wolfram Web Resource.* `https://mathworld.wolfram.com/EulerCharacteristic.html`, Accessed: 2018-11-27.

[186] D. Richeson, *Euler's gem: The polyhedron formula and the birth of topology*. Princeton, N.J: Princeton University Press, 2008.

[187] E. W. Weisstein, "Angle.," *From MathWorld - A Wolfram Web Resource.* `https://mathworld.wolfram.com/Angle.html`, Accessed: 2018-07-01.

[188] E. W. Weisstein, "Solid angle.," *From MathWorld - A Wolfram Web Resource.* `https://mathworld.wolfram.com/SolidAngle.html`, Accessed: 2018-07-01.

[189] F. Eriksson, "On the measure of solid angles," *Mathematics Magazine*, vol. 63, no. 3, pp. 184–187, 1990.

[190] E. W. Weisstein, "Dihedral angle.," *From MathWorld - A Wolfram Web Resource.* `https://mathworld.wolfram.com/DihedralAngle.html`, Accessed: 2018-07-01.

[191] Wolfram Research, Inc., "Mathematica, Version 11.2," Champaign, IL, 2017.

XVI

List of publications

1. P. Borlido, C. Steigemann, N. N. Lathiotakis, M. A. L. Marques, and S. Botti, "Structural prediction of two-dimensional materials under strain," *2D Materials*, vol. 4, no. 4, p. 045009, 2017.

2. S. Lehtola, C. Steigemann, M. J. Oliveira, and M. A. Marques, "Recent developments in libxc — a comprehensive library of functionals for density functional theory," *SoftwareX*, vol. 7, pp. 1 – 5, 2018.

3. A. W. Huran, C. Steigemann, T. Frauenheim, B. Aradi, and M. A. L. Marques, "Efficient automatized density-functional tight-binding parametrizations: Application to group IV elements," *Journal of Chemical Theory and Computation*, vol. 14, no. 6, pp. 2947–2954, 2018.

4. M. R. G. Marques, J. Wolff, C. Steigemann, and M. A. L. Marques, "Neural network force fields for simple metals and semiconductors: Construction and application to the calculation of phonons and melting temperatures," *Physical Chemistry Chemical Physics*, vol. 21, no. 12, pp. 6506–6516, 2019.

Acknowledgements / Danksagung

xx

Curriculum vitae / Lebenslauf

Personal data / Persönliche Informationen

Name:	Conrad Steigemann, born Schuster
Date of birth:	15 February 1986
Place of birth:	Schwedt / Oder

Education / Bildung

2015 - 2019	PhD student at the Martin-Luther-University Halle-Wittenberg Institute for Physics, 06120 Halle (Saale), Germany
2011 - 2014	Scientific staff at the University Rostock Institute for Physics, 18055 Rostock, Germany
2005 - 2011	Study of Physics at the University Rostock Institute for Physics, 18055 Rostock, Germany diploma thesis: „Modulation of ultra-short laser pulses in phase and amplitude"
2005	Abitur / High School Certificate A.-v.-Humboldt-Gymnasium Greifswald, Germany

Halle (Saale),

Conrad Steigemann

Eidesstattliche Erklärung

Hiermit erkläre ich, gemäß §5 der Promotionsordnung vom 13.07.2016 der Naturwissenschaftlichen Fakultät II - Chemie, Physik und Mathematik der Martin-Luther-Universität Halle-Wittenberg, dass die vorliegende Arbeit

„Global structure prediction of phase diagrams"

selbständig und ohne fremde Hilfe verfasst wurde. Andere als die von mir angegebenen Quellen und Hilfsmittel wurden nicht genutzt. Darüber hinaus sind wörtlich oder inhaltlich entnommenen Stellen aus den genutzten Werken als solche gekennzeichnet. Ich erkläre, dass die Angaben wahrheitsgemäß gemacht und keine Dissertation an einer anderen wissenschaftlichen Einrichtung zur Erlangung eines akademischen Grades eingereicht wurde.

Halle (Saale), 19.12.2019

Conrad Steigemann